# Molecular Composition, Volatility, and Formation Mechanisms of Biogenic Secondary Organic Aerosol

Emma Louise D'Ambro

A dissertation

submitted in partial fulfillment of the

requirements for the degree of

Doctor of Philosophy

University of Washington

2018

Reading Committee:

Joel A. Thornton, Chair

Robert E. Synovec

Matthew F. Bush

Program Authorized to Offer Degree:

Chemistry

University of Washington

Abstract

# Molecular Composition, Volatility, and Formation Mechanisms of Biogenic Secondary Organic Aerosol

Emma Louise D'Ambro

Chair of the Supervisory Committee:
Prof. Joel A. Thornton
Atmospheric Sciences

The research herein seeks to answer the following question: what are the main processes governing the formation and properties of secondary organic aerosol (SOA) from oxidation of biogenic volatile organic compounds (BVOC) in both remote and anthropogenically influenced regions? To study this gas-to-particle conversion, a Time-of-Flight Iodide-adduct chemical ionization mass spectrometer has been coupled to a newly developed inlet manifold, the Filter Inlet for Gases and AEROsols (FIGAERO), which provides alternating, online, chemically speciated measurements of both the gas- and particle-phases. The FIGAERO also provides information on effective vapor pressures of each detected composition which can be used to test gas-particle partitioning theories or group contribution methods and thus gain insights into the chemical and physical states of the aerosol. This allows the chemical composition and volatility of bulk aerosol and individual compounds to be examined. By applying this field-deployable

instrumentation to a variety of environments, in particular atmospheric simulation chamber experiments, where individual reactant and oxidant pairings can be targeted and examined, as well as the ambient atmosphere, a piece-by-piece molecular understanding of SOA formation from BVOC can be generated. This work is explicitly focused on the oxidation of isoprene and α-pinene, the two most abundantly emitted BVOC globally which have been shown to form SOA via distinctly different mechanisms, in atmospheric simulation chambers. In chapter 2, I present measurements of a low volatility compound, $C_5H_{12}O_6$, that plays a significant role in SOA formation via gas-particle partitioning and that the presence of $NO_x$, a common anthropogenic pollutant, will decrease the amount of SOA formed by this mechanism. In chapter 3, I apply a detailed mechanistic model to these measurements and find that the pathway to very low volatility material is minor under typical atmospheric conditions. Instead, autoxidation is a more significant pathway in the atmosphere, resulting in higher volatility material than bimolecular reactions. Chapter 4 focuses on the volatility and phase state of SOA from α-pinene ozonolysis. I found that the physical age of the aerosol, as opposed to the oxidative age, determines the volatility of the aerosol and that reversible oligomerization must be invoked to model our observations.

## TABLE OF CONTENTS

## LIST OF FIGURES

## LIST OF TABLES

## ACKNOWLEDGEMENTS

First and foremost, thank you to my advisor, Joel Thornton. I feel incredibly fortunate to have had an advisor who invests so much in their students. From painstakingly editing my manuscripts, helping me find swage in the lab, and teaching me the importance of giving a good talk, he has been the most supportive, kind, and hardworking role model throughout my graduate school experience.

I am also grateful to the other members of the Thornton lab who I have had the privilege to work with over the last several years: Beth Friedman, Claudia Mohr, Cassandra Gaston, Ben Lee, Felipe Lopez-Hilfiker, Lauren Whybrew, Lexie Goldberger, Jessica Haskins, Siegfried Schobesberger, Matson Pothier, Yue Zhao, Jeremy Chan, Qiaoyun Peng, Megan McKeown, Julia Greenwald, Kira Melander, and Brett Palm. I have enjoyed spending time with everyone, whether it has been on field outings, working in the lab, science talks in the office, or eating lunch together outside. I owe particular gratitude to Felipe, without whom I am certain I would not have made it to this point. His patience in teaching me atmospheric measurements from scratch and willingness to drop everything to help when I needed it is eternally appreciated. Thank you to the undergraduates I have had the pleasure to work with. Their zest for life and learning has continually reminded me that science is interesting and fun, even when working on the mundane.

Finally, thank you to my family. My parents have always supported and pushed me to be better, and without them I would not be here. Caroline has shared part of this fantastic Seattle journey

with me and helped keep things in perspective along the way, while also preventing me from starving. Lastly, thank you to Vincent, who has supported, encouraged, listened to me cry, and cheered the loudest for all my successes.

# Chapter 1. INTRODUCTION

Atmospheric aerosol particles, defined as solid and/or liquid particles suspended in the air, can reduce visibility, adversely affect health, and have uncertain overall effects on global climate change [*Hallquist et al.*, 2009], with particles smaller than 1 μm in diameter playing particularly important roles [*Boucher*, 2013]. These submicron particles typically contain a significant fraction of organic material, on the order of 20-90% [*Jimenez et al.*, 2009; *Zhang et al.*, 2007]. Organic material can be emitted directly to the atmosphere as particles, or in the gas phase as volatile organic compounds (VOC). The atmospheric reactions of VOC with common atmospheric oxidants (e.g., $NO_3$, OH, or $O_3$) leads to net oxidation of the carbon, with a fraction of the carbon being in the form of more functionalized lower volatility products that condense onto [*Riipinen et al.*, 2011] or react heterogeneously [*Surratt et al.*, 2010] on existing particles, or participate in homogeneous heteromolecular nucleation to form new particles [*Brock et al.*, 1995]. This condensed phase organic material formed from gas to particle conversion is known as secondary organic aerosol (SOA).

A major source of SOA globally is thought to originate from VOC emitted by terrestrial vegetation [*Hallquist et al.*, 2009; *Spracklen et al.*, 2011]. The global emission rate of these biogenic VOC (BVOC) is estimated to be 1150 TgC/yr [*Guenther et al.*, 1995], higher than the sum total VOC emitted by anthropogenic activities associated with fossil fuel extraction and use. The largest classes of BVOCs include isoprene ($C_5H_8$), monoterpenes ($C_{10}H_{16}$), and sesquiterpenes ($C_{15}H_{24}$). At ~500 TgC/yr, isoprene is the most predominantly emitted BVOC class annually, followed by monoterpenes at ~130 TgC/yr [*Guenther et al.*, 1995]. Isoprene is

primarily emitted from broad-leaf deciduous trees, which are most prevalent at the mid-latitudes, while monoterpenes are primarily emitted from coniferous trees, which are most prevalent at higher latitudes, though significant emissions of both occur in essentially all terrestrial ecosystems. BVOC are highly reactive with respect to atmospheric oxidants, resulting in lifetimes that range from tens of minutes to a few hours (~0.5-3 hours). The oxidative degradation of BVOC is complex, with a single BVOC precursor likely producing 100s of different products stable on timescales of hours to weeks. Estimates of the global source of SOA from BVOC oxidation range from 50 to 380 Tg $yr^{-1}$, with a best estimate of 140 Tg $yr^{-1}$ [*Spracklen et al.*, 2011].

The oxidative degradation of BVOCs proceeds via one of two pathways: functionalization or fragmentation. Functionalization adds functional groups to the parent VOC, resulting in a lower volatility product. Fragmentation occurs when carbon-carbon bonds are broken, resulting in smaller molecules with higher volatility relative to functionalization.

The partitioning of any organic vapor into this condensed organic phase can be described by Raoult's Law, known in the field of atmospheric chemistry as equilibrium absorptive partitioning theory [*Pankow*, 1994], assuming condensed-phase (i.e. particulate) organic matter is a mixture of many individual components acting as nearly ideal solutes. Raoult's Law states that over an ideal liquid mixture, the partial pressure of each component in the mixture is equivalent to its mole fraction in the mixture multiplied by its vapor pressure over pure solution. This can be described by the saturation vapor concentration (c*). The c* of a given compound relates the

mass concentration of organic aerosol ($C_{OA}$, μg $m^{-3}$) to the mole fraction of a compound *i* in the gas ($\square_i^g$) relative to particle ($\square_i^p$) phase as shown in Eq. 1.1.

$$\square_i^g = \square_i^p \, c^* \qquad \text{(Eq. 1.1)}$$

Assuming partitioning is reversible, the c* of components determines the extent to which it partitions. The lower the c*, the lower the volatility or vapor pressure, the more the component will partition to the particle phase.

For compounds with the same carbon number, c* tend to decrease by orders of magnitude for increasing numbers of oxygenated functional groups, e.g. –OH, -OOH, -C(O)OH [*Compernolle et al.*, 2011]. This trend helps explain how the competition between fragmentation and functionalization during BVOC oxidation is a significant factor that determines how much SOA is produced. Typically, the higher the fraction of parent BVOC that is functionalized, the more SOA will be made due to a larger fraction of products having lower c*. However, semi-volatile and even volatile products can participate in multiphase chemistry (i.e. reactions of these vapors on or in particles) that results in lower volatility products, and thus may have a substantial influence on the formation of SOA. Specifically, compounds with epoxide functional groups have been shown to be able to undergo reactive uptake [*Surratt et al.*, 2010] in particles, producing polyols or organosulfates that contribute to SOA mass. It has also been shown that semi-volatile hydroperoxide and aldehyde containing compounds are able to participate in multi-phase oligomerization reactions [*Gao et al.*, 2004], which result in significantly lower volatility molecules. Thus, compounds that were initially not thought to contribute to SOA are now being reconsidered as SOA precursor components [*Claeys et al.*, 2004]. A major question is to what extent is the SOA a result of Raoult's Law driven partitioning, based on the distribution of

compound volatilities produced by gas-phase oxidation chemistry, versus multi-phase chemistry involving a wider suite of the oxidation product space.

Testing theories of SOA formation remains difficult, especially on the atmospheric scale. Direct *in situ* measurements of SOA are now routinely possible but are limited in both location and time, and remote sensing methods (e.g. satellite derived aerosol optical depth) are not specific to SOA. Moreover, the expected atmospheric lifetime of SOA is on the order of days to weeks, which requires testing theories of SOA formation with chemical-transport models in the context of also uncertain or highly parameterized removal processes such as precipitation scavenging. Currently, such models exhibit a significant and persistent difference between the amount of measured and predicted SOA [*Heald et al.*, 2005; *Volkamer et al.*, 2006]. Additionally, there are substantial uncertainties in the sources, oxidation pathways, and properties of SOA, due to its extraordinary complexity: SOA is estimated to contain potentially >10,000 individual species [*Goldstein and Galbally*, 2007].

To robustly study the process of particle formation and growth from gas phase species, knowledge of compounds in both phases is required. This desired information, along with the intense complexity of the SOA, presents an analytical challenge. Measurements of the molecular composition of organic aerosol have typically relied on bulk elemental analysis or used techniques which only allow molecular fragments to be measured [*DeCarlo et al.*, 2006; *Kolesar et al.*, 2015; *Vaden et al.*, 2011]. While offline analysis of filter samples can provide greater molecular composition information [*Surratt et al.*, 2007; *Wang et al.*, 2005], it is unclear how the sample workup procedures (solvent extraction, derivatization, etc.) alter the composition of

aerosol components. Filter samples are often analyzed offline, creating a time delay between aerosol collection and analysis which could allow for further particle phase reactions to occur, resulting in artifacts [*Kristensen et al.*, 2016]. Moreover, filter sampling often requires a substantial quantity of sample with a slow time resolution, making it difficult to accurately track chemical composition changes [*Turpin et al.*, 1994] in response to environmental or chemical drivers such as temperature, relative humidity, or actinic flux.

Recent advances in instrumentation have allowed for measurements that were previously unavailable, and have helped progress the field. Namely, the development of the Filter Inlet for Gases and AEROsols (FIGAERO) inlet manifold [*Lopez-Hilfiker et al.*, 2014], when coupled to a high-resolution time-of-flight chemical ionization mass spectrometer (HR-ToF-CIMS) [*Lee et al.*, 2014], is capable of measuring both the gas and particle phase chemical composition in near-real time. The gas-phase is sampled directly into the mass spectrometer for analysis in real time while simultaneously drawing air across a filter through a separate port, adjacent to the mass spectrometer inlet, to collect particles for subsequent analysis. Once enough aerosol mass is collected for sufficient signal, typically about 0.5 μg, the filter is automatically moved beneath a heating tube, above the orifice to the HR-ToF-CIMS, and a stream of programmatically heated $N_2$ is flown over the aerosols in order to thermally desorb components from the condensed-phase into the gas-phase for detection. The thermal desorption temperature axis can be calibrated with compounds with known vapor pressures by scattering the vapor pressures versus the temperature at which the signal reaches a maximum during desorption, or $T_{max}$, and generating a calibration curve. Then the $T_{max}$ of compounds of interest can be compared to this curve, providing volatility information for these compounds. Consequently, not only can the FIGAERO HR-TOF-CIMS

provide compositional information of both the gas and particle phases, but it can also provide a measure of the c* of compounds in the particle phase. Thus, the combination of the FIGAERO and HR-TOF-CIMS allows for unique and comprehensive measurements of SOA formation.

Environmental simulation chambers are also a useful tool to simplify the number of reactions involved, thereby easing elucidation of the mechanistic pathways giving rise to SOA. As stated previously, the atmosphere is overwhelmingly complex, with innumerable reactants and products. Chambers allow specific combinations of reactant(s) and oxidant(s) to be studied under controlled and repeated conditions in order to target a specific oxidation pathway and the corresponding sensitivity of SOA to various perturbations. While chambers are not without drawbacks, namely that chamber walls act as a large sink of lower volatility material [*Zhang et al.*, 2014], these issues can be minimized by altering the operation of the chamber [*Shilling et al.*, 2008]. By utilizing reaction chambers in a purposeful manner, insights can be gained on the composition, properties, and quantity of products formed, providing valuable information in the quest to understand the formation, growth, and properties of SOA.

Many chamber experiments have been performed using isoprene as the starting BVOC. As the single most predominantly emitted BVOC annually [*Guenther et al.*, 1995], it has the potential to form a significant fraction of SOA globally, even at relatively low efficiency. However, there has been much debate about the extent and pathways of isoprene SOA formation, as the knowledge progressed from the initial belief that it did not make SOA [*Pandis et al.*, 1991], to identifying SOA formation via reactive uptake of semi-volatile material [*Paulot et al.*, 2009]. Isoprene has been observed to form SOA when reactive uptake is suppressed [*Kroll et al.*, 2006], but the

mechanism of this SOA formation was unknown. Despite the relatively small size of isoprene, its oxidation mechanism is quite complex [*Wennberg et al.*, 2018], and thus much about the products formed and their properties is still unknown.

While isoprene is important for global SOA formation and growth due to the sheer volume of its emissions, monoterpenes are more efficient at forming SOA despite their lower emission rate. α-Pinene alone is thought to account for ~50% of monoterpene emissions [*Guenther et al.*, 1995], therefore understanding its fate and contribution to SOA is easily motivated relative to the suite of other monoterpenes. While there is no doubt α -pinene forms SOA under a range of chemical conditions, significant questions remain regarding the efficiency of various pathways, the relative importance of gas-phase condensation compared to multi-phase accretion (oligomer formation) chemistry in forming SOA, and the overall phase-state and volatility [*Cappa and Wilson*, 2011; *Loza et al.*, 2013; *Saleh et al.*, 2013; *Trump and Donahue*, 2014; *Vaden et al.*, 2011]. These questions are effectively coupled by the type of chemistry forming and occurring in the SOA [*Huang et al.*, 2018; *Koop et al.*, 2011]: the higher the oligomer content, the more viscous the aerosol is and also the lower its volatility. Understanding these pathways and properties has important implications for predicting the evolution of SOA in the atmosphere over its lifetime.

Complicating the matter even further, it is still unclear how much SOA is made in various environments from various BVOC + oxidant pairings. The classic way to represent SOA yields, or the amount of SOA observed relative to the amount of parent BVOC generated is to plot the yield versus the concentration of SOA. The theory is that, as the concentration of SOA increases

the surface area also increases, allowing for increasingly volatile material to condense and thus increasing the yield. This yield curve has been shown many times for α-pinene +$O_3$ [*Hallquist et al.*, 2009] and assumes that SOA is predominantly composed of semi-volatile material. However, as experiments and instrumentation evolved, it has been shown that at lower SOA concentrations that are more relevant to the atmosphere (0-10 μg $m^{-3}$), the traditional yield curve does not apply [*Shilling et al.*, 2008], and that the SOA formation and growth is dominated by the condensation of Highly oxygenated Organic Molecules (HOM) with either low or extremely low volatility (LVOC or ELVOC) [*Ehn et al.*, 2014]. Additionally, it has been shown that SOA does not evaporate rapidly when the surrounding vapor phase is completely removed as would be expected based on the traditional view of SOA formation [*Vaden et al.*, 2011]. These more recent studies all suggest that the traditional view of the yield curve and the formation of SOA being driven by the condensation of semi-volatile material is incorrect, although no one has yet tried or been able to study these issues at a molecular composition level.

The research described herein utilizes the relatively new FIGAERO HR-TOF-CIMS coupling, in order to address outstanding questions in the field of SOA formation from BVOC oxidation. This instrumentation was utilized in the laboratory at the University of Washington, and taken to the Pacific Northwest National Laboratory in Richland, WA on three several (6+) week long excursions to make a series of measurements examining the products formed and volatility of those products from a variety of parent BVOC and oxidant pairings. A multi-pronged approach utilizing measurements, chemical kinetics box modeling, and quantum chemical calculations is adopted to answer the main overarching questions:

(1) *What are the products formed from BVOC oxidation that influence SOA formation?*

(2) *What are the volatilities of those products?*

(3) *What is the mechanism of formation for those products?*

In chapters 2 and 3, I focus on the formation of SOA from isoprene. Chapter 2 focuses on the products formed from isoprene and compares and contrasts the SOA formed in "pristine" conditions relative to "polluted" conditions where NO, a common anthropogenic emission, is added to the chamber. Chapter 3 utilizes a combination of measurements, modeling, and quantum chemical calculations to evaluate the chamber conditions and extrapolate to atmospheric conditions in order to determine the true composition and properties of isoprene SOA. Both chapters 2 and 3 build upon previous knowledge of the oxidation mechanism of isoprene.

In chapter 4 I investigate the properties, namely the volatility, of α-pinene SOA formed via reaction with $O_3$. As mentioned previously, phase-state and oligomerization are coupled and difficult to disentangle. We present novel methods that both replicate previous findings with markedly different methods, and expand upon these previous works to more quantitatively assess the interplay between these two properties.

References

Boucher, O., D. Randall, P. Artaxo, C. Bretherton, G. Feingold, P. Forster, V.-M. Kerminen, Y. Kondo, H. Liao, U. Lohmann, P. Rasch, S.K. Satheesh, S. Sherwood, B. Stevens and X.Y. Zhang (2013), Clouds and Aerosols, in *Climate Change 2013: The Physical Science Basis. Contribution of Working Group I to the Fifth Assessment Report of the Intergovernmental Panel on Climate Change*, edited by T. F. Stocker, D. Qin, G.-K. Plattner, M. Tignor, S.K. Allen, J. Boschung, A. Nauels, Y. Xia, V. Bex and P.M. Midgley, pp. 571-632, Cambridge University Press, Cambridge, United Kingdom and New York, NY, USA.

Brock, C. A., P. Hamill, J. C. Wilson, H. H. Jonsson, and K. R. Chan (1995), Particle Formation in the Upper Tropical Troposphere: A Source of Nuclei for the Stratospheric Aerosol, *Science*, *270*(5242), 1650-1653.

Cappa, C. D., and K. R. Wilson (2011), Evolution of organic aerosol mass spectra upon heating: implications for OA phase and partitioning behavior, *Atmospheric Chemistry and Physics*, *11*(5), 1895-1911.

Claeys, M., W. Wang, A. C. Ion, I. Kourtchev, A. Gelencser, and W. Maenhaut (2004), Formation of secondary organic aerosols from isoprene and its gas-phase oxidation products through reaction with hydrogen peroxide, *Atmospheric Environment*, *38*(25), 4093-4098.

Compernolle, S., K. Ceulemans, and J. F. Muller (2011), EVAPORATION: a new vapour pressure estimation method for organic molecules including non-additivity and intramolecular interactions, *Atmos. Chem. Phys.*, *11*(18), 9431-9450.

DeCarlo, P. F., et al. (2006), Field-deployable, high-resolution, time-of-flight aerosol mass spectrometer, *Anal. Chem.*, *78*(24), 8281-8289.

Ehn, M., et al. (2014), A large source of low-volatility secondary organic aerosol, *Nature*, *506*(7489), 476-479.

Gao, S., M. Keywood, N. L. Ng, J. Surratt, V. Varutbangkul, R. Bahreini, R. C. Flagan, and J. H. Seinfeld (2004), Low-molecular-weight and oligomeric components in secondary organic aerosol from the ozonolysis of cycloalkenes and alpha-pinene, *J. Phys. Chem. A*, *108*(46), 10147-10164.

Goldstein, A. H., and I. E. Galbally (2007), Known and unexplored organic constituents in the earth's atmosphere, *Environmental science & technology*, *41*(5), 1514-1521.

Guenther, A., et al. (1995), A global model of natural volatile organic compound emissions, *Journal of Geophysical Research*, *100*(D5), 8873-8892.

Hallquist, M., et al. (2009), The formation, properties and impact of secondary organic aerosol: current and emerging issues, *Atmospheric Chemistry and Physics*, *9*(14), 5155-5236.

Heald, C. L., D. J. Jacob, R. J. Park, L. M. Russell, B. J. Huebert, J. H. Seinfeld, H. Liao, and R. J. Weber (2005), A large organic aerosol source in the free troposphere missing from current models, *Geophys. Res. Lett.*, *32*(18).

Huang, W., H. Saathoff, A. Pajunoja, X. L. Shen, K. H. Naumann, R. Wagner, A. Virtanen, T. Leisner, and C. Mohr (2018), alpha-Pinene secondary organic aerosol at low temperature: chemical composition and implications for particle viscosity, *Atmospheric Chemistry and Physics*, *18*(4), 2883-2898.

Jimenez, J. L., et al. (2009), Evolution of organic aerosols in the atmosphere, *Science*, *326*(5959), 1525-1529.

Kolesar, K. R., Z. Y. Li, K. R. Wilson, and C. D. Cappa (2015), Heating-Induced Evaporation of Nine Different Secondary Organic Aerosol Types, *Environmental science & technology*, *49*(20), 12242-12252.

Koop, T., J. Bookhold, M. Shiraiwa, and U. Poschl (2011), Glass transition and phase state of organic compounds: dependency on molecular properties and implications for secondary organic aerosols in the atmosphere, *Phys. Chem. Chem. Phys.*, *13*(43), 19238-19255.

Kristensen, K., M. Bilde, P. P. Aalto, T. Petaja, and M. Glasius (2016), Denuder/filter sampling of organic acids and organosulfates at urban and boreal forest sites: Gas/particle distribution and possible sampling artifacts, *Atmospheric Environment*, *130*, 36-53.

Kroll, J. H., N. L. Ng, S. M. Murphy, R. C. Flagan, and J. H. Seinfeld (2006), Secondary organic aerosol formation from isoprene photooxidation, *Environ. Sci. Technol.*, *40*(6), 1869-1877.

Lee, B. H., F. D. Lopez-Hilfiker, C. Mohr, T. Kurten, D. R. Worsnop, and J. A. Thornton (2014), An iodide-adduct high-resolution time-of-flight chemical-ionization mass spectrometer: application to atmospheric inorganic and organic compounds, *Environ. Sci. Technol.*, *48*(11), 6309-6317.

Lopez-Hilfiker, F. D., et al. (2014), A novel method for online analysis of gas and particle composition: description and evaluation of a Filter Inlet for Gases and AEROsols (FIGAERO), *Atmos. Meas. Tech.*, *7*(4), 983-1001.

Loza, C. L., M. M. Coggon, T. B. Nguyen, A. Zuend, R. C. Flagan, and J. H. Seinfeld (2013), On the Mixing and Evaporation of Secondary Organic Aerosol Components, *Environmental science & technology*, *47*(12), 6173-6180.

Pandis, S. N., S. E. Paulson, J. H. Seinfeld, and R. C. Flagan (1991), Aerosol formation in the photooxidation of isoprene and beta-pinene, *Atmospheric Environment Part a-General Topics*, *25*(5-6), 997-1008.

Pankow, J. F. (1994), An absorption-model of the gas aerosol partitioning involved in the formation of secondary organic aerosol *Atmos. Environ.*, *28*(2), 189-193.

Paulot, F., J. D. Crounse, H. G. Kjaergaard, A. Kurten, J. M. St Clair, J. H. Seinfeld, and P. O. Wennberg (2009), Unexpected epoxide formation in the gas-phase photooxidation of isoprene, *Science*, *325*(5941), 730-733.

Riipinen, I., et al. (2011), Organic condensation: a vital link connecting aerosol formation to cloud condensation nuclei (CCN) concentrations, *Atmospheric Chemistry and Physics*, *11*(8), 3865-3878.

Saleh, R., N. M. Donahue, and A. L. Robinson (2013), Time scales for gas-particle partitioning equilibration of secondary organic aerosol formed from alpha-pinene ozonolysis, *Environ. Sci. Technol.*, *47*(11), 5588-5594.

Shilling, J. E., Q. Chen, S. M. King, T. Rosenoern, J. H. Kroll, D. R. Worsnop, K. A. McKinney, and S. T. Martin (2008), Particle mass yield in secondary organic aerosol formed by the dark ozonolysis of alpha-pinene, *Atmos. Chem. Phys.*, *8*(7), 2073-2088.

Spracklen, D. V., et al. (2011), Aerosol mass spectrometer constraint on the global secondary organic aerosol budget, *Atmos. Chem. Phys.*, *11*(23), 12109-12136.

Surratt, J. D., M. Lewandowski, J. H. Offenberg, M. Jaoui, T. E. Kleindienst, E. O. Edney, and J. H. Seinfeld (2007), Effect of acidity on secondary organic aerosol formation from isoprene, *Environ. Sci. Technol.*, *41*(15), 5363-5369.

Surratt, J. D., A. W. H. Chan, N. C. Eddingsaas, M. N. Chan, C. L. Loza, A. J. Kwan, S. P. Hersey, R. C. Flagan, P. O. Wennberg, and J. H. Seinfeld (2010), Reactive intermediates revealed in secondary organic aerosol formation from isoprene, *Proc. Natl. Acad. Sci. U. S. A.*, *107*(15), 6640-6645.

Trump, E. R., and N. M. Donahue (2014), Oligomer formation within secondary organic aerosols: equilibrium and dynamic considerations, *Atmospheric Chemistry and Physics*, *14*(7), 3691-3701.

Turpin, B. J., J. J. Huntzicker, and S. V. Hering (1994), Investigation of organic aerosol sampling artifacts in the Los-Angeles basin *Atmospheric Environment*, *28*(19), 3061-3071.

Vaden, T. D., D. Imre, J. Beranek, M. Shrivastava, and A. Zelenyuk (2011), Evaporation kinetics and phase of laboratory and ambient secondary organic aerosol, *Proc. Natl. Acad. Sci. U. S. A.*, *108*(6), 2190-2195.

Volkamer, R., J. L. Jimenez, F. San Martini, K. Dzepina, Q. Zhang, D. Salcedo, L. T. Molina, D. R. Worsnop, and M. J. Molina (2006), Secondary organic aerosol formation from anthropogenic air pollution: Rapid and higher than expected, *Geophys. Res. Lett.*, *33*(17).

Wang, W., I. Kourtchev, B. Graham, J. Cafmeyer, W. Maenhaut, and M. Claeys (2005), Characterization of oxygenated derivatives of isoprene related to 2-methyltetrols in Amazonian aerosols using trimethylsilylation and gas chromatography/ion trap mass spectrometry, *Rapid Commun. Mass Spectrom.*, *19*(10), 1343-1351.

Wennberg, P. O., et al. (2018), Gas-Phase Reactions of Isoprene and Its Major Oxidation Products, *Chem. Rev.*, *118*(7), 3337-3390.

Zhang, Q., et al. (2007), Ubiquity and dominance of oxygenated species in organic aerosols in anthropogenically-influenced Northern Hemisphere midlatitudes, *Geophys. Res. Lett.*, *34*(13), L13801.

Zhang, X., C. D. Cappa, S. H. Jathar, R. C. McVay, J. J. Ensberg, M. J. Kleeman, and J. H. Seinfeld (2014), Influence of vapor wall loss in laboratory chambers on yields of secondary organic aerosol, *Proc. Natl. Acad. Sci. U. S. A.*, *111*(16), 5802-5807.

# Chapter 2. MOLECULAR COMPOSITION AND VOLATILITY OF ISOPRENE PHOTOCHEMICAL OXIDATION SECONDARY ORGANIC AEROSOL UNDER LOW AND HIGH $NO_X$ CONDITIONS[1]

Abstract

We present measurements of secondary organic aerosol (SOA) formation from isoprene photochemical oxidation in an environmental simulation chamber at a variety of oxidant conditions and using dry neutral seed particles to suppress acid catalyzed multiphase chemistry. A high-resolution time-of-flight chemical ionization mass spectrometer (HRToF-CIMS) utilizing iodide-adduct ionization coupled to the Filter Inlet for Gases and AEROsols (FIGAERO) allowed for simultaneous online sampling of the gas and particle composition. Under high $HO_2$ and low NO conditions, highly oxygenated (O:C $\geq$ 1) $C_5$ compounds were major components (~50%) of the SOA. The SOA composition and effective volatility evolved both as a function of time and as a function of input NO concentrations. Organic nitrates increased in both the gas- and particle-phases as input NO increased, but the dominant non-nitrate particle-phase components monotonically decreased. We use comparisons of measured and predicted gas-particle partitioning of individual components to assess the validity of literature-based group-contribution methods for estimating saturation vapor concentrations. While there is evidence for equilibrium partitioning being achieved on the chamber residence time scale (5.2 hours) for some

[1] Reprinted with permission from: D'Ambro, E. L., Lee, B. H., Liu, J., Shilling, J. E., Gaston, C. J., Lopez-Hilfiker, F. D., Schobesberger, S., Zaveri, R. A., Mohr, C., Lutz, A., Zhang, Z., Gold, A., Surratt, J. D., Rivera-Rios, J. C., Keutsch, F. N., and Thornton, J. A.: Molecular composition and volatility of isoprene photochemical oxidation secondary organic aerosol under low- and high-NOx conditions, Atmos. Chem. Phys., 17, 159-174, doi: 10.5194/acp-17-159-2017, 2017.

individual components, significant errors in group-contribution methods are revealed. In addition, >30% of the SOA mass, detected as low-molecular weight semi-volatile compounds, cannot be reconciled with equilibrium partitioning. These compounds desorb from the FIGAERO at unexpectedly high temperatures given their molecular composition, indicative of thermal decomposition of effectively lower volatility components such as larger molecular weight oligomers.

## 2.1 INTRODUCTION

Atmospheric aerosol particles reduce visibility, adversely affect human health, and have uncertain overall effects on global climate [*Poschl*, 2005], with particles smaller than 1 μm in diameter playing important roles. Submicron particles typically contain a significant fraction of organic material, on the order of 20-90% [*Jimenez et al.*, 2009; *Zhang et al.*, 2007]. Particulate organic material can be emitted directly to the atmosphere, known as primary organic aerosol, or formed from the gas-to-particle conversion of volatile organic compound (VOC) oxidation products which can partition [*Donahue et al.*, 2011; *Riipinen et al.*, 2011] or react heterogeneously [*Docherty et al.*, 2005; *Gaston et al.*, 2014; *Jang et al.*, 2002; *Surratt et al.*, 2007; *Surratt et al.*, 2006] on existing particles, or homogeneously nucleate to form new particles [*Kirkby et al.*, 2016]. This condensed phase organic material arising from gas to particle conversion is known as secondary organic aerosol (SOA).

Biogenic VOC (BVOC) contribute significantly to SOA. Emitted at rates of 500 TgC $year^{-1}$ [*Guenther et al.*, 2012] and with a high reactivity, isoprene ($C_5H_8$) has the potential to contribute substantially to SOA, even if the overall conversion is inefficient. Initially, the observed products

of isoprene oxidation were of high volatility, which led to the hypothesis that isoprene did not generate SOA [*Pandis et al.*, 1991]. However, subsequent chamber experiments showed that the yield of SOA from isoprene photochemical oxidation can range from <1-29% with the highest yields achieved either with acidic aqueous seed particles [*Surratt et al.*, 2010] or as a transient during successive oxidative aging [*Kroll et al.*, 2006]. Chemically speciated measurements of atmospheric aerosol components in an isoprene-rich environment identified polyol compounds likely formed from isoprene oxidation [*Claeys et al.*, 2004; *Paulot et al.*, 2009b]. Subsequent chamber studies have shown that, under low NO conditions, isoprene reacts with OH followed by $HO_2$ to form a hydroxy hydroperoxide, ISOPOOH, which further reacts with OH to form the isoprene epoxy diol, IEPOX (see Figure 2.1) [*Paulot et al.*, 2009a; *Paulot et al.*, 2009b]. Both laboratory and field studies suggest that IEPOX plays an important role in the formation of isoprene SOA (iSOA) *via* acid catalyzed heterogeneous reactions on deliquesced particles [*Gaston et al.*, 2014; *Lin et al.*, 2013a; *Lin et al.*, 2014; *Lin et al.*, 2012; *Lin et al.*, 2013b; *Liu et al.*, 2014; *Paulot et al.*, 2009b; *Surratt et al.*, 2010; *Surratt et al.*, 2006]. In the absence of acidic seed particles, iSOA yields have generally been low, but functional group analyses suggested a significant contribution of peroxide moieties and a complex dependence upon $NO_x$ [*Dommen et al.*, 2006; *King et al.*, 2010; *Kroll et al.*, 2005; 2006; *Sato et al.*, 2011; *Xu et al.*, 2014; *Zhang et al.*, 2011]. Despite these advances, a comprehensive molecular characterization of photochemical iSOA has been lacking.

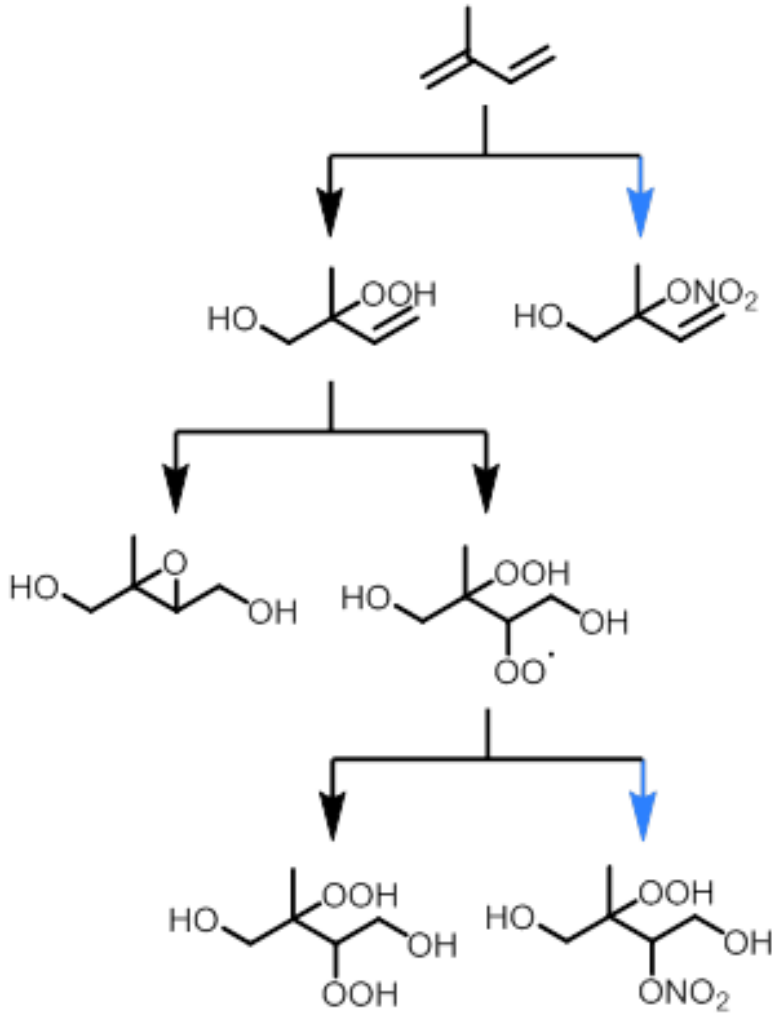


Figure 2.1 A simplified schematic of isoprene and its major oxidation products. Products formed in the presence of $NO_x$ are identified with blue arrows.

Much attention has been focused on the formation of SOA derived from IEPOX chemistry; however, understanding the formation of SOA from pathways other than IEPOX is important for quantifying SOA in environments where the SOA is likely formed via other mechanisms due to the lack of acidic seed. Three recent studies have performed photochemical oxidation on either ISOPOOH [*Krechmer et al.*, 2015; *Riva et al.*, 2016] or both isoprene and ISOPOOH [*Liu et al.*, 2016] in the absence of wet acidic seed in order to study the mechanism of iSOA formation

when the IEPOX pathway is suppressed. These studies identified several $C_5H_{8-12}O_{4-8}$ compounds in both the gas- [*Krechmer et al.*, 2015] and particle- [*Liu et al.*, 2016; *Riva et al.*, 2016] phases. Liu et al. [2016] found that under the photochemical conditions of their chamber, the most abundant compound in the particle-phase was $C_5H_{12}O_6$, $ISOP(OOH)_2$, presumed to be a dihydroxy dihydroperoxide formed from the reaction of an organic peroxy radical ($RO_2$) derived from ISOPOOH + OH followed by further reaction with hydroperoxy radicals ($HO_2$) (see Figure 2.1) [*Liu et al.*, 2016]. However, the iSOA yields starting from isoprene reported by Liu et al. [2016] were substantially higher than those starting from ISOPOOH alone as reported by Krechmer et al. [2015], and generally higher than most previous iSOA studies in the absence of deliquesced acidic seed particles [*Dommen et al.*, 2006; *King et al.*, 2010; *Xu et al.*, 2014].

Furthermore, there is significant interest in understanding how anthropogenic pollutants affect SOA yields [*Shilling et al.*, 2013; *Weber et al.*, 2007; *Xu et al.*, 2015], and there have been several chamber studies to understand the role of $NO_x$ specifically on iSOA yields [*Dommen et al.*, 2006; *King et al.*, 2010; *Kroll et al.*, 2005; 2006; *Xu et al.*, 2014; *Zhang et al.*, 2011]. The general effect of $NO_x$ on the newly discovered non-IEPOX SOA system has been described previously [*Liu et al.*, 2016]. The total SOA mass concentration was shown to be stable for input NO concentrations from 0-20 ppb, with a sharp decrease in SOA mass concentration at the highest input NO concentration (50 ppb). While these studies have advanced our knowledge of the possible mechanisms of iSOA formation, in order to more accurately assess the environments in which this pathway will operate, it remains important to further quantify (*a*) the branching between the formation of the $C_5H_{11}O_6$ peroxy radical versus the formation of IEPOX from the reaction between ISOPOOH and OH, (*b*) the fate of the $C_5H_{11}O_6$ peroxy radical under various

environmental conditions, as well as (*c*) the volatility of the SOA formed under various environmental conditions and (*d*) the role of the broader suite of oxidation products in the formation of this non-IEPOX SOA.

We present laboratory chamber studies of the gas- and particle-phase composition resulting from both the low- and high-$NO_x$ photochemical oxidation of isoprene with the goal of better understanding the chemical mechanisms of iSOA formation and the evolution of its volatility and composition over time, specifically points (*c*) and (*d*) above. We compare the observed gas-particle partitioning of several oxidation products to an assumption of equilibrium partitioning theory. In this analysis, we use the measured thermograms of particle-phase components to assess commonly used group-contribution methods for estimating saturation vapor concentrations, C*. Moreover, we use a combined composition-volatility framework [*Lopez-Hilfiker et al.*, 2015] to quantify the presence of more refractory oligomer-like components of the SOA. From these analyses we find (*i*) the direct effect of higher $NO_x$ (i.e. all else being constant) is a suppression of iSOA yields at very high input NO concentrations (50 ppb); (*ii*) a large shift to more refractory components and N-containing products with increasing $NO_x$; (*iii*) a generally important role for oligomerization reactions and other multiphase chemistry irrespective of $NO_x$ concentrations, even at relatively low precursor concentrations, likely involving a broad suite of isoprene oxidation products.

## 2.2 EXPERIMENTAL METHODS

### 2.2.1 *Chamber Operation*

Experiments were performed in Pacific Northwest National Laboratory's (PNNL) 10.6 $m^3$ polytetrafluoroethylene (PTFE) environmental chamber. The chamber has been described in detail elsewhere [*Liu et al.*, 2012], and a portion of the data discussed herein were obtained from the same experiments described in Liu et al. [2016]. Additional experiments with identical chamber operation were conducted to examine a wider range of oxidant conditions. The chamber was primarily operated in continuous-flow mode where reactants were continuously delivered at a constant rate to allow reaction precursors and products to reach steady state concentrations [*Shilling et al.*, 2008]. The extent of reaction is controlled by oxidant concentrations and the residence time of air within the chamber, typically 5.2 hours. We also discuss a time-dependent "batch mode" experiment also performed during 2015 for comparison purposes where the chamber is filled with a fixed amount of isoprene and oxidant precursors in the dark and then the chemistry is followed for ~6 hours after turning on the UV-VIS lights.

Isoprene was delivered into the chamber via a calibrated cylinder (Matheson, 20 ppm in nitrogen) and mass flow controller. OH radicals were generated by the photolysis of $H_2O_2$. An aqueous solution of $H_2O_2$ was introduced into the chamber via an automated syringe operated at various flow rates to achieve a range of $H_2O_2$, and therefore OH and $HO_2$, concentrations. Quasi-monodisperse, effloresced 50 nm diameter solid ammonium sulfate seed particles were continually added to facilitate the partitioning of oxidized VOC onto particle surfaces as opposed to chamber walls [*Zhang et al.*, 2014] for the formation of SOA. When desired, NO was added via a calibrated cylinder (Matheson, 500 ppm in nitrogen) and mass flow controller. During the

continuous-flow experiments RH was controlled to ~50 %, while the batch mode experiment was performed under dry conditions (~10% RH).

### 2.2.2 *Instrumentation*

A suite of online instruments was utilized to monitor gas- and particle-phase composition. Ozone and $NO/NO_2/NO_x$ concentrations were measured using commercial instruments (Thermo Environmental Instruments models 49C and 42C, respectively). Aerosol number and volume concentrations were measured with a scanning mobility particle sizer (SMPS, TSI model 3936). An Aerodyne high-resolution time-of-flight aerosol mass spectrometer (HRToF-AMS) monitored bulk submicron organic and inorganic aerosol composition. The evolution of isoprene was monitored with an Ionicon proton-transfer-reaction mass spectrometer (PTR-MS).

A high-resolution time-of-flight chemical ionization mass spectrometer (HRToF-CIMS) using iodide-adduct ionization as described previously [*B H Lee et al.*, 2014] was coupled to a Filter Inlet for Gases and AEROsols (FIGAERO) [*Lopez-Hilfiker et al.*, 2014] for measuring a suite of oxygenated products in the gas- and particle-phase. The HRToF-CIMS provides measurements of molecular composition, although cannot provide structural information and therefore cannot differentiate between isobaric compounds. Briefly, the FIGAERO is an inlet manifold that allowed for measurement of both gas- and particle-phase molecular composition with approximately hourly time resolution. To collect particles, chamber air was drawn through a 1.27 cm OD (2014) or 0.635 cm OD (2015) stainless steel tube at 2.5 slpm across a Teflon filter (Zefluor® 24 mm diameter, 2.0 μm pore size, Pall Corp.) for 31 (2014), 42 (2015), or 25 (batch) minutes. Through a separate inlet chamber air was simultaneously sampled at 22 slpm (2014) or

12 slpm (2015) through a 1.9 cm OD, 2 m long (2014) or 1.1 m long (2015) PTFE tube for gas-phase analysis. The gas-phase analysis required sub-sampling a portion of the flow after dilution to maintain linearity of response in the chemical ionization. After a particle collection period, gas-phase analysis ends and the filter containing collected particles is actuated to a location downstream of an ultra-high purity (UHP) $N_2$ source and immediately upstream of an orifice into the HRToF-CIMS. UHP $N_2$, continually passed across the filter at 2.5 slpm, was heated at a rate of 10 or 15 °C $min^{-1}$ to 200 °C for a temperature-programmed thermal desorption and then kept at 200 °C for the remainder of the desorption time (60 min total 2014, 70 min 2015, 40 min batch). The coupled FIGAERO HRToF-CIMS will be referred to herein as the FIGAERO-CIMS. The temperature axis of the FIGAERO thermograms is calibrated with compounds having known enthalpies of sublimation [*Lopez-Hilfiker et al.*, 2014]. Lopez-Hilfiker et al. [2014] have shown that pure compounds, or mixtures of non-interacting compounds, have consistent thermogram shapes throughout time and reach a maximum signal at characteristic temperature ($T_{max}$) which can be related to their enthalpies of sublimation and therefore sub-cooled pure component vapor pressures. In this way, the $T_{max}$ of detected compounds can be used to estimate their C* at ambient conditions even if the structure is unknown.

### 2.2.3 *Experimental Overview*

Figure 2.2 presents a time series of all steady-state experiments. The left and right columns contain experiments conducted in May of 2014 and 2015, respectively. The top panels show the input concentrations of isoprene, hydrogen peroxide, and NO, as well as the isoprene and $C_5H_{10}O_3$ (ISOPOOH + IEPOX) concentrations measured at the chamber output. The phrases "input NO", "input $H_2O_2$", and "input isoprene", refer to the concentration of precursor that

would be in the chamber if there were no loss mechanisms except for dilution. For example, in Figure 2.2, top, the input isoprene (dashed green line) is flat, while the amount of isoprene remaining in the chamber, i.e. what is measured with the PTR-MS (solid green line), varies depending on the chamber chemical environment. Thus, while we state that we input 0-50 ppb NO in the chamber, in reality steady-state NO concentrations in the chamber are much lower for the majority of the chamber residence time, in fact, usually below the detection limit of the NO analyzer due to loss mechanisms such as photochemical conversion to $NO_2$ and nitrate formation.

In Figure 2.2 (top row) we show the time series of gas-phase species: input concentrations of isoprene which were generally similar across both years (26 ppbv 2014, 20 ppbv 2015), NO, and $H_2O_2$, as well as gas-phase measurements of the isoprene remaining in the chamber and $C_5H_{10}O_3$. As discussed above, the HRToF-CIMS cannot differentiate isobaric compounds and thus $C_5H_{10}O_3$ represents the sum of ISOPOOH and IEPOX. It is important to note that while we are suppressing the uptake of IEPOX into the particle-phase, it is still produced at a yield of about 70-80% [*St Clair et al.*, 2016] from the reaction of ISOPOOH + OH. The middle row shows the organic aerosol (OA) as measured by the AMS with the AMS blanks highlighted in black squares. Steady-state periods for analysis were determined by an unchanging OA concentration over a period of 2 or more hours typically at least 24 hours after an intentional change in experimental conditions. The bottom panels show the time series of a few dominant particle-phase components as measured by the FIGAERO-CIMS: $C_5H_{12}O_6$, $C_5H_{12}O_5$, and $C_5H_{11}NO_7$. The organic nitrate is scaled by a factor of 20 to show its time series on the same scale, although it is near zero when NO is not added to the chamber. The grey shaded areas in the left column

indicate when there was a chamber cleaning followed by a dark $NO_3$ + isoprene experiment that is not discussed here. By systematically scanning $H_2O_2$ and NO concentrations independently, we were able to test the response and composition of the SOA across a range of oxidant conditions, ranging from more pristine to polluted in terms of $NO_x$ concentrations.

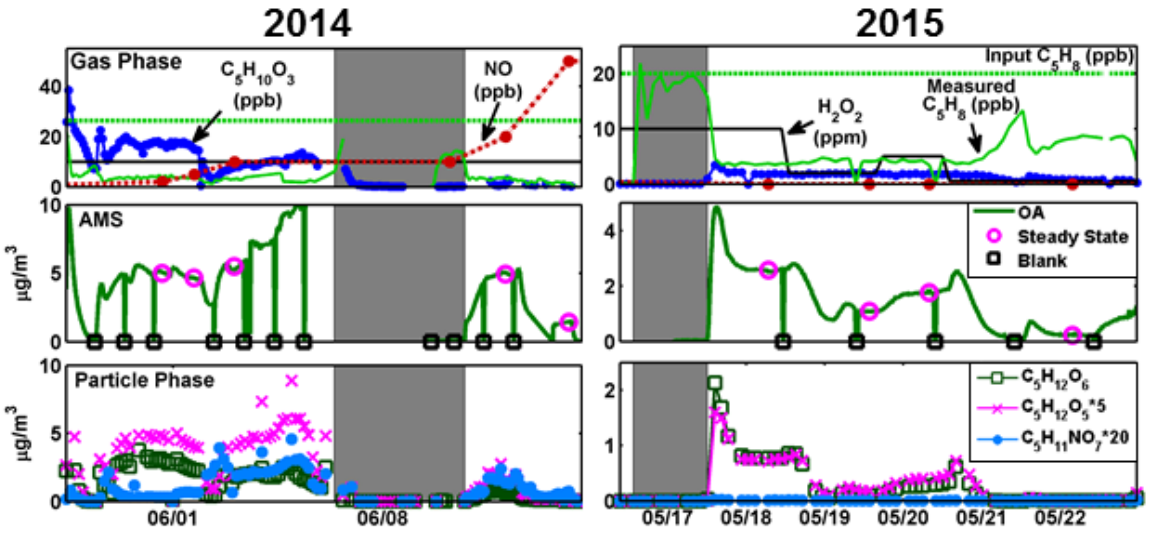


Figure 2.2 Overview of the 2014 and 2015 measurements taken at PNNL. The left column is data from the 2014 campaign, the right column is 2015. The top row shows gas-phase compounds measured by the PTR-MS and FIGAERO-CIMS, as well as input concentrations of $H_2O_2$, NO, and isoprene. Middle row shows the OA as measured by the AMS. Steady state periods are shown within magenta circles, AMS blanks as black squares. Select particle phase species measured by the FIGAERO-CIMS are in the bottom row. Grey shaded areas in each column indicate when chamber lights were off for chamber cleaning and a dark $NO_3$ experiment (in 2014) which is not discussed here. Note that the axis limits are not the same due to a wide range in concentrations across years, while $C_5H_{12}O_5$ has been enhanced 5x and $C_5H_{11}NO_7$ has been enhanced 20x in the bottom rows to clearly show the behavior of each species on the same axis.

All AMS and particle-phase FIGAERO-CIMS data have been multiplied by a factor of 1.5 to correct for particle wall losses as described in Liu et al. [2016], and where we also describe the effect of seed particle surface area concentrations on SOA mass yields from this system in order to assess indirectly the role of vapor wall loss. The effect of added seed was minimal and as such data shown here have not been corrected for vapor wall losses. Operating the chamber in continuous flow mode possibly reduces the net flux of organic compounds to the walls, at least for low volatility to semi volatile compounds, as some degree of equilibration can occur [*Liu et al.*, 2016; *Shilling et al.*, 2008]. Nonetheless, our vapor concentration data may be biased low due to some amount of loss to the walls.

## 2.3 Results & Discussion

### 2.3.1 *Effect of $NO_x$ on Major Gas- and Particle-Phase Species*

The gas- [*Krechmer et al.*, 2015] and particle-phase [*Liu et al.*, 2016; *Riva et al.*, 2016] species detected from isoprene photochemical oxidation when examining the non-IEPOX SOA pathway have been discussed previously. These studies identified several $C_5H_{8\text{-}12}O_{4\text{-}8}$ compounds, among many others, and the findings presented here are broadly consistent. Figure 2.3 summarizes all compounds measured as an iodide-adduct in both the gas- (top) and particle- (bottom) phases at both low (left) and high (right) input NO (20 ppb) for average spectra at steady state. The square root of the background subtracted signals were taken to show the dynamic range and then normalized to the maximum signal within each individual plot. Green bars represent organic compounds with formula $C_xH_yO_zI$-, while blue are organic nitrates (OrgN) with formula $C_xH_yNO_zI$-. It is possible that dinitrates were measured, but due to their occurrence at masses where non-nitrates would be observed, they are difficult to conclusively identify and thus are not

presented here. Major peaks are labeled with letters corresponding to compounds in Table 2.1. It is important to note that while the same molecular composition may be present in both the gas- and particle-phase, we do not suggest that they all exist as the same structure in each phase, although some likely do. We will discuss this further in later sections.

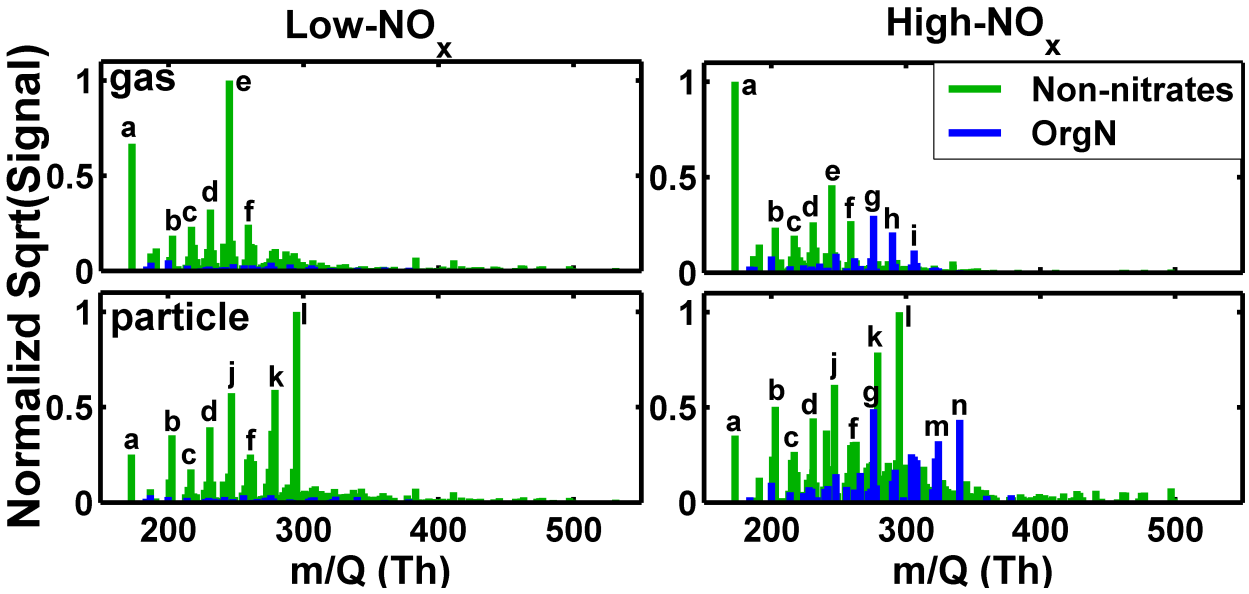


Figure 2.3 Mass spectra for compounds with composition $C_xH_yO_zI^-$ (green) and $C_xH_yNO_zI^-$ (blue) at low (left) and high (right) NO input in both the gas- (top) and particle- (bottom) phases. Bars are sized by the square root of signal (counts $s^{-1}$ for the gas-phase, counts for the particle-phase) to show the dynamic range. Major components are labeled with letters corresponding to those found in Table 1.

Table 2.1 Gas- and particle-phase compounds detailed in the mass spectra in Figure 2.3 (top). Many molecular compositions are observed in both the gas- and particle-phase. If the composition is observed in the particle phase, a $T_{max}$ is listed at both low (0 ppb input NO) and high (20 ppb input NO) $NO_x$. The desorption shape is also listed and is consistent across $NO_x$ conditions. The significance of the $T_{max}$ and desorption shape are discussed in detail in the text. If the compound is only detected in the gas phase, "NA" is listed in the $T_{max}$ and thermogram columns, indicating that those values are not applicable.

| Letter | Mass | Molecular Composition | Particle-phase $T_{max}$, Low $NO_x$ | Particle-phase $T_{max}$, High $NO_x$ | thermogram shape |
|---|---|---|---|---|---|
| a | 172.9105 | $CH_2O_2I$- | 87 | 94 | broad |
| b | 202.9211 | $C_2H_4O_3I$- | 113 | 115 | broad |
| c | 216.9367 | $C_3H_6O_3I$- | 76 | 100 | broad |
| d | 230.9524 | $C_4H_8O_3I$- | 87 | 115 | broad |
| e | 244.968 | $C_5H_{10}O_3I$- | NA | NA | NA |
| f | 258.9473 | $C_5H_8O_4I$- | 76, 111 | 70, 115 | double |
| g | 275.9374 | $C_4H_7NO_5I$- | 88 | 115 | broad |
| h | 289.9531 | $C_5H_9NO_5I$- | NA | NA | NA |
| i | 305.948 | $C_5H_9NO_6I$- | NA | NA | NA |
| j | 246.9473 | $C_4H_8O_4I$- | 95 | 110 | broad |
| k | 278.9735 | $C_5H_{12}O_5I$- | 60 | 48 | Gaussian |
| l | 294.9684 | $C_5H_{12}O_6I$- | 63 | 56 | Gaussian |
| m | 323.9586 | $C_5H_{11}NO_7I$- | 72 | 50 | Gaussian |
| n | 339.9535 | $C_5H_{11}NO_8I$- | 53 | 45 | Gaussian |

From Figure 2.3, the two largest signals detected by the FIGAERO-CIMS in the gas-phase at both low and high input NO are $CH_2O_2$ (presumably formic acid) and $C_5H_{10}O_3$ (presumably the sum of IEPOX and ISOPOOH). With the addition of NO, the $CH_2O_2$ signal becomes noticeably larger than that of $C_5H_{10}O_3$, likely due to increased fragmentation. Even without adding NO to the chamber there is still a small amount of $NO_x$ present, likely from photolysis of inorganic

nitrate on the chamber walls, as we measure non-negligible OrgN concentrations, although the signal is very small relative to organics. The amount of OrgN in the gas-phase increases with increased NO addition as expected. The majority of the OrgN compounds have 5 or fewer carbons and no one component dominates the OrgN. Notable signals include for example $C_4H_7NO_5$ and $C_5H_9NO_{5\text{-}6}$. The two largest signals detected by the FIGAERO-CIMS in the particle-phase at both low and high input NO are $C_5H_{12}O_6$ and $C_5H_{12}O_5$. Other compounds with the isoprene $C_5$ backbone but one degree of unsaturation also represent some of the largest signals at low-$NO_x$, such as $C_5H_{10}O_{4\text{-}7}$. As in the gas-phase, no one component dominates the particle-phase OrgN, although one of the strongest signals is $C_5H_{11}NO_7$, the nitrate analogue to $C_5H_{12}O_6$, formed from the same $C_5H_{11}O_6$ peroxy radical (see Figure 2.1). Compounds with the formula $C_5H_{7,9,11}NO_{4\text{-}8}$ are all observed in the particle-phase, consistent with field observations from an isoprene-emitting forest during the Southern Oxidant and Aerosol Study campaign [*Lee et al.*, 2016]. For compounds that are detected in the particle-phase, their $T_{max}$ and thermogram shape are also listed in Table 1 and lends information on the nature of these compounds which will be discussed in further detail later on.

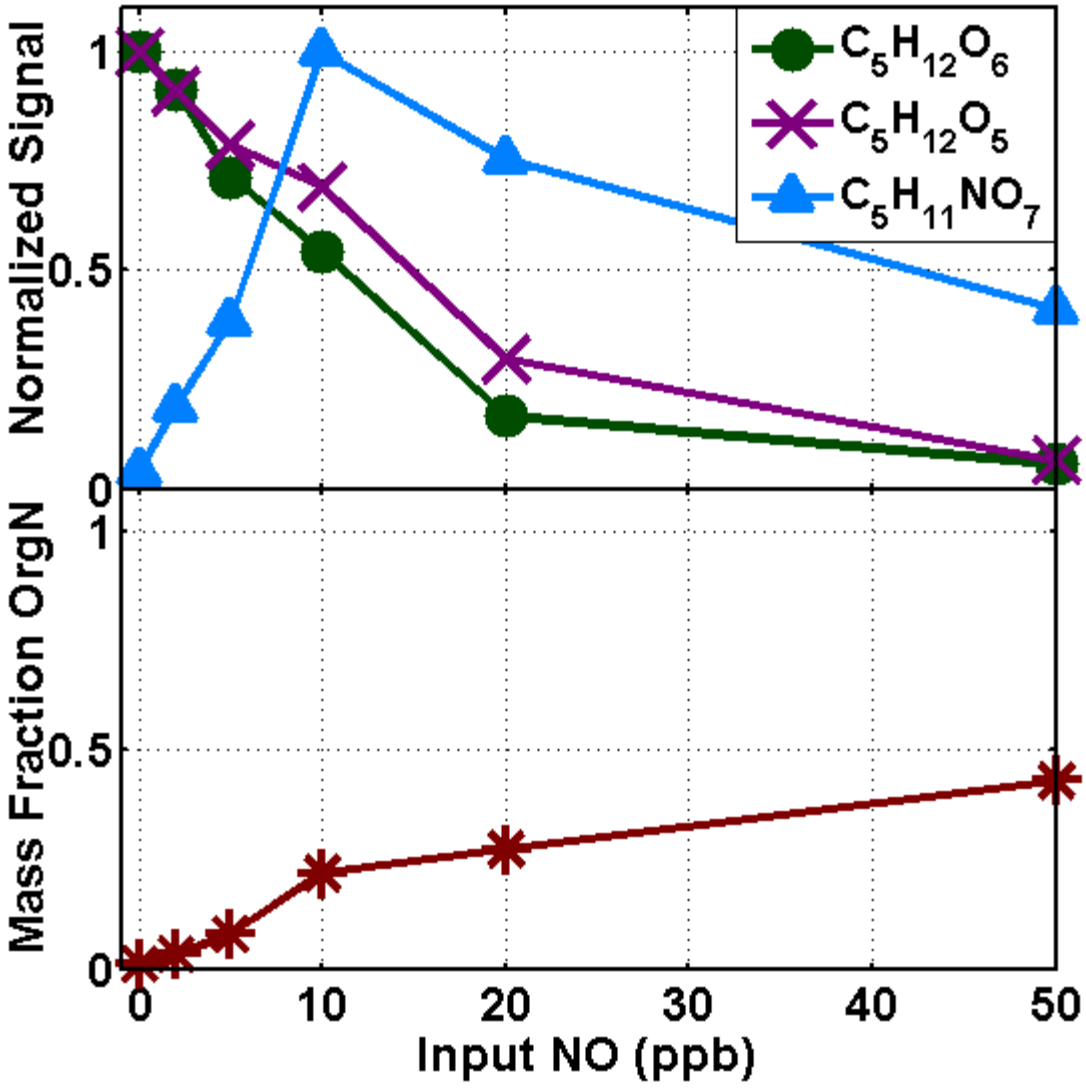


Figure 2.4 Top: Normalized signals of $C_5H_{12}O_6$ and $C_5H_{11}NO_7$, believed to originate in the gas phase from the same $C_5H_{11}O_6$ peroxy radical, as well as $C_5H_{12}O_5$, as a function of input NO. Signal is normalized to maximum signal for each compound to show the relative behaviors. Bottom: The mass fraction of organic nitrates as a function of NO. Mass fraction refers to the mass concentration of FIGAERO-CIMS measured OrgN relative to the total mass concentration of organics (non-nitrogen containing + OrgN) measured by the FIGAERO-CIMS.

The general effect of $NO_x$ on the SOA in this system has been described previously [*Liu et al.*, 2016]. Here we highlight the effect of input NO concentrations on individual compounds by focusing on three of the most prominent particle-phase species (Figure 2.4, top). As the input NO concentration increases, $C_5H_{12}O_6$ and $C_5H_{12}O_5$ decrease nonlinearly. $C_5H_{11}NO_7$, presumably produced from the ISOPOOH + OH $C_5H_{11}O_6$ peroxy radical increases initially with increasing NO addition. Above moderate NO input (>10 ppb), $C_5H_{11}NO_7$, a nitrate, begins to decrease with further increases in NO addition, likely a result of ISOPOOH also decreasing as the $C_5H_9O_3$ peroxy radical reacts more with NO as opposed to $HO_2$. This behavior supports previous observations of low isoprene SOA yields at high $NO_x$ [*Kroll et al.*, 2005; 2006; *Lane et al.*, 2008; *Xu et al.*, 2014; *Zhang et al.*, 2011], though we note a monotonic $NO_x$ dependence of SOA yield in our experiments [*Liu et al.*, 2016]. The bottom panel of Figure 2.4 depicts the mass fraction of OrgN as a function of input NO. The mass fraction of OrgN increases rapidly between 0 and 10 ppb NO input and more modestly above that. At the highest input NO concentration, OrgN make up ~40% of the organic aerosol mass detected by the FIGAERO-CIMS. This estimate carries uncertainty due to the inability to calibrate to every OrgN compound, as well as a lack of a single dominant OrgN. At the highest input NO, the AMS measurements also indicate that OrgN make up ~40% of the SOA mass, assuming a molecular weight of the typical OrgN of 148 g/mol based on the measured FIGAERO-CIMS particle-phase OrgN distribution, which is consistent with our findings. Though considerable uncertainties exist with respect to quantification of OrgN using both the AMS and the FIGAERO-CIMS, the agreement between these independent measurements suggests the calibration factors applied to the FIGAERO-CIMS OrgN signals are reasonable. We draw two main conclusions from this analysis: (1) the complementary increase in OrgN and decrease in non-nitrates likely accounts for the stable SOA mass yields at lower input

NO concentrations as reported previously [*Liu et al.*, 2016], with the highest input NO concentrations resulting in a decrease in both OrgN and non-nitrates, corresponding to the sharp decrease in SOA mass yield at the highest input NO concentration (50 ppb), and (2) while there is no one OrgN that is most prominent in the gas or particle phase, the total OrgN can comprise up to 40% of the SOA mass at high input NO concentrations (50 ppb).

### 2.3.2 *Time Evolution of Low $NO_x$ Isoprene SOA Compositions*

To examine how isoprene photochemical SOA evolves over time, a time-dependent experiment was conducted (Figure 2.5) similar to a previous batch mode study [*Kroll et al.*, 2006]. In this "batch mode" experiment, isoprene, $H_2O_2$, and solid ammonium sulfate seed were injected into the chamber, and then the lights were turned on. The chemistry of the closed system was allowed to evolve in time without further input of reactants. Each pie chart represents a FIGAERO-CIMS particle-phase desorption measurement over the course of the experiment. The data are converted to mass concentration as discussed previously [*Lee et al.*, 2016; *Liu et al.*, 2016], the overall size of each pie chart is proportional to the amount of AMS measured OA (5.6, 10.8, 10.6, 10.4 μg $m^{-3}$ from left to right, corrected for particle wall loss), and the time is the mid-point of the particle collection period (which lasted 25 minutes) relative to the initiation of the chemistry. The desorption just prior to the isoprene injection is used as the baseline, and the corresponding mass spectra are subtracted from the succeeding desorptions. Unlike the work of Kroll et al. [2006] who saw SOA volume maximize after ~3-4 hours of oxidation followed by a large decrease in total volume attributed to photochemical processing, the measurements presented here did not follow the reaction progress long after the maximum OA concentration was achieved (<1 hour) and thus we did not observe a significant decrease in mass.

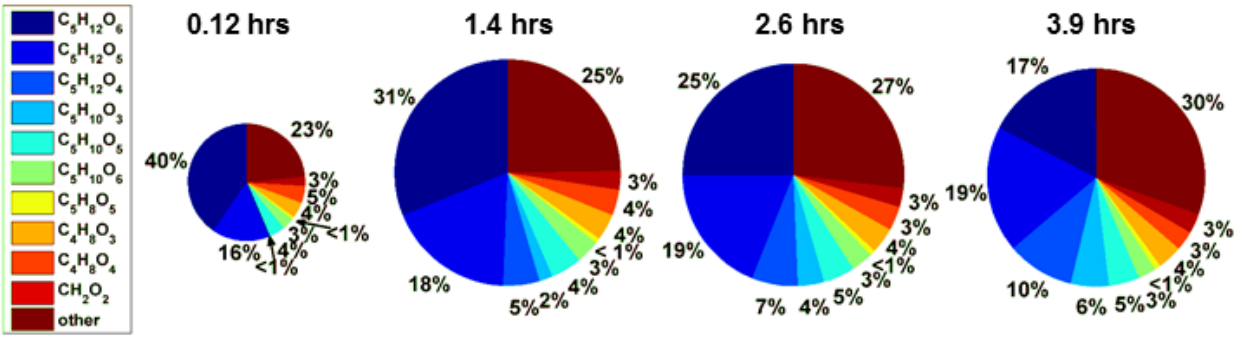


Figure 2.5 Time evolution of particle-phase concentrations in a batch mode isoprene photochemical oxidation experiment at low-$NO_x$. Time increases from left to right and the size of the pies is proportional to the amount of OA present which is: 5.6, 10.8, 10.6, 10.4 µg $m^{-3}$ from left to right.

The absolute and relative concentration of $C_5H_{12}O_6$ in the particle-phase decreases from 40% of the particle-phase SOA to 17% over the four hours of oxidation. The absolute mass of SOA also changes, primarily increasing, during the experiment, reaching a peak of 11.6 µg $m^{-3}$ at t = 4.3 hours. This suggests $C_5H_{12}O_6$ is transforming either within the particle-phase via hydrolysis or other mechanisms, or in the gas-phase, with efficient gas-particle equilibration, due to reaction with OH or photolysis [*Baasandorj et al.*, 2010; *Hsieh et al.*, 2014; *Roehl et al.*, 2007], with a particle-phase half-life of ~4 hours. Gas-phase oxidation seems unlikely given that typically greater than 95% of the $C_5H_{12}O_6$ is found in the particle-phase (Figure 2.6) when OA >2 µg $m^{-3}$. While many of the detected compounds are present at constant mass fractions throughout time, $C_5H_{12}O_5$, $C_5H_{12}O_4$, and $C_5H_{10}O_3$ increase. $C_5H_{12}O_5$ has been observed previously in the gas-phase from ISOPOOH oxidation [*Krechmer et al.*, 2015], and was also shown to be a large fraction of the particle-phase from isoprene oxidation [*Liu et al.*, 2016], but its production

mechanism is uncertain. Krechmer et al. [2015] suggest it could be formed from the oxidation of an impurity in the ISOPOOH, although the experiments presented here use isoprene as the BVOC precursor, ruling out this explanation. In these experiments, $C_5H_{12}O_5$ is observed within the first hour of isoprene oxidation and increases to ~18% of the OA mass within 1.5 hours, becoming relatively stable thereafter. Two possible sources of this compound are the reaction of the ISOPOOH-derived peroxy radical ($C_5H_{11}O_6$) with $RO_2$, or a dihydroxy alkene undergoing reaction with OH and $O_2$ to form a dihydroxy peroxy radical, followed by reaction with $HO_2$. It is also possible that $C_5H_{12}O_5$ could be formed in the condensed phase from hydrolysis reactions. Further work is required to understand the source of this compound.

The other two compounds that increase with time, $C_5H_{12}O_4$ and $C_5H_{10}O_3$, likely isomers of 2-methyl tetrols and alkene triols respectively, are traditional markers of IEPOX derived SOA [*Claeys et al.*, 2004; *Ding et al.*, 2008; *Edney et al.*, 2005; *Kourtchev et al.*, 2005; *Surratt et al.*, 2010; *Xia and Hopke*, 2006]. This result is unexpected given that using effloresced (solid) ammonium sulfate seed at a RH below the deliquescence point (RH ~50%) together with an SOA coating should strongly suppress the known acid catalyzed IEPOX multiphase chemistry [*Gaston et al.*, 2014; *Lin et al.*, 2013a; *Lin et al.*, 2014; *Lin et al.*, 2012; *Lin et al.*, 2013b; *Liu et al.*, 2014; *Nguyen et al.*, 2014; *Paulot et al.*, 2009b; *Surratt et al.*, 2010; *Surratt et al.*, 2006]. We tested the uptake of an authentic IEPOX standard onto dry, crystalline ammonium sulfate seed under conditions similar to these, though during continuous-flow mode, and found no measurable uptake and SOA formation [*Liu et al.*, 2016]. However, it is consistent with previous work that found both of these tracers in the SOA when isoprene was oxidized in the absence of deliquesced acidic seed [*Edney et al.*, 2005; *Kleindienst et al.*, 2009]. $C_5H_{12}O_4$ and $C_5H_{10}O_3$ are

less than 1% of the SOA for the first 2 hours and then gradually increase to 10% and 6% of the SOA, respectively, after 4 hours. Interestingly, the FIGAERO-CIMS thermograms for these tracers have broad maxima at much higher $T_{max}$ than would be consistent with their elemental composition. Lopez-Hilfiker et al. [2016] noted two modes in the thermogram of $C_5H_{12}O_4$, one with a $T_{max}$ as expected based on its structure and another with a higher $T_{max}$ indicating an effectively lower volatility component thermally decomposing. These two tracers are also observed in the $NO_x$ addition experiments performed in continuous-flow mode, though at lower concentrations. In these experiments there was not enough NO to completely suppress ISOPOOH formation and therefore IEPOX formation from ISOPOOH + OH. Moreover, IEPOX can also form, albeit at lower yields, from OH reactions with the first-generation isoprene hydroxy nitrate [*Jacobs et al.*, 2014; *L Lee et al.*, 2014; *St Clair et al.*, 2016]. However, the formation of IEPOX SOA tracers is more puzzling given the very low reactive uptake of IEPOX expected on solid inorganic seed coated with isoprene SOA [Gaston et al., 2014; Riedel et al., 2015]. Perhaps nitric acid catalyzed IEPOX multiphase chemistry is contributing to the formation of these tracers at high $NO_x$. That said, observation of these tracers, also in the absence of $NO_x$ addition, indicates that this explanation not sufficient.

The chemical mechanism leading to the measurement of these tracers in the particle phase is unknown, but given that the experimental conditions strongly suppressed the traditional acid catalyzed aqueous IEPOX chemistry, perhaps these tracers are not solely derived from aqueous IEPOX chemistry but isoprene photochemical oxidation more generally. In conclusion, $C_5H_{12}O_6$ condenses rapidly and initially makes up a majority of the SOA mass, but over time its contribution decreases as other compounds such as $C_5H_{12}O_5$, $C_5H_{12}O_4$, and $C_5H_{10}O_3$ increase.

Our data suggest these compounds may be formed in the particle phase from heterogeneous reactions and/or during the thermal desorption analysis, but more work is required to determine their sources.

### 2.3.3 *Gas-particle Partitioning: Saturation Vapor Concentrations and Oligomeric Content*

The volatility of the products generated from the non-IEPOX $C_5H_{12}O_6$ pathway [*Krechmer et al.*, 2015; *Liu et al.*, 2016; *Riva et al.*, 2016] will be a crucial aspect of its contribution to SOA formation and the lifetime of the resulting SOA against dilution, gas-phase oxidation, and depositional losses. The capability of the FIGAERO-CIMS to measure the concentration of individual species in both the gas- and particle-phase allows for a direct measurement of the particle-phase fraction ($F_p$), which is the particle-phase concentration relative to the gas- and particle-phase concentrations per volume of air. The $F_p$ can also be calculated from an assumption of equilibrium absorptive partitioning theory first described by Pankow [1994] using equation 2.1 as first reported by Donahue et al. [2006], where C* is the saturation vapor concentration (μg $m^{-3}$) of the pure substance and $C_{OA}$ is the concentration of organic aerosol (μg $m^{-3}$).

$$F_p = \left(1 + \frac{c^*}{C_{OA}}\right)^{-1} \quad \text{(Eq. 2.1)}$$

Equation 2.1 neglects the activity coefficient and molecular weight differences for simplicity, though any C* derived from a comparison to equation 2.1 would implicitly include these factors. Calibration standards do not exist for a vast majority of compounds in SOA and therefore the C* are largely unknown, mitigating somewhat the impact of such simplifications. Group-contribution methods exist to estimate C*, where each functional group represents a discrete,

empirically determined contribution to the equilibrium vapor pressure of a compound [*Capouet and Muller*, 2006; *Compernolle et al.*, 2011; *Nannoolal et al.*, 2008; *Pankow and Asher*, 2008]. These approaches carry substantial uncertainty for atmospheric SOA systems, in large part due to the lack of enough standards to develop a robust parameterization. In addition, these approaches do not directly address the potential of functional group interactions, such as intramolecular hydrogen bonding, which when not included can lead to C* estimates that are significantly biased low [*Kurten et al.*, 2016].

Measured $F_p$ were determined using the FIGAERO-CIMS for a subset of major particle-phase components from 2015 (Figure 2.6). A short (1-2 m) laminar flow Teflon inlet line with a short residence time (<1 s) was coupled to the chamber for the detection of gases by the FIGAERO-CIMS. The largest source of error in the measured $F_p$, beyond thermal decomposition during desorption, is diffusion-controlled vapor losses in the inlet which were corrected for by assuming a diffusivity of 0.05-0.1 $cm^2\ s^{-1}$, although the variability is not discernable on the log scale. Inlet losses are 25-44% for the range of diffusivities, a small effect on the comparison of measured and predicted $F_p$ as we show below.

$F_p$ were predicted using equation 2.1 with $C_{OA}$ measured by the AMS and C* calculated via the EVAPORATION group-contribution method [*Compernolle et al.*, 2011], which generally gave similar estimates as the Capouet and Muller approach [2006]. The Nannoolal method [2008] was also explored, but it gave C* estimates that varied by several orders of magnitude for structurally similar compounds, as well as estimates that were unexpectedly low based on FIGAERO-CIMS measurements and what one would expect based on molecular structure, consistent with previous

findings [*Kurten et al.*, 2016]. The SIMPOL method of Pankow and Asher [2008] was also applied to select compounds and is discussed below. A major limitation of this analysis is that we do not know the structure of the molecules detected, only the elemental composition, and so we make assumptions based on the most likely functional groups expected from the chemical conditions of the chamber and from the elemental composition (e.g., degrees of unsaturation, oxygen to carbon ratio). In many cases these assumptions have little impact on our conclusions as the inferred errors are far larger than expected from possible isomers.

If the SOA formed according to equilibrium partitioning theory as first described by Pankow [1994], the $F_p$ measured by the FIGAERO-CIMS and the C* calculated using group-contribution methods should be in agreement over a range of organic aerosol mass concentrations. Figure 2.6 indicates two immediate challenges to testing partitioning theory. First, a large number of mostly small carbon number compounds have a much higher measured $F_p$ relative to the predicted $F_p$ based on their group-contribution determined C*. The C* estimates would have to be in error by five or more orders of magnitude, which is likely not the case as there are many measurements of vapor pressures for similar compounds. Furthermore, the thermograms of these compounds appear broad, not Gaussian as expected for individual non-interacting compounds [*Lopez-Hilfiker et al.*, 2014], and do not peak until ~85 °C or higher, see Table 1, which is also inconsistent with the calibrated composition-enthalpy of sublimation relationship scaled for the FIGAERO used here [*Lopez-Hilfiker et al.*, 2014]. We attribute this behavior to thermal decomposition of lower volatility components during the desorption process giving rise to smaller molecular weight, more volatile components as in previous studies of IEPOX SOA tracers in the southeast U.S. [*Lopez-Hilfiker et al.*, 2016], α-pinene derived chamber SOA

[*Lopez-Hilfiker et al.*, 2015], and biomass burning organic aerosol in the northwest U.S. [*Gaston et al.*, 2016]. That is, the disagreement between measured and predicted $F_p$ for these compounds is not necessarily a failure of equilibrium partitioning theory, nor evidence that equilibrium had not been achieved, but rather that the compounds desorbing were actually part of another larger molecular weight oligomerization product, the C* and gas-phase concentrations of which are unknown.

The second challenge to testing gas-particle partitioning is illustrated in the $F_p$ for two representative compounds, $C_5H_{12}O_6$ and $C_5H_{10}O_6$ (Figure 2.6, bottom panels). That there is reasonable agreement between measured and predicted $F_p$ (Figure 2.6, bottom right, circles) for $C_5H_{10}O_6$ suggests that equilibrium partitioning is potentially achieved in the chamber. However, the disagreement for $C_5H_{12}O_6$ (Figure 2.6, bottom left, circles) cannot be explained solely by thermal decomposition of lower volatility material for two reasons: the thermogram shape is nearly Gaussian and therefore behaves like a single component, and the predicted $F_p$ is much larger than measured (opposite to the above situation). This behavior implies inaccurate C* derived from the group-contribution methods as opposed to thermal decomposition.

The EVAPORATION group-contribution method [*Compernolle et al.*, 2011] used in Figure 2.6 and that of Capouet and Muller [2006] both produce a C* of 0.03 μg $m^{-3}$ for $C_5H_{12}O_6$ when assuming it is a dihydroxy dihydroperoxide, while the SIMPOL method predicts 2 μg $m^{-3}$ [*Pankow and Asher*, 2008]. For $C_5H_{10}O_6$, assumed to be a hydroxy dihydroperoxy aldehyde, EVAPORATION [*Compernolle et al.*, 2011] predicts 4 μg $m^{-3}$, the Capouet and Muller [2006] method predicts 2 μg $m^{-3}$, and SIMPOL [*Pankow and Asher*, 2008] suggests 20 μg $m^{-3}$. That the

$C_5H_{12}O_6$ values vary by 2 orders of magnitude while the $C_5H_{10}O_6$ values vary by a factor of 10 suggests the need for better experimental constraints. Using the measured $T_{max}$ from the FIGAERO-CIMS thermograms, the C* of $C_5H_{12}O_6$ and $C_5H_{10}O_6$ were determined to be 0.7 and 7 μg $m^{-3}$, respectively. These values were then used to re-calculate the predicted $F_p$ using equation 2.1. The original group-contribution calculated $F_p$ is shown alongside the adjusted points in the bottom panels of Figure 2.6 as navy crosses. The root mean square error of both $C_5H_{12}O_6$ and $C_5H_{10}O_6$ is minimized when comparing the measurements with the adjusted $F_p$, indicating that the calibrated FIGAERO-CIMS temperature axis can more accurately determine the C*.

There are a number of possible reasons why measured and predicted $F_p$ do not agree, with one being that our methods to estimate C* are flawed. This potential source of error can be addressed directly with the FIGAERO-CIMS thermograms, independently of the measured $F_p$, thereby allowing for a more robust assessment of whether *(i)* the assumption of gas-particle equilibrium is reasonable, *(ii)* there are possible biases in the measured $F_p$ due to thermal decomposition, or *(iii)* the C* estimation methods are valid. The above analysis demonstrates that all possibilities arise in this data set.

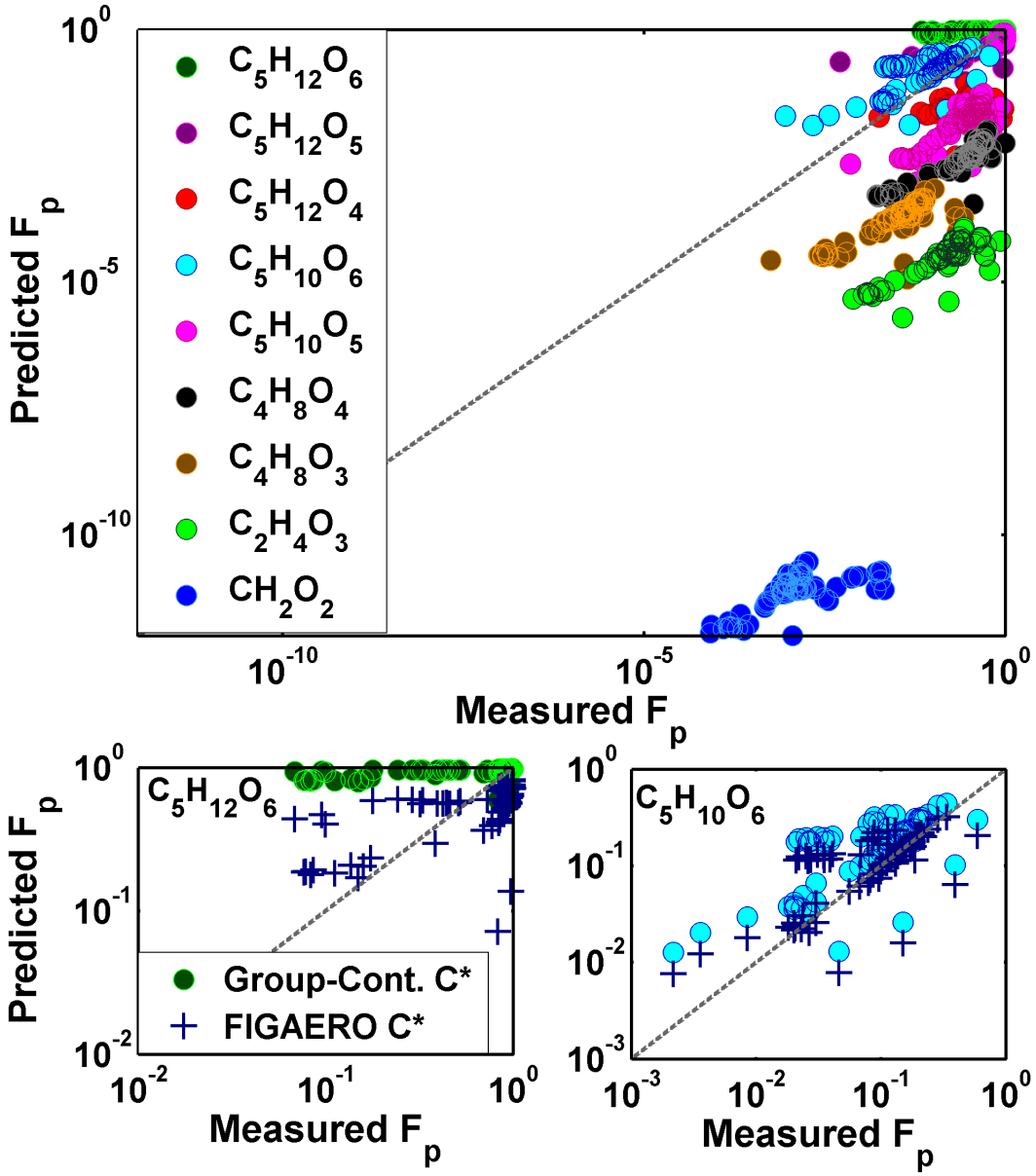


Figure 2.6 Top: Predicted versus measured fraction in the particle-phase ($F_p$). Predicted $F_p$ is obtained from equation 2.1 where C*s were calculated with the EVAPORATION group-contribution method [*Compernolle et al.*, 2011] labeled as "Group-Cont. C*" in the bottom panels. Measured $F_p$ is the direct measurement from the FIGAERO. Bottom: The $F_p$ can also be predicted based on the calibrated FIGAERO temperature axis as discussed in the methods and is shown as the predicted $F_p$ here. Agreement can be reached for two representative compounds where the $F_p$ is over and correctly predicted (left, right respectively).

In the case of $C_5H_{12}O_6$ the FIGAERO-CIMS determined C* is much closer to the SIMPOL estimation, and significantly higher than that estimated by the other group-contribution methods. We suspect the large differences between measured and group-contribution method estimates of C* in this case are due to the lack of vapor pressure data on compounds with hydroperoxide groups, specifically multifunctional hydroperoxides: there is only data on four hydroperoxide containing compounds on which these methods are based [*Capouet and Muller*, 2006; *Compernolle et al.*, 2011]. It can be argued that -OH and –OOH groups will lower the C* relative to the precursor by a comparable amount, with the possibility that a -OOH group could lower it slightly more due to the additional oxygen. For example, the C* of 2-methyl-1,2,3,4-butanol ($C_5H_{12}O_4$) was calculated to be 9 to 34 μg $m^{-3}$, depending on the method used [*Capouet and Muller*, 2006; *Compernolle et al.*, 2011], roughly 250-1000 times greater than the C* estimates for $C_5H_{12}O_6$. That is, a molecule with the same number of distinct –OH containing functional groups is predicted to have a very different C* because the vapor pressure lowering of –OOH groups assumed by these group-contribution methods is larger than that for an -OH group. Our observations suggest this assumption is incorrect, at least to the extent employed in these methods, and is supported by previous work that found group-contribution methods predicted significantly lower C* than two computational models, the conductor-like screening model for real solvents (COSMO-RS) [*Kurten et al.*, 2016] and the generator for explicit chemistry and kinetics of organics in the atmosphere (GECKO-A) [*Valorso et al.*, 2011], did for compounds with multiple functionalities. Conversely, we assume $C_5H_{10}O_6$ is a hydroxy dihydroperoxy aldehyde, also with two –OOH groups, but the group contribution methods accurately predicted a C* consistent with that inferred from the FIGAERO-CIMS $T_{max}$. This agreement may be a coincidence or indicative of the fact that multifunctional compounds with

slightly different functional groups can have significantly different intramolecular interactions, leading to significantly different saturation vapor concentrations [*Compernolle et al.*, 2011].

Figure 2.6 leads to two main conclusions. The first is that testing equilibrium partitioning theory is a challenge without a direct constraint on the C* like the FIGAERO-CIMS desorption $T_{max}$ due to possibly large systematic errors in the C* predicted from group-contribution methods. Moreover, thermal decomposition of higher molecular weight compounds, such as oligomers, into smaller molecular weight compounds generates uncertainty in the measured $F_p$ in that the FIGAERO-CIMS $T_{max}$ derived C* does not correspond in such cases to the observed molecule. This result leads to our second conclusion: a surprisingly large fraction of the iSOA is resistant to evaporation, indicating it will have a longer lifetime against dilution [*Kroll et al.*, 2006]. Approximately 30-45% of the SOA mass detected by the FIGAERO-CIMS desorbs at temperatures greater than 80 °C, much of that above 100 °C, which corresponds to effective enthalpies of sublimation >150 kJ $mol^{-1}$ in our FIGAERO-CIMS assuming no diffusion limitations to evaporation from the particles that exist at these temperatures (for example, due to highly viscous phases). We note that Kroll et al. [2006] also found evidence for a significant mass fraction of large molecular weight compounds when applying the AMS to low-$NO_x$, non-IEPOX iSOA. We conclude that oligomerization products are the cause of this more refractory SOA component, but, we cannot determine from the thermograms alone whether the oligomerization process is reversible at ambient temperatures on longer timescales than the ~1 hour desorptions. That the SOA yield from isoprene is significantly higher for similar organic mass loadings than that reported from ISOPOOH only, suggests an important role for the broader distribution of oxidation products formed in addition to those from ISOPOOH. One possible

reason is that these mostly semi volatile products can contribute to lower volatility products via oligomerization chemistry [*Jathar et al.*, 2016; *Sato et al.*, 2011; *Tsai et al.*, 2015].

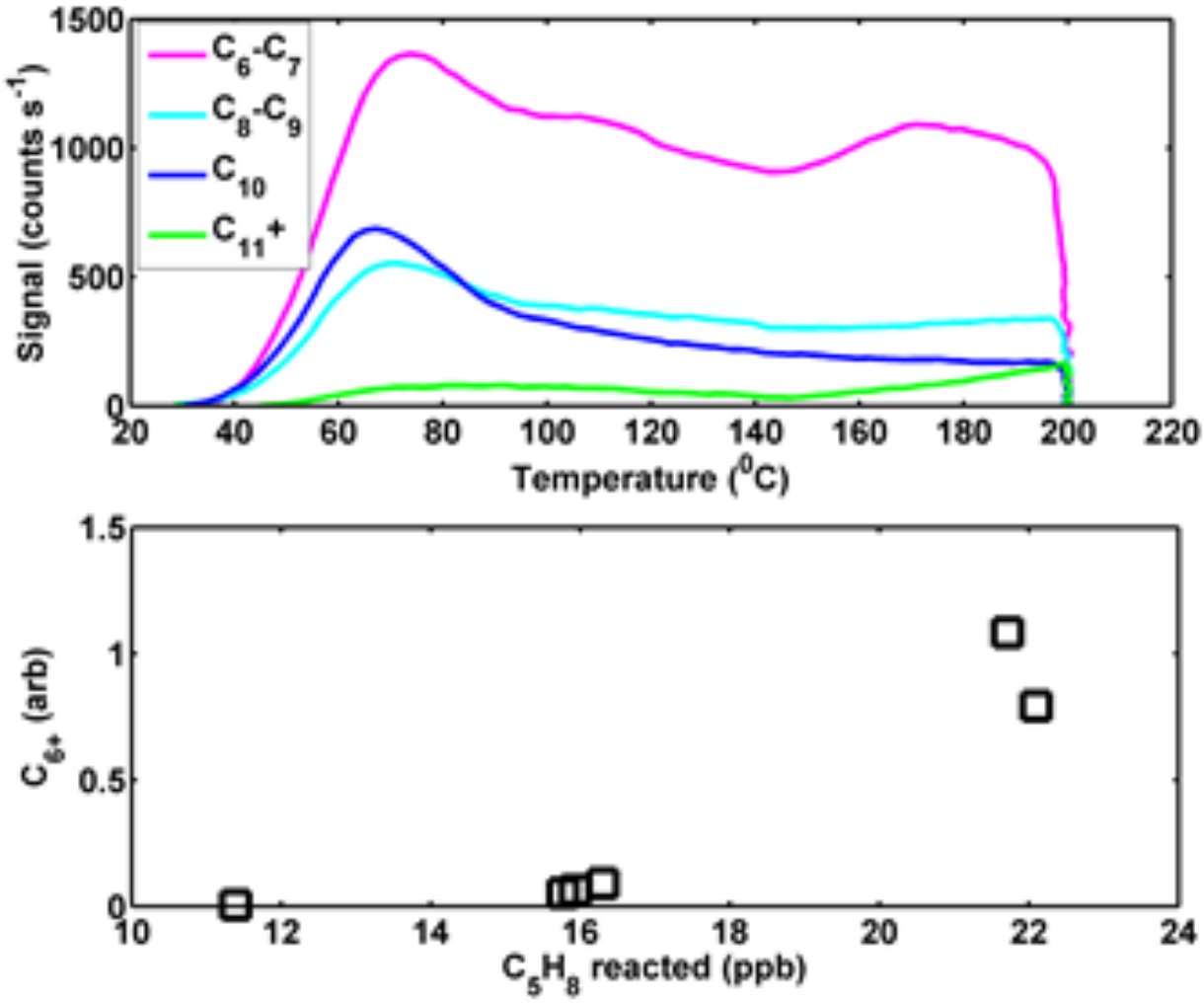


Figure 2.7 Top: Sum of the thermogram signal for compounds with formula $C_xH_yO_zI$-, where x is varied across each thermogram and represents compounds with 6 or more carbons. Bottom: The sum off the mass concentration of all compounds with 6 or more carbons relative to the mass concentration of organic aerosol as a function of isoprene reacted.

The sum of thermogram signals across all ions with formula $C_xH_yO_zN_{0-1}I$- is presented in Figure 6, with the value of x specified for each thermogram. We measured non-negligible signal for

compounds with 6 or more carbons, consistent with the possibility of oligomerization products. Such compounds account for ~5-15% of detected mass. Compounds with 6-7 carbons make up a majority of the signal for compounds with greater than 5 carbons, though we also detected significant signal in $C_8$-$C_{10}$ compounds, themselves making up 3-8% of detected mass. We measure a monoterpene impurity at 0.3% of the isoprene concentration in our gas cylinder which could result in ~0.05-0.1 μg $m^{-3}$ of monoterpene SOA, i.e. 0.3-2.8% of the SOA mass, significantly lower than the sum of all compounds with 6 or more carbons as well as the sum of just $C_{8\text{-}10}$ compounds. Furthermore, the ratio of $C_{6\text{-}7}$ to $C_{10}$ compounds is 5-10 times higher than we detect in monoterpene + OH experiments performed in the same chamber with the same FIGAERO-CIMS. We also note that a previous study similar to the ones presented here detected $C_{10}H_{20\text{-}22}O_{6\text{-}9}$ compounds, as well as a fragment ion in the AMS at *m/z* 91 corresponding to $C_7H_7$+ which was tentatively attributed to thermal decomposition of dimers and oligomers on the vaporizer, among other possibilities [*Riva et al.*, 2016]. The mass concentration of these compounds with 6 or more carbons was found to increase with isoprene reacted (Figure 2.7, bottom). At the highest isoprene reacted, these contribute on order 25% to the total OA mass detected.

### 2.3.4 *Role of $NO_x$ in iSOA Volatility*

Previous studies using thermal denuders and either an AMS or a tandem differential mobility measurement of particle size distributions have found that iSOA formed in the presence of $NO_x$ is less volatile relative to that formed in $HO_2$-dominant regimes [*Kleindienst et al.*, 2009; *Xu et al.*, 2014]. We compare the iSOA volatility under different regimes by looking at the sum thermograms for compounds with formulae $C_xH_yO_zN_{0\text{-}1}I^-$. These sum thermograms are plotted as

a function of temperature for both low- and high-$NO_x$ conditions in Figure 2.8, bottom left and right, respectively. Since $C_5H_{12}O_6$ is a large portion of the SOA mass concentration in these experiments (e.g. Figure 2.5), it is shown separately in dark green with the remainder of the summed signal shown in light green. $C_5H_{12}O_6$ is clearly a large contribution to the sum signal in both the low- and high-$NO_x$ cases, although more so in the low $NO_x$ regime, with the remaining thermogram signal primarily located in the lower volatility (higher temperature) "tail" of the desorption. We have also showed in the bottom left low $NO_x$ figure a sum of the thermograms for all compounds with 6 or more carbons, i.e. the sum of all thermograms in Figure 2.7. We note that the sum of these compounds makes up ~6% of the total signal. At high $NO_x$, there are two clear modes in the thermogram remaining after removing the $C_5H_{12}O_6$ contribution (light green), one mode at roughly the same $T_{max}$, and therefore volatility, of $C_5H_{12}O_6$, and the other mode at a higher $T_{max}$, ~110 °C, suggesting a larger fraction of detected iSOA mass at high $NO_x$ is resistant to evaporation compared to the low $NO_x$ case. We also note that the $T_{max}$ of individual compounds shifts to higher values with the addition of $NO_x$ except for the highest mass compounds (see Table 1). Although the thermograms for many of these compounds do not have a distinct Gaussian shape, making determination of the $T_{max}$ uncertain or undefined, the shift to higher $T_{max}$ for the same compounds could indicate not just lower volatility products in the form of oligomers, but also potentially a change in the overall particle viscosity causing the iSOA to be more resistant to evaporation with the addition of $NO_x$.

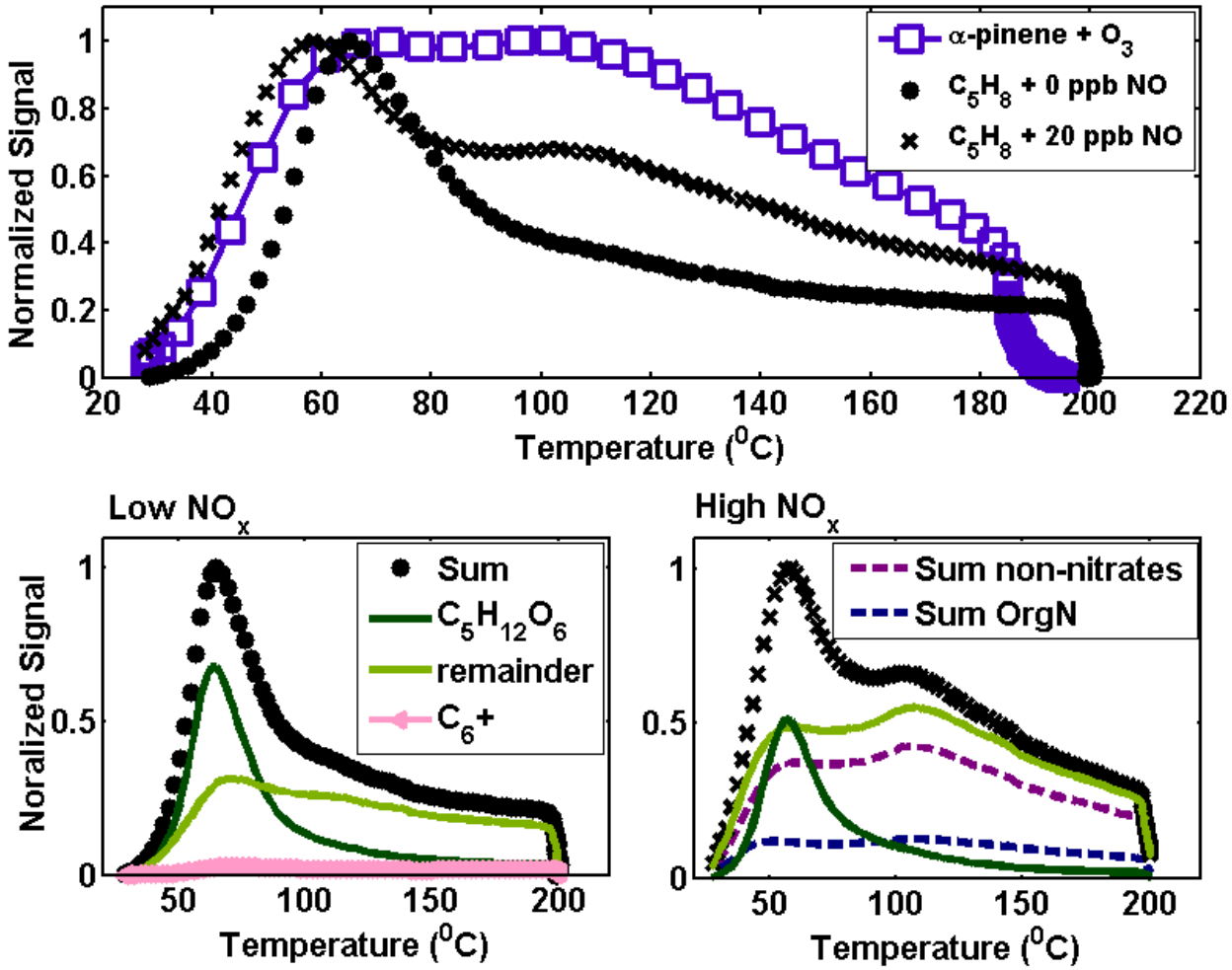


Figure 2.8 Top: Sum thermograms of α-pinene + $O_3$ compared to isoprene ($C_5H_8$) photooxidation with and without $NO_x$. The α-pinene sum thermogram has been reported previously (Lopez-Hilfiker et al. [2015], Figure 5). Bottom: The sum thermograms at low (left) and high (right) input NO. The thermogram of $C_5H_{12}O_6$, the largest signal in both cases, is separated out (dark green) and the sum of the remaining signal minus $C_5H_{12}O_6$ is displayed as the remaining signal (light green). At Low NO input, the sum of compounds with 6 or more carbons is specified (pink triangle/line), while at high NO input the sum of OrgN and the sum of non-nitrate organics are plotted (dashed lines, independent of solid lines) to show the relative thermogram features.

A sum thermogram of α-pinene ozonolysis that has been previously reported [*Lopez-Hilfiker et al.*, 2015] is displayed alongside those of the low- and high-$NO_x$ experiments (Figure 2.8, top) for comparison. The α-pinene SOA has a bimodal sum thermogram, similar to that of the high-$NO_x$ iSOA with the second lower volatility modes in the same temperature range. The higher volatility mode of the α-pinene SOA corresponds in temperature space to that of the higher volatility mode of the low-$NO_x$ iSOA. The multiple modes of the α-pinene sum thermogram have the same relative maxima in signal space, unlike the isoprene sum thermograms. α-Pinene ozonlysis apparently generates a larger fraction of lower volatility SOA relative to isoprene photochemical oxidation, although isoprene photochemical SOA has components in the same volatility ranges of α-pinene ozonlysis SOA, and the relative size of the various modes and location in temperature space is dependent on the amount of $NO_x$.

The contribution of the effectively lower volatility components inferred from thermograms in Figure 2.8 is likely underestimated in both the low- and high- $NO_x$ cases because the thermograms are presented as ion signal, not mass concentration. If we converted into mass concentration units prior to calculating the summed thermogram, the contribution of $C_5H_{12}O_6$ would be significantly less than implied in Conclusions

## 2.4 Results & Discussion

We have explored the composition and volatility of isoprene SOA at low and high $NO_x$ concentrations utilizing effloresced ammonium sulfate seed to prevent IEPOX uptake and thus suppress IEPOX multiphase chemistry. We measured compositions of products reported in previous works of similar experiments [*Krechmer et al.*, 2015; *Liu et al.*, 2016; *Riva et al.*,

2016], in particular $C_5H_{12}O_6$ and related highly oxidized compounds. We note that these compounds have also been observed in the atmosphere in isoprene rich regions [*Riva et al.*, 2016]. We examined the saturation vapor concentrations of several of the most dominant particle-phase signals and tested the accuracy of various group-contribution methods to determine the C*. Of the three group-contribution methods assessed, the SIMPOL approach [*Pankow and Asher*, 2008] gave the closest estimates of C* compared to those determined from the thermograms. The vapor pressure lowering effect of –OOH groups, assumed to be abundantly present in this system, appears to be greatly overestimated in two commonly used methods [*Capouet and Muller*, 2006; *Compernolle et al.*, 2011]. Through these analyses we found that a significant fraction of SOA components we measure are likely thermal decomposition fragments, characterized by broad thermograms and higher than expected $T_{max}$.

That such a large fraction (30-45%) of the non-IEPOX iSOA is of low volatility implies the lifetime of non-IEPOX iSOA is longer than would previously be expected. Together with the thermal decomposition fragments, we also observe compounds with 6 or greater carbons, supporting an important role for oligomerization chemistry. These findings suggest that experiments which assess the SOA formation potential of isoprene or one of its oxidation products alone likely underestimate the overall potential due to the participation of a broad suite of products in oligomerization chemistry. Further work on the role of oligomerization chemistry in this system is needed to verify that the higher iSOA yield observed by Liu et al. [2016] from isoprene is indeed caused by semi volatile products participating in oligomerization reactions. Furthermore, we have shown here that the addition of NO has a strong effect on the amount of $C_5H_{12}O_6$ produced, and while the overall volatility of the OA decreases with $NO_x$, the total

amount of OA also decreases [*Liu et al.*, 2016], indicating that in polluted regions the amount of SOA formed from this pathway will be diminished, but the SOA will be longer lived against dilution. In conclusion, due to the high yield of IEPOX from ISOPOOH + OH it has been assumed to be the most important pathway for the formation of iSOA, however, its relatively high volatility (~$2 \times 10^4$ μg $m^{-3}$ [*Compernolle et al.*, 2011]) and the fact that it requires such specific conditions to form SOA efficiently implies that the formation of SOA from the non-IEPOX pathway discussed herein can also play an important role in many environments regardless of sulfate aerosol concentrations.

References

Baasandorj, M., D. K. Papanastasiou, R. K. Talukdar, A. S. Hasson, and J. B. Burkholder (2010), (CH3)(3)COOH (tert-butyl hydroperoxide): OH reaction rate coefficients between 206 and 375 K and the OH photolysis quantum yield at 248 nm, *Phys. Chem. Chem. Phys.*, *12*(38), 12101-12111.

Capouet, M., and J. F. Muller (2006), A group contribution method for estimating the vapour pressures of alpha-pinene oxidation products, *Atmospheric Chemistry and Physics*, *6*, 1455-1467.

Claeys, M., et al. (2004), Formation of secondary organic aerosols through photooxidation of isoprene, *Science*, *303*(5661), 1173-1176.

Compernolle, S., K. Ceulemans, and J. F. Muller (2011), EVAPORATION: a new vapour pressure estimation method for organic molecules including non-additivity and intramolecular interactions, *Atmos. Chem. Phys.*, *11*(18), 9431-9450.

Ding, X., M. Zheng, L. P. Yu, X. L. Zhang, R. J. Weber, B. Yan, A. G. Russell, E. S. Edgerton, and X. M. Wang (2008), Spatial and seasonal trends in biogenic secondary organic aerosol tracers and water-soluble organic carbon in the southeastern United States, *Environmental science & technology*, *42*(14), 5171-5176.

Docherty, K. S., W. Wu, Y. B. Lim, and P. J. Ziemann (2005), Contributions of organic peroxides to secondary aerosol formed from reactions of monoterpenes with $O_3$, *Environmental science & technology*, *39*(11), 4049-4059.

Dommen, J., A. Metzger, J. Duplissy, M. Kalberer, M. R. Alfarra, A. Gascho, E. Weingartner, A. S. H. Prevot, B. Verheggen, and U. Baltensperger (2006), Laboratory observation of oligomers in the aerosol from isoprene/NOx photooxidation, *Geophys. Res. Lett.*, *33*(13).

Donahue, N. M., A. L. Robinson, C. O. Stanier, and S. N. Pandis (2006), Coupled partitioning, dilution, and chemical aging of semivolatile organics, *Environmental science & technology*, *40*(8), 2635-2643.

Donahue, N. M., E. R. Trump, J. R. Pierce, and I. Riipinen (2011), Theoretical constraints on pure vapor-pressure driven condensation of organics to ultrafine particles, *Geophys. Res. Lett.*, *38*(16), L16801.

Edney, E. O., T. E. Kleindienst, M. Jaoui, M. Lewandowski, J. H. Offenberg, W. Wang, and M. Claeys (2005), Formation of 2-methyl tetrols and 2-methylglyceric acid in secondary organic aerosol from laboratory irradiated isoprene/NO(X)/SO(2)/air mixtures and their detection in ambient PM(2.5) samples collected in the eastern United States, *Atmospheric Environment*, *39*(29), 5281-5289.

Gaston, C. J., T. P. Riedel, Z. F. Zhang, A. Gold, J. D. Surratt, and J. A. Thornton (2014), Reactive uptake of an isoprene-derived epoxydiol to submicron aerosol particles, *Environ. Sci. Technol.*, *48*(19), 11178-11186.

Gaston, C. J., F. D. Lopez-Hilfiker, L. E. Whybrew, O. Hadley, F. McNair, H. Gao, D. A. Jaffe, and J. A. Thornton (2016), Online molecular characterization of fine particulate matter in Port Angeles, WA: Evidence for a major impact from residential wood smoke, *Atmospheric Environment*, *138*, 99-107.

Guenther, A. B., X. Jiang, C. L. Heald, T. Sakulyanontvittaya, T. Duhl, L. K. Emmons, and X. Wang (2012), The model of emissions of gases and aerosols from nature version 2.1 (MEGAN2.1): an extended and updated framework for modeling biogenic emissions, *Geosci. Model Dev.*, *5*(6), 1471-1492.

Hsieh, S., R. Vushe, Y. M. T. Tun, and J. L. Vallejo (2014), Trends in organic hydroperoxide photodissociation and absorption cross sections between 266 and 377 nm, *Chem. Phys. Lett.*, *591*, 99-102.

Jacobs, M. I., W. J. Burke, and M. J. Elrod (2014), Kinetics of the reactions of isoprene-derived hydroxynitrates: gas phase epoxide formation and solution phase hydrolysis, *Atmos. Chem. Phys.*, *14*(17), 8933-8946.

Jang, M. S., N. M. Czoschke, S. Lee, and R. M. Kamens (2002), Heterogeneous atmospheric aerosol production by acid-catalyzed particle-phase reactions, *Science*, *298*(5594), 814-817.

Jathar, S. H., C. D. Cappa, A. S. Wexler, J. H. Seinfeld, and M. J. Kleeman (2016), Simulating secondary organic aerosol in a regional air quality model using the statistical oxidation model - Part 1: Assessing the influence of constrained multi-generational ageing, *Atmospheric Chemistry and Physics*, *16*(4), 2309-2322.

Jimenez, J. L., et al. (2009), Evolution of organic aerosols in the atmosphere, *Science*, *326*(5959), 1525-1529.

King, S. M., T. Rosenoern, J. E. Shilling, Q. Chen, Z. Wang, G. Biskos, K. A. McKinney, U. Poschl, and S. T. Martin (2010), Cloud droplet activation of mixed organic-sulfate particles produced by the photooxidation of isoprene, *Atmospheric Chemistry and Physics*, *10*(8), 3953-3964.

Kirkby, J., et al. (2016), Ion-induced nucleation of pure biogenic particles, *Nature*, *533*(7604), 521-526.

Kleindienst, T. E., M. Lewandowski, J. H. Offenberg, M. Jaoui, and E. O. Edney (2009), The formation of secondary organic aerosol from the isoprene plus OH reaction in the absence of NOx, *Atmospheric Chemistry and Physics*, *9*(17), 6541-6558.

Kourtchev, I., T. Ruuskanen, W. Maenhaut, M. Kulmala, and M. Claeys (2005), Observation of 2-methyltetrols and related photo-oxidation products of isoprene in boreal forest aerosols from Hyytiala, Finland, *Atmospheric Chemistry and Physics*, *5*, 2761-2770.

Krechmer, J. E., et al. (2015), Formation of low volatility organic compounds and Secondary Organic Aerosol from isoprene hydroxyhydroperoxide low-NO oxidation, *Environ. Sci. Technol.*, *49*(17), 10330-10339.

Kroll, J. H., N. L. Ng, S. M. Murphy, R. C. Flagan, and J. H. Seinfeld (2005), Secondary organic aerosol formation from isoprene photooxidation under high-NOx conditions, *Geophys. Res. Lett.*, *32*(18).

Kroll, J. H., N. L. Ng, S. M. Murphy, R. C. Flagan, and J. H. Seinfeld (2006), Secondary organic aerosol formation from isoprene photooxidation, *Environ. Sci. Technol.*, *40*(6), 1869-1877.

Kurten, T., K. Tiusanen, P. Roldin, M. Rissanen, J. N. Luy, M. Boy, M. Ehn, and N. Donahue (2016), alpha-Pinene autoxidation products may not have extremely low saturation vapor pressures despite high O:C ratios, *J. Phys. Chem. A*, *120*(16), 2569-2582.

Lane, T. E., N. M. Donahue, and S. N. Pandis (2008), Effect of NO(x) on secondary organic aerosol concentrations, *Environmental science & technology*, *42*(16), 6022-6027.

Lee, B. H., F. D. Lopez-Hilfiker, C. Mohr, T. Kurten, D. R. Worsnop, and J. A. Thornton (2014), An iodide-adduct high-resolution time-of-flight chemical-ionization mass spectrometer: application to atmospheric inorganic and organic compounds, *Environ. Sci. Technol.*, *48*(11), 6309-6317.

Lee, B. H., et al. (2016), Highly functionalized organic nitrates in the southeast United States: Contribution to secondary organic aerosol and reactive nitrogen budgets, *Proceedings of the National Academy of Sciences*, *113*, 1516-1521.

Lee, L., A. P. Teng, P. O. Wennberg, J. D. Crounse, and R. C. Cohen (2014), On rates and mechanisms of OH and O3 reactions with isoprene-derived hydroxy nitrates, *J. Phys. Chem. A*, *118*(9), 1622-1637.

Lin, Y. H., E. M. Knipping, E. S. Edgerton, S. L. Shaw, and J. D. Surratt (2013a), Investigating the influences of SO2 and NH3 levels on isoprene-derived secondary organic aerosol formation using conditional sampling approaches, *Atmos. Chem. Phys.*, *13*(16), 8457-8470.

Lin, Y. H., H. Budisulistiorini, K. Chu, R. A. Siejack, H. F. Zhang, M. Riva, Z. F. Zhang, A. Gold, K. E. Kautzman, and J. D. Surratt (2014), Light-absorbing oligomer formation in secondary organic aerosol from reactive uptake of isoprene epoxydiols, *Environ. Sci. Technol.*, *48*(20), 12012-12021.

Lin, Y. H., et al. (2012), Isoprene epoxydiols as precursors to secondary organic aerosol formation: Acid-catalyzed reactive uptake studies with authentic compounds, *Environ. Sci. Technol.*, *46*(1), 250-258.

Lin, Y. H., et al. (2013b), Epoxide as a precursor to secondary organic aerosol formation from isoprene photooxidation in the presence of nitrogen oxides, *Proc. Natl. Acad. Sci. U. S. A.*, *110*(17), 6718-6723.

Liu, J. M., et al. (2016), Efficient isoprene secondary organic aerosol formation from a non-IEPOX pathway, *Environ. Sci. Technol.*, *50*(18), 9872-9880.

Liu, S., J. E. Shilling, C. Song, N. Hiranuma, R. A. Zaveri, and L. M. Russell (2012), Hydrolysis of organonitrate functional groups in aerosol particles, *Aerosol Sci. Technol.*, *46*(12), 1359-1369.

Liu, Y., M. Kuwata, B. F. Strick, F. M. Geiger, R. J. Thomson, K. A. McKinney, and S. T. Martin (2014), Uptake of epoxydiol isomers accounts for half of the particle-phase material produced from isoprene photooxidation via the HO pathway, *Environ. Sci. Technol.*, *49*, 250-258.

Lopez-Hilfiker, F. D., et al. (2014), A novel method for online analysis of gas and particle composition: description and evaluation of a Filter Inlet for Gases and AEROsols (FIGAERO), *Atmos. Meas. Tech.*, *7*(4), 983-1001.

Lopez-Hilfiker, F. D., et al. (2015), Phase partitioning and volatility of secondary organic aerosol components formed from alpha-pinene ozonolysis and OH oxidation: the importance of accretion products and other low volatility compounds, *Atmos, Chem. Phys.*, *15*(14), 7765-7776.

Lopez-Hilfiker, F. D., et al. (2016), Molecular composition and volatility of organic aerosol in the southeastern US: Implications for IEPOX derived SOA, *Environ. Sci. Technol.*, *50*(5), 2200-2209.

Nannoolal, Y., J. Rarey, and D. Ramjugernath (2008), Estimation of pure component properties - Part 3. Estimation of the vapor pressure of non-electrolyte organic compounds via group contributions and group interactions, *Fluid Phase Equilibria*, *269*(1-2), 117-133.

Nguyen, T. B., M. M. Coggon, K. H. Bates, X. Zhang, R. H. Schwantes, K. A. Schilling, C. L. Loza, R. C. Flagan, P. O. Wennberg, and J. H. Seinfeld (2014), Organic aerosol formation from the reactive uptake of isoprene epoxydiols (IEPOX) onto non-acidified inorganic seeds, *Atmospheric Chemistry and Physics*, *14*(7), 3497-3510.

Pandis, S. N., S. E. Paulson, J. H. Seinfeld, and R. C. Flagan (1991), Aerosol formation in the photooxidation of isoprene and beta-pinene, *Atmospheric Environment Part a-General Topics*, *25*(5-6), 997-1008.

Pankow, J. F. (1994), AN ABSORPTION-MODEL OF GAS-PARTICLE PARTITIONING OF ORGANIC-COMPOUNDS IN THE ATMOSPHERE, *Atmospheric Environment*, *28*(2), 185-188.

Pankow, J. F., and W. E. Asher (2008), SIMPOL.1: a simple group contribution method for predicting vapor pressures and enthalpies of vaporization of multifunctional organic compounds, *Atmospheric Chemistry and Physics*, *8*(10), 2773-2796.

Paulot, F., J. D. Crounse, H. G. Kjaergaard, J. H. Kroll, J. H. Seinfeld, and P. O. Wennberg (2009a), Isoprene photooxidation: new insights into the production of acids and organic nitrates, *Atmos. Chem. Phys.*, *9*(4), 1479-1501.

Paulot, F., J. D. Crounse, H. G. Kjaergaard, A. Kurten, J. M. St Clair, J. H. Seinfeld, and P. O. Wennberg (2009b), Unexpected epoxide formation in the gas-phase photooxidation of isoprene, *Science*, *325*(5941), 730-733.

Poschl, U. (2005), Atmospheric aerosols: Composition, transformation, climate and health effects, *Angew. Chem.-Int. Edit.*, *44*(46), 7520-7540.

Riedel, T. P., Y. H. Lin, H. Budisulistiorini, C. J. Gaston, J. A. Thornton, Z. F. Zhang, W. Vizuete, A. Gold, and J. D. Surrattt (2015), Heterogeneous reactions of isoprene-derived epoxides: reaction probabilities and molar secondary organic aerosol yield estimates, *Environ. Sci. Technol. Lett.*, *2*(2), 38-42.

Riipinen, I., et al. (2011), Organic condensation: a vital link connecting aerosol formation to cloud condensation nuclei (CCN) concentrations, *Atmospheric Chemistry and Physics*, *11*(8), 3865-3878.

Riva, M., et al. (2016), Chemical characterization of secondary organic aerosol from oxidation of isoprene hydroxyhydroperoxides, *Environ. Sci. Technol.*, *50*(18), 9889-9899.

Roehl, C. M., Z. Marka, J. L. Fry, and P. O. Wennberg (2007), Near-UV photolysis cross sections of CH3OOH and HOCH2OOH determined via action spectroscopy, *Atmospheric Chemistry and Physics*, *7*, 713-720.

Sato, K., S. Nakao, C. H. Clark, L. Qi, and D. R. Cocker (2011), Secondary organic aerosol formation from the photooxidation of isoprene, 1,3-butadiene, and 2,3-dimethyl-1,3-butadiene under high NOx conditions, *Atmospheric Chemistry and Physics*, *11*(14), 7301-7317.

Shilling, J. E., Q. Chen, S. M. King, T. Rosenoern, J. H. Kroll, D. R. Worsnop, K. A. McKinney, and S. T. Martin (2008), Particle mass yield in secondary organic aerosol formed by the dark ozonolysis of alpha-pinene, *Atmos. Chem. Phys.*, *8*(7), 2073-2088.

Shilling, J. E., et al. (2013), Enhanced SOA formation from mixed anthropogenic and biogenic emissions during the CARES campaign, *Atmospheric Chemistry and Physics*, *13*(4), 2091-2113.

St Clair, J. M., J. C. Rivera-Rios, J. D. Crounse, H. C. Knap, K. H. Bates, A. P. Teng, S. Jørgensen, H. G. Kjaergaard, F. N. Keutsch, and P. O. Wennberg (2016), Kinetics and products of the reaction of the first-generation isoprene hydroxy hydroperoxide (ISOPOOH) with OH, *J. Phys. Chem. A*, *120*(9), 1441-1451.

Surratt, J. D., M. Lewandowski, J. H. Offenberg, M. Jaoui, T. E. Kleindienst, E. O. Edney, and J. H. Seinfeld (2007), Effect of acidity on secondary organic aerosol formation from isoprene, *Environ. Sci. Technol.*, *41*(15), 5363-5369.

Surratt, J. D., A. W. H. Chan, N. C. Eddingsaas, M. N. Chan, C. L. Loza, A. J. Kwan, S. P. Hersey, R. C. Flagan, P. O. Wennberg, and J. H. Seinfeld (2010), Reactive intermediates revealed in secondary organic aerosol formation from isoprene, *Proc. Natl. Acad. Sci. U. S. A.*, *107*(15), 6640-6645.

Surratt, J. D., et al. (2006), Chemical composition of secondary organic aerosol formed from the photooxidation of isoprene, *J. Phys. Chem. A*, *110*(31), 9665-9690.

Tsai, I. C., J. P. Chen, C. S. C. Lung, N. Li, W. N. Chen, T. M. Fu, C. C. Chang, and G. D. Hwang (2015), Sources and formation pathways of organic aerosol in a subtropical metropolis during summer, *Atmospheric Environment*, *117*, 51-60.

Valorso, R., B. Aumont, M. Camredon, T. Raventos-Duran, C. Mouchel-Vallon, N. L. Ng, J. H. Seinfeld, J. Lee-Taylor, and S. Madronich (2011), Explicit modelling of SOA formation from alpha-pinene photooxidation: sensitivity to vapour pressure estimation, *Atmospheric Chemistry and Physics*, *11*(14), 6895-6910.

Weber, R. J., et al. (2007), A study of secondary organic aerosol formation in the anthropogenic-influenced southeastern United States, *J. Geophys. Res.-Atmos.*, *112*(D13), D13302.

Xia, X., and P. K. Hopke (2006), Seasonal variation of 2-methyltetrols in ambient air samples, *Environmental science & technology*, *40*(22), 6934-6937.

Xu, L., M. S. Kollman, C. Song, J. E. Shilling, and N. L. Ng (2014), Effects of NOx on the volatility of secondary organic aerosol from isoprene photooxidation, *Environmental science & technology*, *48*(4), 2253-2262.

Xu, L., et al. (2015), Effects of anthropogenic emissions on aerosol formation from isoprene and monoterpenes in the southeastern United States, *Proc. Natl. Acad. Sci. U. S. A.*, *112*(1), 37-42.

Zhang, H., J. D. Surratt, Y. H. Lin, J. Bapat, and R. M. Kamens (2011), Effect of relative humidity on SOA formation from isoprene/NO photooxidation: enhancement of 2-methylglyceric acid and its corresponding oligoesters under dry conditions, *Atmospheric Chemistry and Physics*, *11*(13), 6411-6424.

Zhang, Q., et al. (2007), Ubiquity and dominance of oxygenated species in organic aerosols in anthropogenically-influenced Northern Hemisphere midlatitudes, *Geophys. Res. Lett.*, *34*(13), L13801.

Zhang, X., C. D. Cappa, S. H. Jathar, R. C. McVay, J. J. Ensberg, M. J. Kleeman, and J. H. Seinfeld (2014), Influence of vapor wall loss in laboratory chambers on yields of secondary organic aerosol, *Proc. Natl. Acad. Sci. U. S. A.*, *111*(16), 5802-5807.

# Chapter 3. ISOMERIZATION OF SECOND GENERATION ISOPRENE PEROXY RADICALS: EPOXIDE FORMATION AND IMPLICATIONS FOR SECONDARY ORGANIC AEROSOL YIELDS[2]

Abstract

We report chamber measurements of secondary organic aerosol (SOA) formation from isoprene photochemical oxidation, where radical concentrations were systematically varied and the molecular composition of semi to low volatility gases and SOA were measured online. Using a detailed chemical kinetics box model, we find that to explain the behavior of low volatility products and SOA mass yields relative to input $H_2O_2$ concentrations, the second generation dihydroxy hydroperoxy peroxy radical ($C_5H_{11}O_6$•) must undergo an intra-molecular H-shift with a net forward rate constant of order 0.1 $s^{-1}$ or higher. This finding is consistent with quantum chemical calculations which suggest a net forward rate constant of 0.3-0.9 $s^{-1}$. Furthermore, these calculations suggest the dominant product of this isomerization is a dihydroxy hydroperoxy epoxide ($C_5H_{10}O_5$) which is expected to have a saturation vapor pressure ~2 orders of magnitude higher, as determined by group-contribution calculations, than the dihydroxy dihydroperoxide, $ISOP(OOH)_2$ ($C_5H_{12}O_6$), a major product of the peroxy radical reacting with $HO_2$. These results provide strong constraints on the likely volatility distribution of isoprene oxidation products under atmospheric conditions and thus on the importance of non-reactive gas-particle partitioning of isoprene oxidation products as an SOA source.

---

[2] Reprinted with permission from: D'Ambro, E. L., Moller, K. H., Lopez-Hilfiker, F. D., Schobesberger, S., Liu, J. M., Shilling, J. E., Lee, B., Kjaergaard, H. G., and Thornton, J. A.: Isomerization of Second-Generation Isoprene Peroxy Radicals: Epoxide Formation and Implications for Secondary Organic Aerosol Yields, Environmental science & technology, 51, 4978-4987, doi: 10.1021/acs.est.7b00460, 2017.

## 3.1 INTRODUCTION

Atmospheric submicron aerosol particles impact climate, human health, and visibility [*Poschl*, 2005]. A large portion of submicron aerosol mass (~20-90%) is secondary organic aerosol (SOA) [*Jimenez et al.*, 2009; *Zhang et al.*, 2007], which arises from chemical processes in the atmosphere that convert volatile organic compounds (VOC) into condensed-phase organic material. A significant fraction of SOA is thought to be formed from biogenic rather than anthropogenic VOC [*Schichtel et al.*, 2008; *Weber et al.*, 2007]. The annual emissions of isoprene ($C_5H_8$), primarily from deciduous vegetation, represent nearly half the total of all non-methane hydrocarbons [*Guenther et al.*, 2012]. Thus, isoprene has the potential to generate large quantities of SOA, even if its overall conversion is inefficient.

The formation of SOA from the free radical photochemical oxidation of biogenic VOC (BVOC) is governed in part by the mass concentration (c) weighted volatility distribution of the resulting products. For example, BVOC oxidation products having equilibrium saturation vapor concentrations (c*) lower than ~100 μg $m^{-3}$ can be expected to partition into an existing organic condensed-phase and thus contribute to SOA, as typical organic aerosol mass concentrations ($c_{OA}$) are in the range of 1-10 μg $m^{-3}$ [*Donahue et al.*, 2011; *Pankow*, 1994]. The volatility distribution of BVOC oxidation products is governed by the ratio of the BVOC that undergoes functionalization relative to fragmentation during atmospheric oxidation. Oxidation of BVOC is frequently initiated by the formation of a carbon-centered radical primarily due to reaction with a hydroxyl radical (OH). In this initial stage, atmospheric oxygen ($O_2$) can add to the carbon-

centered radical to form an organic peroxy radical ($RO_2$). $RO_2$ can then undergo bimolecular reactions with typically $HO_2$, NO, or $RO_2$. All of these bimolecular reactions can produce more functionalized products, while the latter two can also form alkoxy radicals (RO) which can undergo H-shift isomerization [*Atkinson and Lloyd*, 1984] or fragment into smaller, more volatile products. Thus, the volatility distribution is largely determined by the fate of $RO_2$ intermediates.

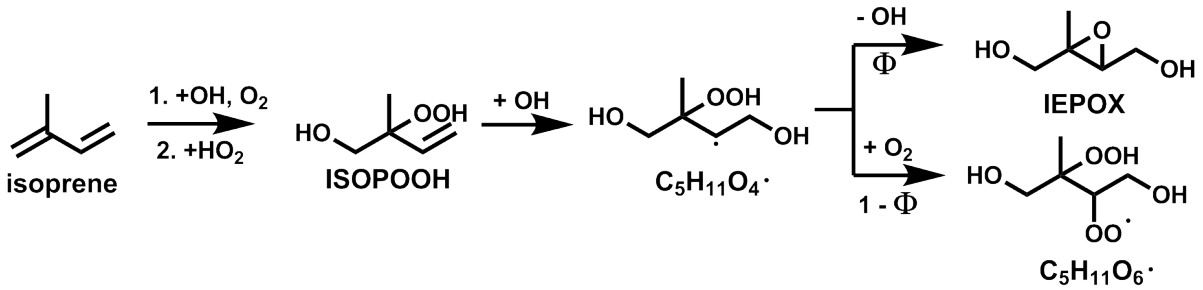


Figure 3.1 Isoprene photochemical oxidation mechanism for one isomer of ISOPOOH under low-$NO_x$ conditions. ϕ and 1-ϕ represent the branching ratio between IEPOX and the peroxy radical, respectively.

In the specific case of isoprene (Figure 3.1), OH addition to a double bond followed by $O_2$ addition yields a hydroxy $RO_2$. Some isomers of the first-generation $RO_2$ can undergo unimolecular isomerization (not shown), with a forward rate constant of order 0.01 - 1 $s^{-1}$ [*Crounse et al.*, 2011; *Peeters et al.*, 2009; *Peeters et al.*, 2014], followed by $HO_2$ loss to produce a hydroperoxyenal (HPALD) [*Crounse et al.*, 2011; *Peeters et al.*, 2009], or dihydroperoxy-carbonyl peroxy radicals (di-HPCARP) [*Peeters et al.*, 2014]. The net isomerization rate constant weighted by the isomer distribution was calculated to be ~0.001 $s^{-1}$ [*Crounse et al.*, 2011; *Peeters et al.*, 2014]. The first generation $RO_2$ can undergo bimolecular reactions with $HO_2$ to form a hydroxy hydroperoxide (ISOPOOH), NO to form an alkyl nitrate [*Paulot et al.*, 2009a], or NO or $RO_2$ to form an alkoxy radical. The latter tends to decompose by carbon-carbon

bond scission to form products such as formaldehyde, methacrolein, or methyl vinyl ketone [*Atkinson et al.*, 1989; *Miyoshi et al.*, 1994; *Paulson and Seinfeld*, 1992; *Tuazon and Atkinson*, 1990]. These first generation closed-shell products are rather volatile, and though they may undergo multiphase reactions, their contribution to SOA by direct partitioning is likely small. Given that a large fraction of isoprene reacts to form ISOPOOH under low $NO_x$ conditions, possibly up to or greater than 70% [*Paulot et al.*, 2009b], and that it likely has the lowest c* of the first generation products, its oxidation products are the subject of continued focus.

ISOPOOH reacts rapidly via OH addition to the remaining double bond producing a carbon-centered radical often α to the hydroperoxide moiety (Figure 3.1). This alkyl radical has been shown to form an epoxide bridge with the hydroperoxide group. Consecutive loss of OH from that hydroperoxide group forms an epoxydiol (IEPOX) [*Paulot et al.*, 2009b] ~70-80% of the time [*St Clair et al.*, 2016] (Figure 3.1). A significant fraction of isoprene-derived SOA is now understood to originate from acid catalyzed aqueous phase chemistry of IEPOX [*Gaston et al.*, 2014; *Lin et al.*, 2013a; *Lin et al.*, 2014; *Lin et al.*, 2012; *Lin et al.*, 2013b; *Liu et al.*, 2014; *Paulot et al.*, 2009b; *Surratt et al.*, 2010; *Surratt et al.*, 2006], although SOA also forms from isoprene oxidation in the absence of an acidic aqueous phase [*Krechmer et al.*, 2015; *Kroll et al.*, 2006; *Liu et al.*, 2016; *Riva et al.*, 2016]. Recent gas- [*Krechmer et al.*, 2015] and particle-phase [*D'Ambro et al.*, 2017; *Liu et al.*, 2016; *Riva et al.*, 2016] composition measurements of low-$NO_x$ OH oxidation of both isoprene and ISOPOOH reveal highly oxygenated second generation products. A major particle-phase component has the composition $C_5H_{12}O_6$ [*D'Ambro et al.*, 2017; *Liu et al.*, 2016; *Riva et al.*, 2016], likely a dihydroxy dihydroperoxide, which we refer to as $ISOP(OOH)_2$ (see Figure 3.2, top reaction, for structure). This product is believed to form

from $O_2$ addition to the carbon-centered radical from ISOPOOH + OH to yield a second generation $RO_2$ in competition with IEPOX formation (Figure 3.1), followed by reaction of the $RO_2$ with $HO_2$ (Figure 3.2, top reaction). A fraction of ISOPOOH + OH is also expected to react via H-abstraction from an alkyl group or the –OOH group, although these channels are relatively small contributions to net ISOPOOH reactivity [*St Clair et al.*, 2016].

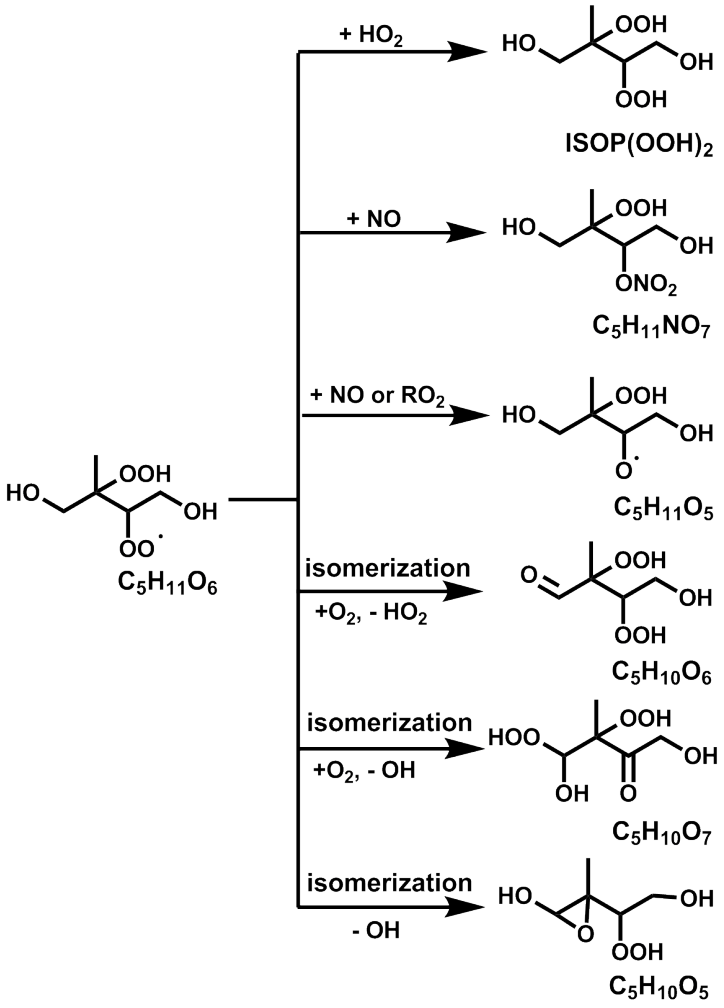


Figure 3.2 Proposed mechanism for one isomer of $C_5H_{11}O_6$, the peroxy radical formed from ISOPOOH + OH in Figure 3.1. The formation of the three isomerization products is shown in detail in Figure 3.5.

In previous work, we showed that steady-state $ISOP(OOH)_2$ and SOA mass yields increase together as the OH and $HO_2$ source [*Liu et al.*, 2016], $H_2O_2$, is increased relative to isoprene. Reasons for this behavior have yet to be determined. Mechanistic explanations for prominent products from this system other than $ISOP(OOH)_2$, such as $C_5H_{12}O_5$ and $C_5H_{10}O_{5\text{-}7}$, are also lacking. Herein, we compare an expanded set of chamber experiments with novel predictions from a detailed multiphase chemical model, and quantum chemical calculations of $RO_2$ radical fates, to improve our understanding of the isoprene oxidation mechanism and thus the formation of isoprene SOA from non-IEPOX oxidation products. Specifically, we test different hypotheses for the fate of the $C_5H_{11}O_6$• peroxy radical so that we can understand the dependence of non-IEPOX isoprene SOA formation on chamber oxidation conditions. We conclude with a discussion of the atmospheric implications of our findings.

## 3.2 METHODS

### 3.2.1 *Laboratory Experiments*

A suite of online instruments were employed to monitor the gas- and particle-phase chemical composition. Ozone (Thermo Environmental Instruments model 49C), $NO/NO_2/NO_x$ (Thermo Environmental Instruments model 42C), and isoprene (Ionicon proton-transfer-reaction mass spectrometer (PTR-MS)) concentrations were measured in the chamber outflow. Bulk submicron organic and inorganic particle-phase composition and mass loading were measured with an Aerodyne high-resolution time-of-flight aerosol mass spectrometer (HRToF-AMS). A high-resolution time-of-flight chemical ionization mass spectrometer (HRToF-CIMS) with iodide ionization was coupled to a Filter Inlet for Gases and AEROsols (FIGAERO) [*Lopez-Hilfiker et al.*, 2014]. The HRToF-CIMS FIGAERO coupling has been described in detail previously in the

configuration used in these experiments [*D'Ambro et al.*, 2017; *B H Lee et al.*, 2014; *Liu et al.*, 2016]. Briefly, the FIGAERO is an inlet manifold that allows for sampling gas-phase composition at 1 Hz through an independent inlet while collecting aerosol particles on a Teflon filter through another inlet. Particle-phase composition is assessed at approximately hourly resolution by actuating the filter to be in front of the HRToF-CIMS entrance orifice and performing temperature-programmed thermal desorption of particles. Vaporized particle-phase compounds are then detected by the HRToF-CIMS.

Experiments presented here have been discussed previously [*D'Ambro et al.*, 2017], but the observed relationships of SOA yields to radical sources in these specific experiments have not been presented. In brief, experiments were performed in 2015 in the Pacific Northwest National Laboratory's 10.6 $m^3$ fluorinated ethylene polypropylene (FEP) environmental chamber, which has been described before [*D'Ambro et al.*, 2017; *Liu et al.*, 2012]. The chamber was controlled to a constant 50% relative humidity and operated in continuous-flow mode with a residence time of 5.2 hours where reactants are continuously delivered at a constant flow rate while products are continuously monitored with a suite of gas- and particle-phase instrumentation. OH and $HO_2$ radicals were generated from the photolysis of excess $H_2O_2$ (Sigma-Aldrich, 50% in water), with chamber concentrations ranging from <0.5 to 10 ppm. A constant flow of isoprene was delivered to the chamber to achieve 20 ppbv (Matheson, 20 ppm isoprene in nitrogen) at steady state in the absence of photochemistry. Monodisperse 50 nm diameter solid ammonium sulfate seed particles were added to facilitate SOA formation. More information on these experiments can be found in previous publications [*D'Ambro et al.*, 2017; *Liu et al.*, 2016] and the SI.

### 3.2.2 *Box Model Simulations*

The laboratory experiments presented here were simulated with a detailed chemical kinetics box model, the Framework for 0-D Atmospheric Modeling (F0AM) [*Wolfe et al.*, 2016]. F0AM is a zero-dimensional, i.e. single box model developed from the CAFE model [*Wolfe and Thornton*, 2011; *Wolfe et al.*, 2011a; *Wolfe et al.*, 2011b], which incorporates the latest version of the University of Leeds Master Chemical Mechanism (v3.3.1) for isoprene [*Jenkin et al.*, 2015], as well as customized updates including the newly observed ISOP(OOH)$_2$ pathway summarized in Figure 3.2. See SI Tables 1 and 2 for a complete list of chemical structures, reactions, rates, and yields added to the MCM isoprene mechanism. The mechanism development will be discussed in detail in the following sections.

We have also coupled F0AM to a custom dynamic gas-particle partitioning module to better simulate the competing pathways of vapor loss to chamber walls, partitioning to particles, and oxidation in the gas-phase that low- and semi-volatile products will undergo. Condensation and evaporation rate coefficients ($k_{\text{cond}}$ and $k_{\text{evap}}$, respectively) were calculated using the inverse timescales for gas-to-particle mass transfer and evaporation of a surface bound molecule given by equations 3.3 and 3.4, respectively.

$$k_{cond} = k_{mt} S_a \quad \text{(Eq. 3.2)}$$

$$k_{evap} = k_{mt} S_a \frac{c_i^*}{c_{OA}} \quad \text{(Eq. 3.3)}$$

$$k_{mt} = \left( \frac{r_p}{D_g} + \frac{r}{\alpha \omega} \right)^{-1} \quad \text{(Eq. 3.4)}$$

$S_a$ is the aerosol surface area per volume of air, $c_i^*$ is the saturation vapor concentration of compound $i$, $c_{OA}$ is the mass concentration of the absorbing organic aerosol, and $k_{mt}$ is the gas-phase diffusion limited gas-to-particle mass transfer coefficient given by equation 3.5. In equation 3.5, $r_p$ is the particle radius, ω is the mean molecular speed, $D_g$ is the gas-phase diffusion constant assumed to be 0.1 $cm^2\ s^{-1}$ based on Hilal et al. [2003] and references therein, and α is the mass accommodation coefficient assumed to be 0.1 based on findings by Saleh et al. [2013] for a BVOC SOA system. The $c_i^*$ were calculated using the EVAPORATION group-contribution method [*Compernolle et al.*, 2011] with adjustments for $ISOP(OOH)_2$ and other select compounds as described in D'Ambro et al. [2017]. Compounds with c* ≤ 100 μg $m^{-3}$ were allowed to participate in gas-particle partitioning reactions. A separate $k_{cond}$ and $k_{evap}$ was used for each compound tracked in the partitioning module due to the specificity of the c* and ω. Vapors undergoing gas-particle partitioning also undergo irreversible loss to the chamber walls described using a single pseudo first order rate coefficient for all compounds, discussed below. Particle wall-loss is also described with a single rate coefficient, $6\times10^{-5}\ s^{-1}$ [*Crump et al.*, 1983], as the steady-state size distribution is fairly monodisperse.

Emission rates of isoprene, $H_2O_2$, and seed particles, as well as chamber residence time with respect to dilution, are fixed to their observed values for a given set of chamber conditions (Table S3). Photolysis frequencies were estimated from known lamp spectral intensities and adjusted slightly to match the observed decay of isoprene (Fig. S1). The set of 2,090 gas-phase reactions involving 645 species, including dynamic condensation and evaporation of 101 of those species to an organic phase are then integrated until chemical steady-state is reached, i.e. production and loss of species were equal and thus concentrations were unchanging. The

observational data presented here has not been wall-loss corrected because we include particle and vapor wall-losses in the model. More information, including a link to the Matlab code, can be found in the SI.

Using the reactions shown in Figure 3.2 together with the extensive isoprene oxidation mechanism already in F0AM, we first explored the sensitivity of the predicted $ISOP(OOH)_2$ and SOA to three key mechanistic parameters *(i)* the yield of $C_5H_{11}O_6$• peroxy radical (from ISOPOOH + OH, Figure 3.1) relative to the yield of IEPOX, *(ii)* the possible isomerization rate of the $C_5H_{11}O_6$• peroxy radical (Figure 3.2), and *(iii)* the vapor wall-loss rate. In total, 36 model runs were performed, independently varying each of these parameters. The branching ratio between IEPOX and $C_5H_{11}O_6$• from the reaction of ISOPOOH + OH was varied between 70%, 76%, and 82% in line with the measurements of St. Clair et al. [2016] to address *(i)*. The isomerization rate constant, $k_{isom}$, of $C_5H_{11}O_6$• was varied between 0, 0.005, 0.3, and 0.8 $s^{-1}$ to address *(ii)*. While it has been shown that vapor wall-losses can be significant in chamber experiments [*Krechmer et al.*, 2016; *La et al.*, 2016; *Loza et al.*, 2010; *Matsunaga and Ziemann*, 2010; *McMurry and Grosjean*, 1985; *Yeh and Ziemann*, 2014; *Zhang et al.*, 2014], it has been demonstrated that operating chambers in continuous-flow mode, as was done in this study, can reduce these losses [*Liu et al.*, 2016; *Shilling et al.*, 2008]. Therefore, the vapor wall-loss rate constant, $k_{wall}$, was varied between $10^{-5}$, $10^{-4}$, and $10^{-3}$ $s^{-1}$ to cover these scenarios and address *(iii)*. In general, we compare the model predicted total concentrations (gas + particle) to observed total concentrations unless otherwise specified so as to minimize the effect of errors in c* estimates. Comparing the model to the measurements requires making assumptions about structures of measured molecular formulas. While the HRToF-CIMS does not provide a measure

of structure, the highly controlled chamber environment allows us to make reasonable assumptions of structures based on the known inputs and generally accepted organic reaction mechanisms.

### 3.2.3 *Quantum Chemical Calculations*

Calculations of rate constants herein are based on the multi-conformer transition state theory (MC-TST) [*Vereecken and Peeters*, 2003] approach with use of quantum chemical methods as outlined in Møller et al. [2016] with slight modifications. A full description is given in the SI. Briefly, a systematic conformer search was carried out in Spartan'14 [2014] using the SYBYL force field.[2014; *Clark et al.*, 1989] Following a subsequent B3LYP/6-31+G(d) [*Becke*, 1993; *Clark et al.*, 1983; *Frisch et al.*, 1984; *Hehre et al.*, 1972; *Lee et al.*, 1988] optimization in Gaussian 09 Revision D.01 [*Frisch et al.*, 2009], all structures within 2 kcal $mol^{-1}$ of the lowest energy structure, were further optimized at the ωB97X-D/aug-cc-pVTZ level of theory [*Chai and Head-Gordon*, 2008; *Dunning*, 1989; *Kendall et al.*, 1992]. For the lowest energy conformer at this level, an ROCCSD(T)-F12a/VDZ-F12 [*Adler et al.*, 2007; *Knizia et al.*, 2009; *Peterson et al.*, 2008; *Watts et al.*, 1993; *Werner et al.*, 2011] energy calculation was conducted in Molpro 2012.1 [*Werner et al.*, 2012], which was used for the barrier height in calculation of the MC-TST reaction rate constant, while ωB97X-D/aug-cc-pVTZ was used for the relative energies between conformers and partition functions. Quantum mechanical tunneling was calculated using the Eckart approach [*Eckart*, 1930]. All calculations were carried out on the R,R stereoisomer of the second generation dihydroxy hydroperoxy peroxy radical ($C_5H_{11}O_6$•) and the products arising from it. The approach by Møller et al. [2016] has been shown to yield calculated reaction rate constants within a factor of five from

experimental results for three peroxy hydrogen shift reactions in the oxidation of methacrolein and 3-pentanone [*Møller et al.*, 2016].

## 3.3 Results & Discussion

Several recent studies have focused on isoprene SOA formation when the IEPOX multiphase pathway was suppressed [*D'Ambro et al.*, 2017; *Krechmer et al.*, 2015; *Liu et al.*, 2016; *Riva et al.*, 2016], and one of the main particle-phase products detected, $ISOP(OOH)_2$, is also detected in the gas-phase in the absence of a large organic aerosol phase [*D'Ambro et al.*, 2017; *Krechmer et al.*, 2015]. The likely mechanism of $ISOP(OOH)_2$ formation has been presented previously [*Liu et al.*, 2016], see also Figure 3.2. Our goal is to test hypotheses for the growth of both the SOA and $ISOP(OOH)_2$ yields with increasing $H_2O_2$ by comparing model predictions to the observed gas- and particle-phase composition. We focus on $ISOP(OOH)_2$ as this compound is the most abundant of a small set of compounds with yields that are highly correlated with the overall SOA mass yield [*Liu et al.*, 2016].

The increasing steady-state yields of SOA and $ISOP(OOH)_2$ with increasing $H_2O_2$, and all else constant (Figure 3.3, bottom), suggests that their formation is in competition with another pathway that suppresses or has less efficient SOA formation (see SI). Increasing $H_2O_2$ mostly leads to increasing $HO_2$ concentrations (Fig. S2). This can affect the absolute amount of low volatility oxidation products that can contribute to SOA and the distribution of functional group types, which might affect volatility and/or condensed phase reactivity. Our overall hypothesis is that multifunctional hydroperoxides with compositions similar to $ISOP(OOH)_2$ are the lowest

volatility gas-phase products formed on the timescales available in the continuous flow chamber, and therefore processes which suppress their yields suppress SOA formation, and vice versa.

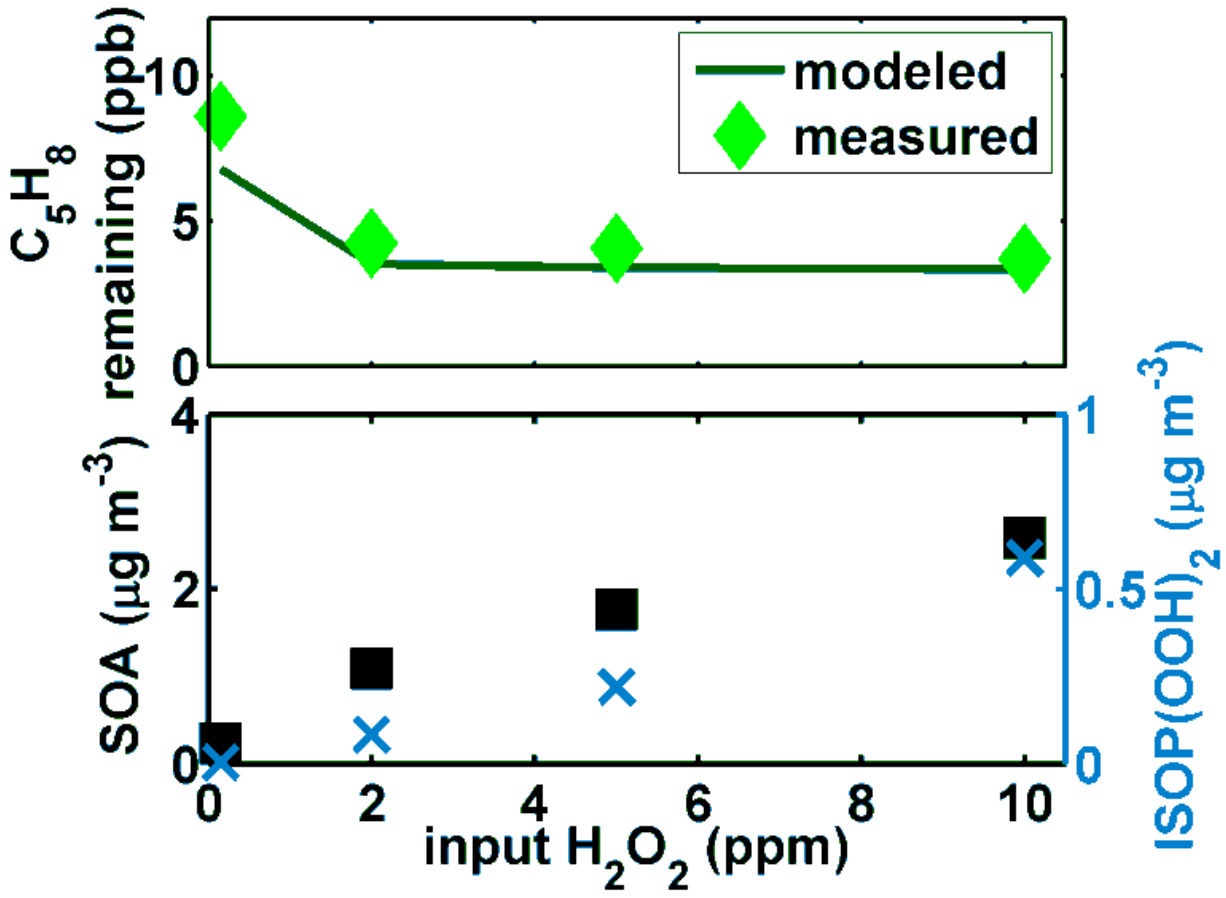


Figure 3.3 Top: Model predicted (line) and measured (diamonds) isoprene remaining in the chamber at steady state. Bottom: Measured $C_5H_{12}O_6$ (blue x's) and SOA (black squares) mass concentration. Note the different y-axis scale.

The box model accurately predicts the amount of isoprene remaining in the chamber at steady-state (Figure 3.3, top), as well as the isoprene decay when chamber lights are turned on, initiating photochemistry (Fig. S1), suggesting that the OH concentration is well constrained. While there are uncertainties in the predicted OH and $HO_2$ concentrations, as we show in the SI, the OH concentration is somewhat buffered against changes in $H_2O_2$ which is both its major source and

sink, decreasing the effect of these uncertainties on our results. The previously discussed behavior of $ISOP(OOH)_2$ and SOA as a function of $H_2O_2$ is displayed in Figure 3.3, bottom, in mass concentration units. As a base-case scenario, we ran the model including only bimolecular reactions for the ISOPOOH-derived $C_5H_{11}O_6$• peroxy radical (i.e. $k_{isom} = 0\ s^{-1}$, Figure 3.4, blue line). This allowed us to test whether the observed decrease in SOA and $ISOP(OOH)_2$ mass yields was due to chemistry already represented in the model. Then, model optimizations, detailed in Figure S3, were conducted to find the values of $k_{isom}$, $\phi$, and $k_{wall}$ that give the best model/measurement agreement. Agreement is defined by both the root mean square difference as well as the $R^2$ between the model and observations for the absolute concentrations (gas+particle) of $ISOP(OOH)_2$, the $ISOP(OOH)_2$ mass yield, and the sum of $C_5H_{10}O_5$, $C_5H_{10}O_6$, and $C_5H_{10}O_7$ concentrations relative to the $ISOP(OOH)_2$ concentration.

When comparing the model to measured $ISOP(OOH)_2$ concentrations, the sensitivity studies (Fig. S3) illustrate three key aspects. First, the agreement with $ISOP(OOH)_2$ is most sensitive to $k_{isom}$, not very sensitive to $k_{wall}$, and less sensitive to the IEPOX yield ($\phi$ in Figure 3.1). Agreement can be achieved with typical literature values for IEPOX formation from ISOPOOH + OH of ~80%. Second, optimal agreement to $ISOP(OOH)_2$ occurs for $k_{wall}$ of $10^{-5}\ s^{-1}$, which is slower than other recent determinations in chambers operated in batch-mode [*Krechmer et al.*, 2016; *La et al.*, 2016; *Matsunaga and Ziemann*, 2010; *McMurry and Grosjean*, 1985; *Yeh and Ziemann*, 2014; *Zhang et al.*, 2014]. We note that while we determine the best model agreement at $10^{-5}\ s^{-1}$, it is not significantly better than those runs at faster vapor wall-loss rates and larger values of $\phi$ to compensate (Fig. S3). Time dependent studies shown in D'Ambro et al. [2017] illustrate an $ISOP(OOH)_2$ lifetime of $\sim 10^4$ s, corresponding to a loss rate of $10^{-4}\ s^{-1}$, consistent

with a faster $k_{wall}$ than applied here, however, we cannot distinguish between vapor wall-loss, photolysis, or reaction in the particle-phase as the source of this loss rate. Thus, it is likely that the IEPOX yield is lower ($C_5H_{11}O_6$• yield is larger) than what we report given that we do not account for the loss of $10^{-4}$ $s^{-1}$ for $ISOP(OOH)_2$. Third, regardless of vapor wall-loss and the IEPOX yield, best agreement was obtained only when the ISOPOOH-derived peroxy radical ($C_5H_{11}O_6$•) isomerization rate, $k_{isom}$, was >0.1 $s^{-1}$.

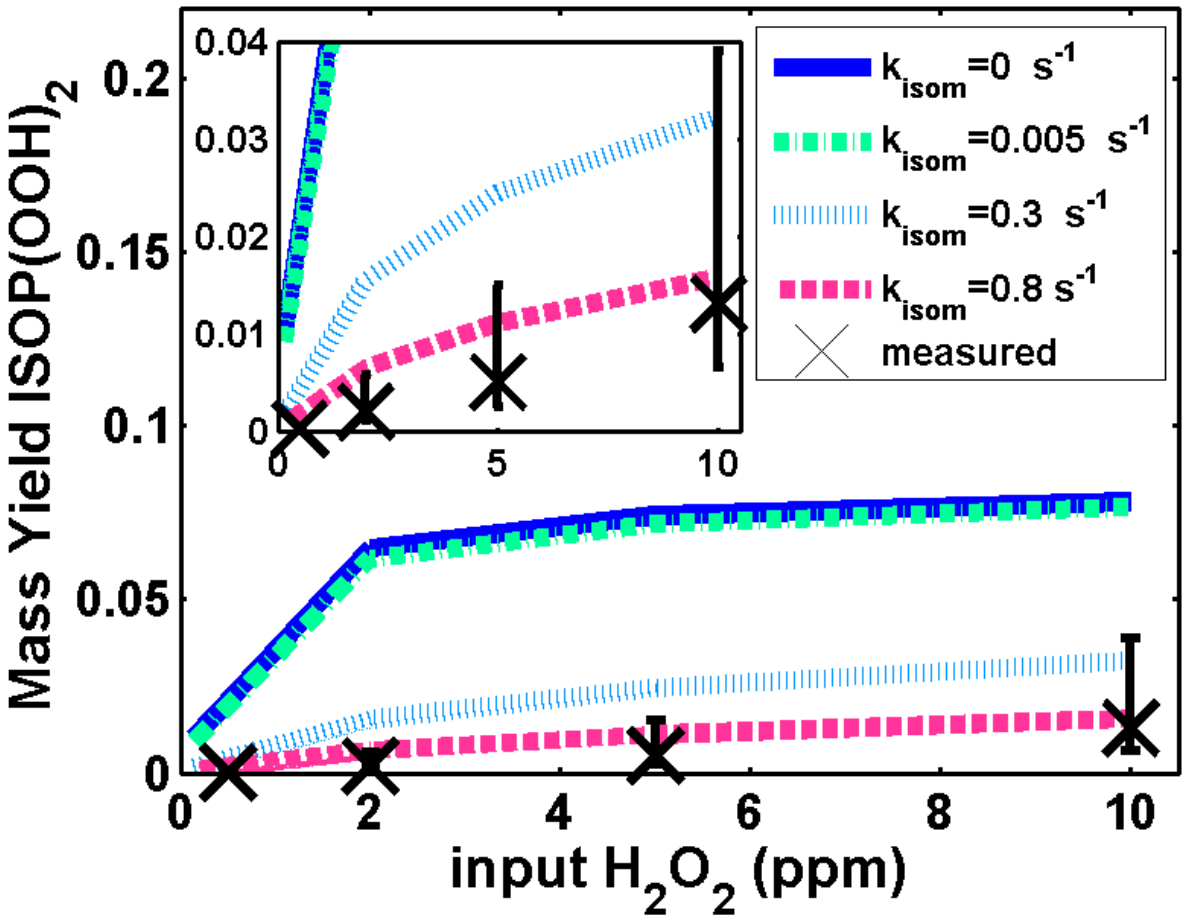


Figure 3.4 Measured mass yield of $C_5H_{12}O_6$ (black x's) and several model results with varying isomerization rates of $C_5H_{11}O_6$ peroxy radical precursor as a function of input $H_2O_2$ (ppm). Inset provides a zoomed-in view to better observe the behavior of the measurements and most representative model run. Measurement error bars reflect our uncertainty in the calibration factor.

The important role of isomerization is demonstrated further in Figure 3.4, where we compare model predicted and observed $ISOP(OOH)_2$ mass yields as a function of $H_2O_2$ in the chamber, used as a proxy for $[HO_2]$ (Fig. S2). Model runs were conducted at isomerization rate constants, $k_{isom}$, of 0 (i.e. the base-case), 0.005, 0.3, and 0.8 $s^{-1}$ and all other parameters the same as the base-case (IEPOX yield of 82%, $k_{wall}$ =$10^{-5}$ $s^{-1}$). The runs at the two slowest isomerization rates (0 and 0.005 $s^{-1}$) are statistically the same and significantly over-predict the $ISOP(OOH)_2$ mass yield relative to the measurements by up to a factor of 30. The runs with $k_{isom}$ of 0.3 and 0.8 $s^{-1}$ are both much closer to the data, with the run at $k_{isom}$ = 0.8 $s^{-1}$ predicting $ISOP(OOH)_2$ mass yields closest to the observations (Figure 3.4, inset), and have the approximate linear increase of yield with $H_2O_2$. We demonstrate in the SI with a steady-state chemical analysis that the dependence of the $ISOP(OOH)_2$ and SOA mass yields on changing input $H_2O_2$ concentrations requires the existence of a pathway such as isomerization that competes with the $RO_2$ + $HO_2$ reaction. Simply increasing $k_{wall}$ or $\phi$ moves the model curve down, but does not change the shape (Fig. S4), nor does [OH] change enough to explain the observations. We can also rule out significant nitric oxide chemistry using our observations of organic nitrates (and $NO_x$) [*D'Ambro et al.*, 2017]. Increasing the $RO_2$ + $RO_2$ reaction rate constant to the kinetic limit also did not improve the agreement. Thus, we conclude that isomerization of the $C_5H_{11}O_6$• peroxy radical competes with the reaction of $C_5H_{11}O_6$• with $HO_2$ and thereby causes the observed trend with $H_2O_2$ concentration.

While Crounse et al. [2011] reported experimentally measured net isomer-weighted isomerization rate of the first generation isoprene hydroxy peroxy radical, $C_5H_9O_3$• ($ISOPO_2$), of

order 0.001 $s^{-1}$, we note specific isomers had larger isomerization rates,[*Crounse et al.*, 2013] and other studies have found the H-shift $k_{isom}$ of methacrolein and a peroxy radical of -OOH substituted 3-pentanone to be 0.5 $s^{-1}$ [*Crounse et al.*, 2012] and >0.1 $s^{-1}$ [*Crounse et al.*, 2013], respectively. Computational studies have also calculated rates similar to these for peroxy radical hydrogen shift reactions [*Møller et al.*, 2016; *Rissanen et al.*, 2014]. Thus, the $k_{isom}$ required for agreement with the observations we present is consistent with $k_{isom}$ for other peroxy radicals.

Our independently performed quantum chemical calculations examined the isomerization rate of $C_5H_{11}O_6$• and possible products for the two most prominent ISOPOOH isomers, 1,2-ISOPOOH (shown in Figure 3.1) and 3,4-ISOPOOH. In Figure 3.5, we show the $C_5H_{11}O_6$• isomers formed from 1,2-ISOPOOH, however, the same is obtained for 3,4-ISOPOOH due to the rapid interconversion between the two peroxy radicals, which has also been previously demonstrated for another hydroperoxy-peroxy system [*Jørgensen et al.*, 2016]. The forward rates of the 1,5 H-shift reactions were found to be 0.3 $s^{-1}$ and 0.9 $s^{-1}$ for the two isomers, respectively (Figure 3.5). The reverse rates in both cases were too slow at room temperature to compete with epoxide formation or the addition of $O_2$ to the resulting alkyl radical, which presumably occurs near the kinetic limit (~$10^8$ $s^{-1}$ at 1 atm total pressure) as previously shown [*Park et al.*, 2004]. Thus, the ISOPOOH-derived $RO_2$ will convert into other products due to intramolecular H-shifts at a net forward rate of order 0.3 $s^{-1}$ or faster according to the quantum chemical calculations, consistent with the observations and box modeling described above. The fact that the box model and quantum chemical calculations independently arrive at a similar value for the rate of $C_5H_{11}O_6$• isomerization supports the hypothesis that such a pathway competes with $HO_2$, not only in the chamber, but also the atmosphere where $HO_2$ concentrations are significantly lower.

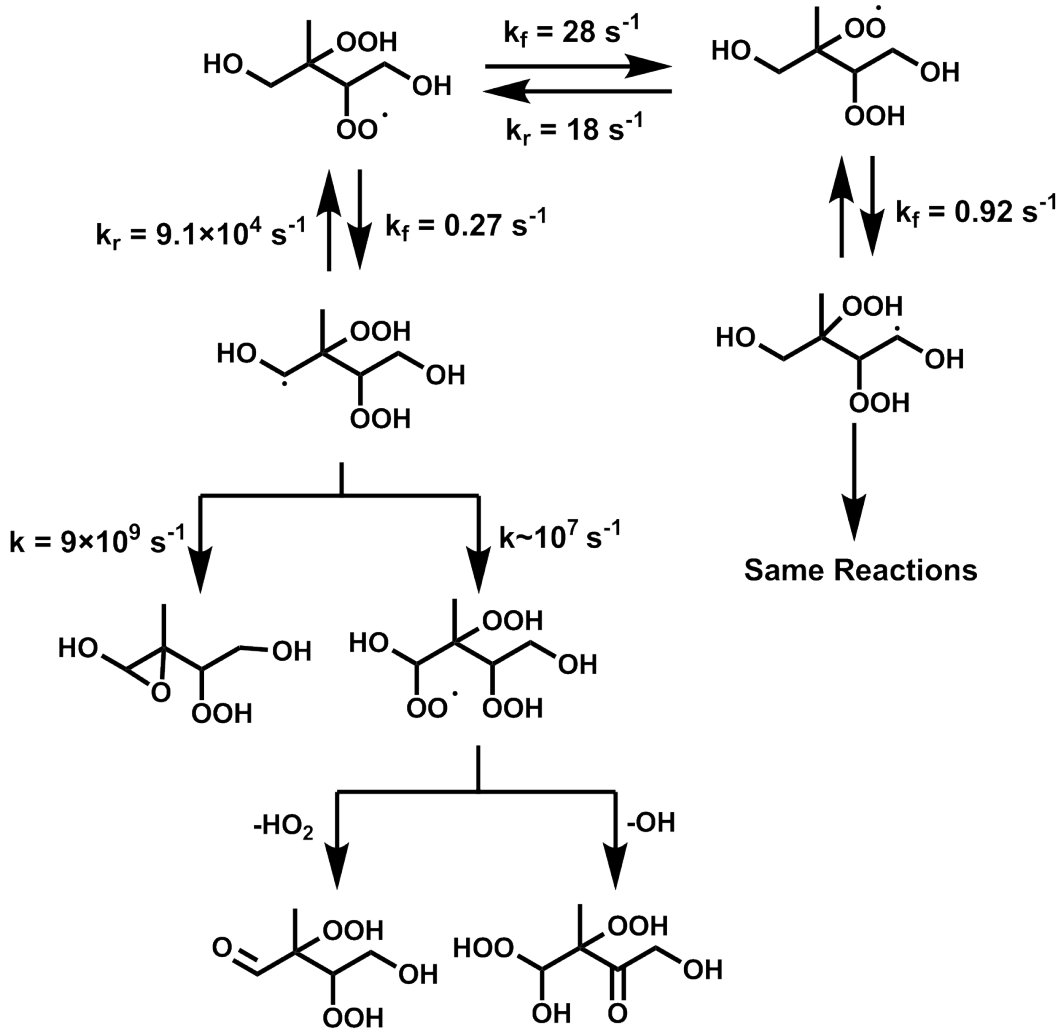


Figure 3.5 Proposed detailed mechanism and calculated rates of the isomerization of one isomer of $C_5H_{11}O_6$, the peroxy radical formed from ISOPOOH + OH in Figure 3.1.

For isomerization of the ISOPOOH-derived $RO_2$ to explain a decreasing SOA mass yield, the products that result from the isomerization must be of higher volatility than $ISOP(OOH)_2$. The quantum chemical calculations predict three possible products: a hydroxy dihydroperoxy aldehyde or ketone ($C_5H_{10}O_6$ or $C_5H_{10}O_7$, respectively) and a dihydroxy hydroperoxy epoxide ($C_5H_{10}O_5$), (Schemes 2 and 3). Additionally, $C_5H_{10}O_5$ could be a dihydroxy hydroperoxy aldehyde formed from addition of OH to the internal carbon of the remaining ISOPOOH double

bond (Scheme S1). Previous studies suggest branching to this pathway is a few percent [*Paulot et al.*, 2009a; *Peeters et al.*, 2007; *Ziemann and Atkinson*, 2012], and so was not included. As it is also a product of isomerization, it does not affect our determination of $k_{isom}$ or conclusions (see SI). The calculations suggest that formation of the epoxide, analogous mechanistically to the formation of IEPOX [*Paulot et al.*, 2009b], is one to two orders of magnitude faster than $O_2$ addition to form the aldehyde/ketone, where $O_2$ addition occurs at a rate of ~$10^7$ $s^{-1}$ for both 1,2- and 3,4-ISOPOOH and epoxide formation occurs at calculated rates of $9 \times 10^9$ or $3 \times 10^8$ $s^{-1}$ for 1,2- and 3,4-ISOPOOH, respectively. That an epoxide is formed is intriguing, suggesting that epoxide formation may be a more general characteristic of isoprene oxidation rather than specific to IEPOX, and that epoxide formation when a hydroperoxide is α to a carbon-centered radical is more common than our current mechanisms of VOC oxidation suggests.

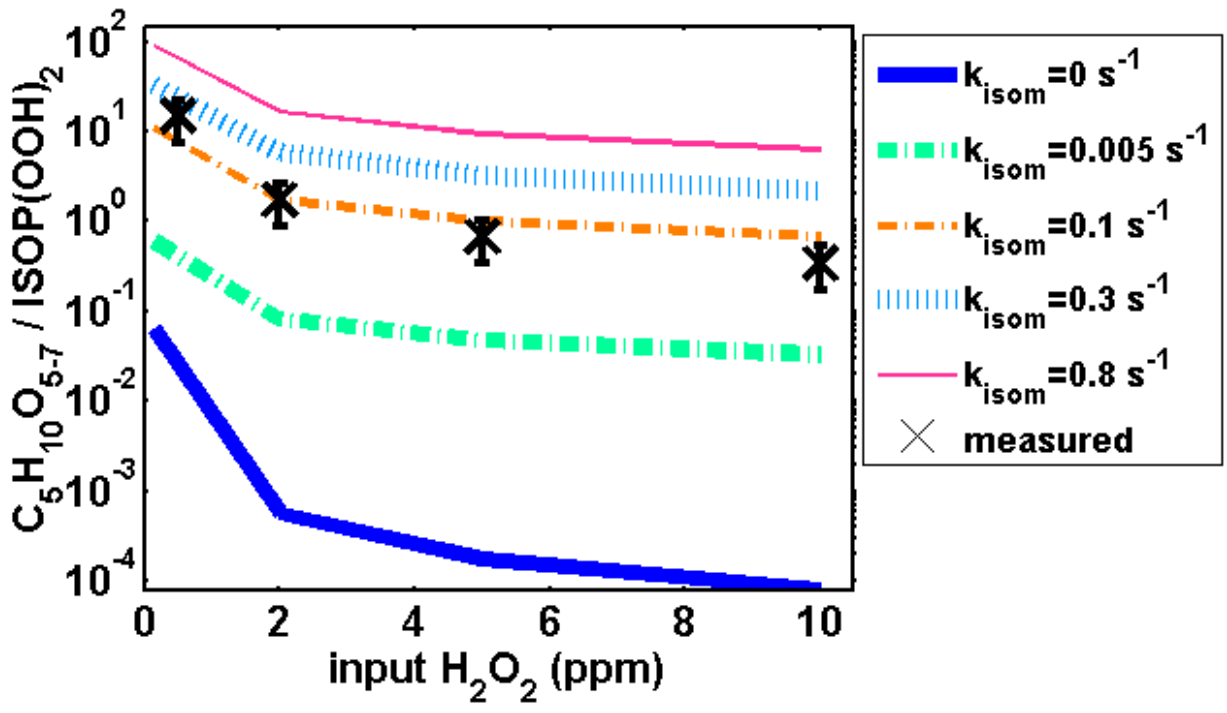


Figure 3.6 The ratio of the sum of $C_5H_{11}O_6$• isomerization products relative to the product of reaction with $HO_2$ for measurements (black x's) and various model results (lines) at varying

$C_5H_{11}O_6$• isomerization rates. Measurement error bars reflect our uncertainty in calibration factors.

Although the FIGAERO HRToF-CIMS does not provide structural information, we can assess whether the products of $C_5H_{11}O_6$• peroxy radical isomerization are consistent with the observed compositions of measured oxidation products. Figure 3.6 shows the behavior of the sum of isomerization products relative to the $HO_2$ bimolecular reaction product, where we assume ions with the compositions $C_5H_{10}O_5$, $C_5H_{10}O_6$, and $C_5H_{10}O_7$ correspond to the predicted epoxide, aldehyde, and ketone products, respectively. The model predicts the relative shape of the relationship with respect to $H_2O_2$ correctly, but the absolute agreement in the ratio of these products is better for $k_{isom}$ of ~0.1 $s^{-1}$, as opposed to the 0.3 – 0.8 $s^{-1}$ suggested by the comparison to the concentration of $ISOP(OOH)_2$. Uncertainties in the relative loss rates assumed in the model and in the relative instrument response to these various products likely explain such discrepancies. The results shown in Figures 2 and 3, combined with the quantum calculations, all point to a $k_{isom}$ of 0.1-0.8 $s^{-1}$. That independent approaches all arrive at $k_{isom} > 0.1$ $s^{-1}$ therefore has important implications for SOA formation from isoprene in the atmosphere.

The SOA mass concentration and the distribution of compounds in the particle-phase provide an additional test of the model. Figure 3.7, top, shows that a $C_5H_{11}O_6$• $k_{isom}$ of 0.3 $s^{-1}$ provides good model/measurement agreement of the SOA abundance ($R^2$=0.98). The base-case model over-predicts SOA, while $k_{isom}$ of 0.8 $s^{-1}$ slightly under-predicts SOA. Consistent with the observations, the modeled SOA contains 36% $ISOP(OOH)_2$ (Figure 3.7, bottom), with other major components matching compositions of major components measured by the FIGAERO

HRToF-CIMS. The model predicts that the dihydroxy hydroperoxy epoxide formed from $C_5H_{11}O_6$• isomerization makes up 48% of the aerosol composition at the highest $HO_2$ concentration and $k_{isom}$ of 0.8 $s^{-1}$, while it was observed to be 11%.

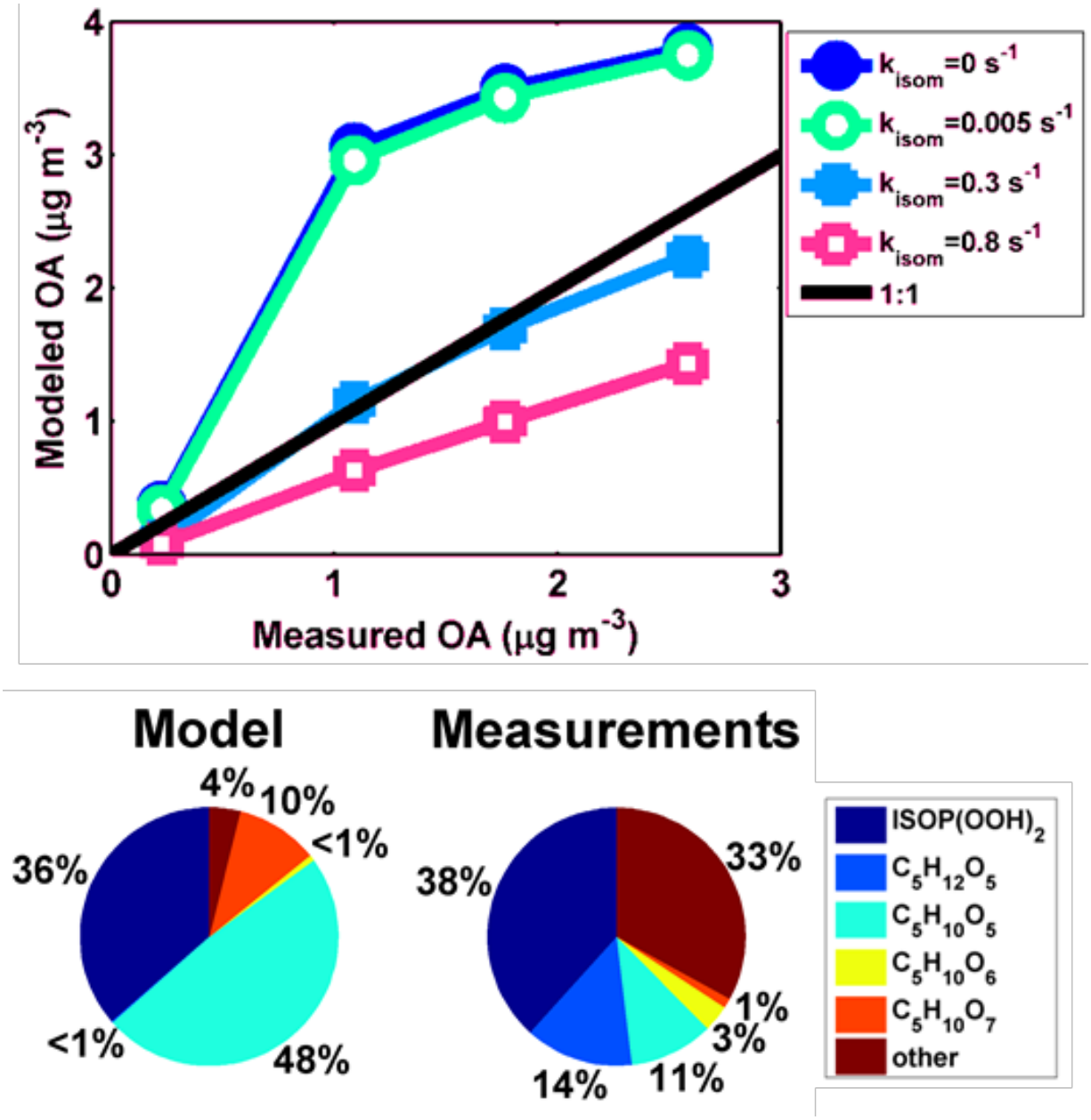


Figure 3.7 Top: model OA concentrations plotted versus measurements for model runs with $10^{-5}$ $s^{-1}$ wall loss, 11% $C_5H_{11}O_6$ yield, and varying isomerization rates ($s^{-1}$). Bottom: pie charts of the

most prolific particle phase species modeled (left) for the data point in the above plot circled in yellow, and measured (right) in μg $m^{-3}$.

We do not expect perfect agreement between measured and modeled SOA abundance and composition, in part because previous studies have shown that up to 50% of this non-IEPOX SOA is possibly low volatility accretion-like products[*D'Ambro et al.*, 2017] likely formed from multiphase chemistry which is not included in the model. Thus, we expect to under-predict measured SOA by as much as a factor of two with F0AM, as well as to be unable to simulate observed products which are the result of thermal decomposition of low volatility oligomers during the desorption analysis. As such, we conclude that the overall agreement with observations in the predicted SOA mass abundance, dominant products, and response to changing $H_2O_2$ is reasonable, and that constraining $k_{isom}$ for the $C_5H_{11}O_6$• peroxy radical at >0.1 $s^{-1}$ is more important than $k_{wall}$ for predicting the SOA yield.

## 3.4 Atmospheric Implications

We utilize quantum chemical calculations and a detailed chemical kinetics box model compared to measurements of gas- and particle-phase oxidation products of isoprene made in an environmental chamber. To explain the responses of product distributions and SOA mass concentrations to changes in chamber radical conditions, the $C_5H_{11}O_6$• peroxy radical formed from ISOPOOH + OH must undergo intra-molecular H-atom shift reactions ("$RO_2$ isomerization") at rates exceeding 0.1 $s^{-1}$ to form products 1-2 orders of magnitude higher volatility than that of $ISOP(OOH)_2$, which forms if the peroxy radical reacts with $HO_2$. Such a pathway has significant implications for how low-NO chamber studies should be conducted, and

offers a way to reconcile differences in SOA yields measured under different chamber conditions [*Krechmer et al.*, 2015; *Kroll et al.*, 2006; *Liu et al.*, 2016; *Riva et al.*, 2016].

While $ISOP(OOH)_2$ and related highly oxygenated $C_5$ compounds believed to come from the $ISOP(OOH)_2$ pathway, have been observed in the Southeastern U.S. atmosphere during the SOAS 2013 field campaign, their abundance was only a few percent of the total SOA in an isoprene dominated region [*Riva et al.*, 2016]. Using SOAS diurnally averaged measurements of $HO_2$ and NO, and our F0AM model presented here, we calculate the vast majority, >96%, of the $C_5H_{11}O_6$• will undergo isomerization instead of forming the lowest volatility $ISOP(OOH)_2$ and related products.

The quantum calculations suggest the most likely product of the isomerization is a dihydroxy hydroperoxy epoxide. While we and others observe a major second generation product with the composition ($C_5H_{10}O_5$) of such an epoxide [*Krechmer et al.*, 2015], confirmation of the structure remains necessary. Epoxides in general undergo heterogeneous uptake and acid catalyzed ring opening with the potential to form SOA through subsequent substitution reactions [*Eddingsaas et al.*, 2010; *Surratt et al.*, 2007; *Surratt et al.*, 2006]. However, we speculate that the dominant fate in aqueous acidic particles of this specific epoxide moiety will be nearly instantaneous conversion to a dihydroxy hydroperoxy carbonyl, but direct experimental evidence is needed. That said, its lower volatility relative to IEPOX will allow it to partition more strongly to an organic phase where it may undergo accretion chemistry.

The dominance of epoxide formation over $O_2$ addition to a carbon radical α to a hydroperoxyl group, as calculated herein and for the case of IEPOX, suggests gas-phase epoxide formation may be more common than current atmospheric chemistry mechanisms allow. Such a situation would have implications for the propensity of acidity enhanced SOA formation from a variety of biogenic and anthropogenic VOC [*Eddingsaas et al.*, 2010; *Gaston et al.*, 2014; *Surratt et al.*, 2010; *Surratt et al.*, 2006]. For example, the peroxy radical autoxidation, where peroxy radicals form multiple hydroperoxide moieties by several intra-molecular H-shifts could well terminate to epoxides. Epoxide formation has been commonly suggested, particularly for aromatic systems [*Bartolotti and Edney*, 1995; *Glowacki et al.*, 2009; *Motta et al.*, 2002; *Pan and Wang*, 2014; *Richters et al.*, 2016; *Suh et al.*, 2003; *Yu and Jeffries*, 1997], supporting the idea that epoxides are potentially a feature of low $NO_x$ oxidation of non-aromatics when a radical center occurs α to a hydroperoxy group. Moreover, there is also recent evidence for epoxide formation from $-ONO_2$ groups α to the carbon radical [*Jacobs et al.*, 2014; *L Lee et al.*, 2014; *St Clair et al.*, 2016]. Thus, we suggest analytical methods specific to epoxides be developed for assessing their ubiquity in the atmosphere and chamber studies.

## 3.5 Supporting Information

The supporting information is available free of charge on the ACS publications website at DOI: 10.1021/acs.est.7b00460. The Supporting information includes: further details on chamber conditions, the 0-D chemical kinetics model, quantum chemical calculations, and the dependence of ISOP(OOH)2 and SOA mass yields on $H_2O_2$. It also includes: tables showing molecular formulas, structures, SMILE, and compound names; a complete list of all reactions, rate constants, and yields; and experimental conditions. There is also an additional ISOPOOH + OH

reaction scheme and figures showing the decay of isoprene, modeled $HO_2$ concentration and fraction of $RO_2$ reacting through different pathways, model sensitivity, and $ISOP(OOH)_2$ mass yields at a lower peroxy radical yield.

References

(2014), Spartan '14, edited, Wavefunction Inc., Irvine, CA.

Adler, T. B., G. Knizia, and H. J. Werner (2007), A simple and efficient CCSD(T)-F12 approximation, *J. Chem. Phys.*, *127*(22).

Atkinson, R., and A. C. Lloyd (1984), Evaluation of kinetic and mechanistic data for modeling of photochemical smog, *J. Phys. Chem. Ref. Data*, *13*(2), 315-444.

Atkinson, R., S. M. Aschmann, E. C. Tuazon, J. Arey, and B. Zielinska (1989), Formation of 3-methylfuran from the gas-phase reaction of OH radicals with isoprene and the rate-constant for its reaction with the OH radical *Int. J. Chem. Kinet.*, *21*(7), 593-604.

Bartolotti, L. J., and E. O. Edney (1995), Density-functional theory derived intermediates from the OH initiated atmospheric oxidation of toluene, *Chem. Phys. Lett.*, *245*(1), 119-122.

Becke, A. D. (1993), Density-functional thermochemistry .3. The role of exact exchange, *J. Chem. Phys.*, *98*(7), 5648-5652.

Chai, J.-D., and M. Head-Gordon (2008), Long-range corrected hybrid density functionals with damped atom-atom dispersion corrections, *Phys. Chem. Chem. Phys.*, *10*(44), 6615-6620.

Clark, M., R. D. Cramer, and N. Vanopdenbosch (1989), Validation of the general-purpose TRIPOS 5.2 force-field, *J. Comput. Chem.*, *10*(8), 982-1012.

Clark, T., J. Chandrasekhar, G. W. Spitznagel, and P. V. Schleyer (1983), Efficient diffuse function-augmented basis sets for anion calculations. III. The 3-21+G basis set for first-row elements, Li-F *J. Comput. Chem.*, *4*(3), 294-301.

Compernolle, S., K. Ceulemans, and J. F. Muller (2011), EVAPORATION: a new vapour pressure estimation method for organic molecules including non-additivity and intramolecular interactions, *Atmos. Chem. Phys.*, *11*(18), 9431-9450.

Crounse, J. D., F. Paulot, H. G. Kjaergaard, and P. O. Wennberg (2011), Peroxy radical isomerization in the oxidation of isoprene, *Phys. Chem. Chem. Phys.*, *13*(30), 13607-13613.

Crounse, J. D., L. B. Nielsen, S. Jørgensen, H. G. Kjaergaard, and P. O. Wennberg (2013), Autoxidation of organic compounds in the atmosphere, *J. Phys. Chem. Lett.*, *4*(20), 3513-3520.

Crounse, J. D., H. C. Knap, K. B. Ornso, S. Jørgensen, F. Paulot, H. G. Kjaergaard, and P. O. Wennberg (2012), Atmospheric fate of methacrolein. 1. Peroxy radical isomerization following addition of OH and O-2, *J. Phys. Chem. A*, *116*(24), 5756-5762.

Crump, J. G., R. C. Flagan, and J. H. Seinfeld (1983), Particle wall loss rates in vessels, *Aerosol Sci. Technol.*, *2*(3), 303-309.

D'Ambro, E. L., et al. (2017), Molecular composition and volatility of isoprene photochemical oxidation secondary organic aerosol under low- and high-NOx conditions, *Atmos. Chem. Phys.*, *17*(1), 159-174.

Donahue, N. M., E. R. Trump, J. R. Pierce, and I. Riipinen (2011), Theoretical constraints on pure vapor-pressure driven condensation of organics to ultrafine particles, *Geophys. Res. Lett.*, *38*(16), L16801.

Dunning, T. H. (1989), Gaussian-basis sets for use in correlated molecular calculations .1. The atoms boron through neon and hydrogen, *J. Chem. Phys.*, *90*(2), 1007-1023.

Eckart, C. (1930), The penetration of a potential barrier by electrons, *Phys. Rev.*, *35*(11), 1303-1309.

Eddingsaas, N. C., D. G. VanderVelde, and P. O. Wennberg (2010), Kinetics and products of the acid-catalyzed ring-opening of atmospherically relevant butyl epoxy alcohols, *J. Phys. Chem. A*, *114*(31), 8106-8113.

Frisch, M. J., J. A. Pople, and J. S. Binkley (1984), Self-consistent molecular-orbital methods .25. Supplementary functions for gaussian-basis sets *J. Chem. Phys.*, *80*(7), 3265-3269.

Frisch, M. J., et al. (2009), Gaussian 09 Revision D.01.

Gaston, C. J., T. P. Riedel, Z. F. Zhang, A. Gold, J. D. Surratt, and J. A. Thornton (2014), Reactive uptake of an isoprene-derived epoxydiol to submicron aerosol particles, *Environ. Sci. Technol.*, *48*(19), 11178-11186.

Glowacki, D. R., L. M. Wang, and M. J. Pilling (2009), Evidence of formation of bicyclic species in the early stages of atmospheric benzene oxidation, *J. Phys. Chem. A*, *113*(18), 5385-5396.

Guenther, A. B., X. Jiang, C. L. Heald, T. Sakulyanontvittaya, T. Duhl, L. K. Emmons, and X. Wang (2012), The model of emissions of gases and aerosols from nature version 2.1 (MEGAN2.1): an extended and updated framework for modeling biogenic emissions, *Geosci. Model Dev.*, *5*(6), 1471-1492.

Hehre, W. J., R. Ditchfield, and J. A. Pople (1972), Self-consistent molecular-orbital methods .12. Further extensions of gaussian-type basis sets for use in molecular-orbital studies of organic-molecules *J. Chem. Phys.*, *56*(5), 2257-+.

Hilal, S. H., S. W. Karickhoff, and L. A. Carreira (2003), Prediction of the vapor pressure boiling point, heat of vaporization and diffusion coefficient of organic compounds, *QSAR Comb. Sci.*, *22*(6), 565-574.

Jacobs, M. I., W. J. Burke, and M. J. Elrod (2014), Kinetics of the reactions of isoprene-derived hydroxynitrates: gas phase epoxide formation and solution phase hydrolysis, *Atmos. Chem. Phys.*, *14*(17), 8933-8946.

Jenkin, M. E., J. C. Young, and A. R. Rickard (2015), The MCM v3.3.1 degradation scheme for isoprene, *Atmos. Chem. Phys.*, *15*(20), 11433-11459.

Jimenez, J. L., et al. (2009), Evolution of organic aerosols in the atmosphere, *Science*, *326*(5959), 1525-1529.

Jørgensen, S., H. C. Knap, R. V. Otkjaer, A. M. Jensen, M. L. H. Kjeldsen, P. O. Wennberg, and H. G. Kjaergaard (2016), Rapid hydrogen shift scrambling in hydroperoxy-substituted organic peroxy radicals, *J. Phys. Chem. A*, *120*(2), 266-275.

Kendall, R. A., T. H. Dunning, and R. J. Harrison (1992), Electron-affinities of the 1st-row atoms revisted- Systematic basis-sets and wave-functions *J. Chem. Phys.*, *96*(9), 6796-6806.

Knizia, G., T. B. Adler, and H. J. Werner (2009), Simplified CCSD(T)-F12 methods: Theory and benchmarks, *J. Chem. Phys.*, *130*(5).

Krechmer, J. E., D. Pagonis, P. J. Ziemann, and J. L. Jimenez (2016), Quantification of gas-wall partitioning in teflon environmental chambers using rapid bursts of low-volatility oxidized species generated in situ, *Environ. Sci. Technol.*, *50*(11), 5757-5765.

Krechmer, J. E., et al. (2015), Formation of low volatility organic compounds and Secondary Organic Aerosol from isoprene hydroxyhydroperoxide low-NO oxidation, *Environ. Sci. Technol.*, *49*(17), 10330-10339.

Kroll, J. H., N. L. Ng, S. M. Murphy, R. C. Flagan, and J. H. Seinfeld (2006), Secondary organic aerosol formation from isoprene photooxidation, *Environ. Sci. Technol.*, *40*(6), 1869-1877.

La, Y. S., M. Camredon, P. J. Ziemann, R. Valorso, A. Matsunaga, V. Lannuque, J. Lee-Taylor, A. Hodzic, S. Madronich, and B. Aumont (2016), Impact of chamber wall loss of gaseous organic compounds on secondary organic aerosol formation: explicit modeling of SOA formation from alkane and alkene oxidation, *Atmos. Chem. Phys.*, *16*(3), 1417-1431.

Lee, B. H., F. D. Lopez-Hilfiker, C. Mohr, T. Kurten, D. R. Worsnop, and J. A. Thornton (2014), An iodide-adduct high-resolution time-of-flight chemical-ionization mass spectrometer: application to atmospheric inorganic and organic compounds, *Environ. Sci. Technol.*, *48*(11), 6309-6317.

Lee, C. T., W. T. Yang, and R. G. Parr (1988), Development of the Colle-Salvetti correlation-energy formula into a functional of the electron-density *Phys. Rev. B*, *37*(2), 785-789.

Lee, L., A. P. Teng, P. O. Wennberg, J. D. Crounse, and R. C. Cohen (2014), On rates and mechanisms of OH and O3 reactions with isoprene-derived hydroxy nitrates, *J. Phys. Chem. A*, *118*(9), 1622-1637.

Lin, Y. H., E. M. Knipping, E. S. Edgerton, S. L. Shaw, and J. D. Surratt (2013a), Investigating the influences of SO2 and NH3 levels on isoprene-derived secondary organic aerosol formation using conditional sampling approaches, *Atmos. Chem. Phys.*, *13*(16), 8457-8470.

Lin, Y. H., H. Budisulistiorini, K. Chu, R. A. Siejack, H. F. Zhang, M. Riva, Z. F. Zhang, A. Gold, K. E. Kautzman, and J. D. Surratt (2014), Light-absorbing oligomer formation in secondary organic aerosol from reactive uptake of isoprene epoxydiols, *Environ. Sci. Technol.*, *48*(20), 12012-12021.

Lin, Y. H., et al. (2012), Isoprene epoxydiols as precursors to secondary organic aerosol formation: Acid-catalyzed reactive uptake studies with authentic compounds, *Environ. Sci. Technol.*, *46*(1), 250-258.

Lin, Y. H., et al. (2013b), Epoxide as a precursor to secondary organic aerosol formation from isoprene photooxidation in the presence of nitrogen oxides, *Proc. Natl. Acad. Sci. U. S. A.*, *110*(17), 6718-6723.

Liu, J. M., et al. (2016), Efficient isoprene secondary organic aerosol formation from a non-IEPOX pathway, *Environ. Sci. Technol.*, *50*(18), 9872-9880.

Liu, S., J. E. Shilling, C. Song, N. Hiranuma, R. A. Zaveri, and L. M. Russell (2012), Hydrolysis of organonitrate functional groups in aerosol particles, *Aerosol Sci. Technol.*, *46*(12), 1359-1369.

Liu, Y., M. Kuwata, B. F. Strick, F. M. Geiger, R. J. Thomson, K. A. McKinney, and S. T. Martin (2014), Uptake of epoxydiol isomers accounts for half of the particle-phase material produced from isoprene photooxidation via the HO pathway, *Environ. Sci. Technol.*, *49*, 250-258.

Lopez-Hilfiker, F. D., et al. (2014), A novel method for online analysis of gas and particle composition: description and evaluation of a Filter Inlet for Gases and AEROsols (FIGAERO), *Atmos. Meas. Tech.*, *7*(4), 983-1001.

Loza, C. L., A. W. H. Chan, M. M. Galloway, F. N. Keutsch, R. C. Flagan, and J. H. Seinfeld (2010), Characterization of vapor wall loss in laboratory chambers, *Environ. Sci. Technol.*, *44*(13), 5074-5078.

Matsunaga, A., and P. J. Ziemann (2010), Gas-wall partitioning of organic compounds in a teflon film chamber and potential effects on reaction product and aerosol yield measurements, *Aerosol Sci. Technol.*, *44*(10), 881-892.

McMurry, P. H., and D. Grosjean (1985), Gas and aerosol wall losses in teflon film smog chambers *Environ. Sci. Technol.*, *19*(12), 1176-1182.

Miyoshi, A., S. Hatakeyama, and N. Washida (1994), OH radical-initiated photooxidation of isoprene- an estimate of global CO production, *J. Geophys. Res.-Atmos.*, *99*(D9), 18779-18787.

Møller, K. H., R. V. Otkjær, N. Hyttinen, T. Kurtén, and H. G. Kjaergaard (2016), Cost-Effective Implementation of Multiconformer Transition State Theory for Peroxy Radical Hydrogen Shift Reactions, *J. Phys. Chem. A*, *120*(51), 10072-10087.

Motta, F., G. Ghigo, and G. Tonachini (2002), Oxidative degradation of benzene in the troposphere. Theoretical mechanistic study of the formation of unsaturated dialdehydes and dialdehyde epoxides, *J. Phys. Chem. A*, *106*(17), 4411-4422.

Pan, S. S., and L. M. Wang (2014), Atmospheric oxidation mechanism of m-xylene initiated by OH radical, *J. Phys. Chem. A*, *118*(45), 10778-10787.

Pankow, J. F. (1994), An absorption-model of the gas aerosol partitioning involved in the formation of secondary organic aerosol *Atmos. Environ.*, *28*(2), 189-193.

Park, J., C. G. Jongsma, R. Y. Zhang, and S. W. North (2004), OH/OD initiated oxidation of isoprene in the presence of O-2 and NO, *J. Phys. Chem. A*, *108*(48), 10688-10697.

Paulot, F., J. D. Crounse, H. G. Kjaergaard, J. H. Kroll, J. H. Seinfeld, and P. O. Wennberg (2009a), Isoprene photooxidation: new insights into the production of acids and organic nitrates, *Atmos. Chem. Phys.*, *9*(4), 1479-1501.

Paulot, F., J. D. Crounse, H. G. Kjaergaard, A. Kurten, J. M. St Clair, J. H. Seinfeld, and P. O. Wennberg (2009b), Unexpected epoxide formation in the gas-phase photooxidation of isoprene, *Science*, *325*(5941), 730-733.

Paulson, S. E., and J. H. Seinfeld (1992), Development and evaluation of a photooxidation mechanism for isoprene *J. Geophys. Res.-Atmos.*, *97*(D18), 20703-20715.

Peeters, J., T. L. Nguyen, and L. Vereecken (2009), HOx radical regeneration in the oxidation of isoprene, *Phys. Chem. Chem. Phys.*, *11*(28), 5935-5939.

Peeters, J., J. F. Muller, T. Stavrakou, and V. S. Nguyen (2014), Hydroxyl radical recycling in isoprene oxidation driven by hydrogen bonding and hydrogen tunneling: the upgraded LIM1 mechanism, *J. Phys. Chem. A*, *118*(38), 8625-8643.

Peeters, J., W. Boullart, V. Pultau, S. Vandenberk, and L. Vereecken (2007), Structure-activity relationship for the addition of OH to (poly)alkenes: Site-specific and total rate constants, *J. Phys. Chem. A*, *111*(9), 1618-1631.

Peterson, K. A., T. B. Adler, and H. J. Werner (2008), Systematically convergent basis sets for explicitly correlated wavefunctions: The atoms H, He, B-Ne, and Al-Ar, *J. Chem. Phys.*, *128*(8).

Poschl, U. (2005), Atmospheric aerosols: Composition, transformation, climate and health effects, *Angew. Chem.-Int. Edit.*, *44*(46), 7520-7540.

Richters, S., H. Herrmann, and T. Berndt (2016), Different pathways of the formation of highly oxidized multifunctional organic compounds (HOMs) from the gas-phase ozonolysis of beta-caryophyllene, *Atmos. Chem. Phys.*, *16*(15), 9831-9845.

Rissanen, M. P., et al. (2014), The formation of highly oxidized multifunctional products in the ozonolysis of cyclohexene, *J. Am. Chem. Soc.*, *136*(44), 15596-15606.

Riva, M., et al. (2016), Chemical characterization of secondary organic aerosol from oxidation of isoprene hydroxyhydroperoxides, *Environ. Sci. Technol.*, *50*(18), 9889-9899.

Saleh, R., N. M. Donahue, and A. L. Robinson (2013), Time scales for gas-particle partitioning equilibration of secondary organic aerosol formed from alpha-pinene ozonolysis, *Environ. Sci. Technol.*, *47*(11), 5588-5594.

Schichtel, B. A., W. C. Malm, G. Bench, S. Fallon, C. E. McDade, J. C. Chow, and J. G. Watson (2008), Fossil and contemporary fine particulate carbon fractions at 12 rural and urban sites in the United States, *J. Geophys. Res.-Atmos.*, *113*(D2), D02311.

Shilling, J. E., Q. Chen, S. M. King, T. Rosenoern, J. H. Kroll, D. R. Worsnop, K. A. McKinney, and S. T. Martin (2008), Particle mass yield in secondary organic aerosol formed by the dark ozonolysis of alpha-pinene, *Atmos. Chem. Phys.*, *8*(7), 2073-2088.

St Clair, J. M., J. C. Rivera-Rios, J. D. Crounse, H. C. Knap, K. H. Bates, A. P. Teng, S. Jørgensen, H. G. Kjaergaard, F. N. Keutsch, and P. O. Wennberg (2016), Kinetics and products of the reaction of the first-generation isoprene hydroxy hydroperoxide (ISOPOOH) with OH, *J. Phys. Chem. A*, *120*(9), 1441-1451.

Suh, I., R. Y. Zhang, L. T. Molina, and M. J. Molina (2003), Oxidation mechanism of aromatic peroxy and bicyclic radicals from OH-toluene reactions, *J. Am. Chem. Soc.*, *125*(41), 12655-12665.

Surratt, J. D., M. Lewandowski, J. H. Offenberg, M. Jaoui, T. E. Kleindienst, E. O. Edney, and J. H. Seinfeld (2007), Effect of acidity on secondary organic aerosol formation from isoprene, *Environ. Sci. Technol.*, *41*(15), 5363-5369.

Surratt, J. D., A. W. H. Chan, N. C. Eddingsaas, M. N. Chan, C. L. Loza, A. J. Kwan, S. P. Hersey, R. C. Flagan, P. O. Wennberg, and J. H. Seinfeld (2010), Reactive intermediates revealed in secondary organic aerosol formation from isoprene, *Proc. Natl. Acad. Sci. U. S. A.*, *107*(15), 6640-6645.

Surratt, J. D., et al. (2006), Chemical composition of secondary organic aerosol formed from the photooxidation of isoprene, *J. Phys. Chem. A*, *110*(31), 9665-9690.

Tuazon, E. C., and R. Atkinson (1990), A product study of the gas-phase reaction of isoprene with the OH radical in the presence of NOx, *Int. J. Chem. Kinet.*, *22*(12), 1221-1236.

Vereecken, L., and J. Peeters (2003), The 1,5-H-shift in 1-butoxy: A case study in the rigorous implementation of transition state theory for a multirotamer system, *J. Chem. Phys.*, *119*(10), 5159-5170.

Watts, J. D., J. Gauss, and R. J. Bartlett (1993), Coupled-cluster methods with noniterative triple excitations for restricted open-shell Hartree-Fock and other general single determinant reference functions - Energies and analytical gradients *J. Chem. Phys.*, *98*(11), 8718-8733.

Weber, R. J., et al. (2007), A study of secondary organic aerosol formation in the anthropogenic-influenced southeastern United States, *J. Geophys. Res.-Atmos.*, *112*(D13), D13302.

Werner, H. J., G. Knizia, and F. R. Manby (2011), Explicitly correlated coupled cluster methods with pair-specific geminals, *Mol. Phys.*, *109*(3), 407-417.

Werner, H. J., et al. (2012), Molpro, version 2012.1, a package of ab initio programs.

Wolfe, G. M., and J. A. Thornton (2011), The Chemistry of Atmosphere-Forest Exchange (CAFE) Model - Part 1: Model description and characterization, *Atmos. Chem. Phys.*, *11*(1), 77-101.

Wolfe, G. M., J. A. Thornton, M. McKay, and A. H. Goldstein (2011a), Forest-atmosphere exchange of ozone: sensitivity to very reactive biogenic VOC emissions and implications for in-canopy photochemistry, *Atmos. Chem. Phys.*, *11*(15), 7875-7891.

Wolfe, G. M., M. R. Marvin, S. J. Roberts, K. R. Travis, and J. Liao (2016), The Framework for 0-D Atmospheric Modeling (F0AM) v3.1, *Geosci. Model Dev.*, *9*(9), 3309-3319.

Wolfe, G. M., et al. (2011b), The Chemistry of Atmosphere-Forest Exchange (CAFE) Model - Part 2: Application to BEARPEX-2007 observations, *Atmos. Chem. Phys.*, *11*(3), 1269-1294.

Yeh, G. K., and P. J. Ziemann (2014), Alkyl nitrate formation from the reactions of C-8-C-14 n-alkanes with OH radicals in the presence of NOx: Measured yields with essential corrections for gas-wall partitioning, *J. Phys. Chem. A*, *118*(37), 8147-8157.

Yu, J. Z., and H. E. Jeffries (1997), Atmospheric photooxidation of alkylbenzenes .2. Evidence of formation of epoxide intermediates, *Atmos. Environ.*, *31*(15), 2281-2287.

Zhang, Q., et al. (2007), Ubiquity and dominance of oxygenated species in organic aerosols in anthropogenically-influenced Northern Hemisphere midlatitudes, *Geophys. Res. Lett.*, *34*(13), L13801.

Zhang, X., C. D. Cappa, S. H. Jathar, R. C. McVay, J. J. Ensberg, M. J. Kleeman, and J. H. Seinfeld (2014), Influence of vapor wall loss in laboratory chambers on yields of secondary organic aerosol, *Proc. Natl. Acad. Sci. U. S. A.*, *111*(16), 5802-5807.

Ziemann, P. J., and R. Atkinson (2012), Kinetics, products, and mechanisms of secondary organic aerosol formation, *Chem. Soc. Rev.*, *41*(19), 6582-6605.

# Chapter 4. ISOTHERMAL EVAPORATION OF A-PINENE OZONOLYSIS SOA: VOLATILITY, PHASE STATE, AND OLIGOMERIC COMPOSITION[3]

Abstract

We present measurements of the isothermal evaporation of α-pinene ozonolysis secondary organic aerosol (SOA). Using a novel, filter-based method, we reproduce literature observations of the time-dependent evaporation of SOA particles. We apply two detailed physical models to interpret the evaporative behavior of both the bulk SOA and individual components. Both models find that a combination of effectively non-volatile products, together with reversibly formed oligomers (or otherwise reactive monomers) having a decomposition lifetime of 9 to 28 hours, best explains the evolution of composition and volatility as particles age in the absence of both organic vapors and oxidants, even under an assumption of relatively viscous (soft wax-like with a minimum diffusion coefficient of $1 \times 10^{-15}$ $cm^2$ $s^{-1}$) particles. We find that the residence time in the SOA formation chamber, and time spent undergoing isothermal evaporation, both indicative of the physical age of the aerosol, are the most important experimental parameter determining the evaporation rate. The evolution of volatility observed in these experiments is compared to field measurements in a boreal forest site. The ambient monoterpene-dominated SOA volatility is only reproduced in the laboratory after 24 hours of extended aging in a dilute, dark, oxidant-free environment.

---

[3] Reprinted with permission from: D'Ambro, E. L., Schobesberger, S., Zaveri, R. A., Shilling, J. E., Lee, B. H., Lopez-Hilfiker, F. D., Mohr, C., and Thornton, J. A.: Isothermal Evaporation of α-Pinene Ozonolysis SOA: Volatility, Phase State, and Oligomeric Composition, ACS Earth and Space Chemistry, 10, 1058-1067, doi: 10.1021/acsearthspacechem.8b00084, 2018

## 4.1 INTRODUCTION

Atmospheric aerosol particles, particularly those less than 1 μm in diameter, have important implications for human health and visibility, and have an uncertain net effect on climate [*Poschl*, 2005]. Organic material composes a large portion (20-90%) of submicron aerosols [*Jimenez et al.*, 2009; *Zhang et al.*, 2007], with a majority of this material arising from the atmospheric processing of gas-phase volatile organic compound (VOC) emissions from biogenic sources [*Hallquist et al.*, 2009] to lower volatility material, forming secondary organic aerosol (SOA). Monoterpenes (isomers of $C_{10}H_{16}$) are a major biogenic VOC component, capable of efficiently forming SOA especially in coniferous forests, with α-pinene having the highest emission rate globally [*Guenther et al.*, 2012].

Reaction of α-pinene with ozone ($O_3$) represents approximately half of the fate of α-pinene emissions, and produces SOA with approximately a 10% or even higher mass yield [*Ng et al.*, 2006; *Pathak et al.*, 2007; *Shilling et al.*, 2008]. However, the oxidation products and chemical mechanisms driving the SOA formation, as well as the physical properties of the resulting SOA such as the bulk volatility and phase state, remain uncertain [*Shrivastava et al.*, 2017]. SOA volatility has been of particular interest due to its implications for the SOA lifetime against dilution and transport. Furthermore, to accurately model SOA growth and evolution over the full aerosol life cycle requires describing the extent to which the SOA volatility is determined by the prompt formation of low and extremely low volatility gas-phase oxidation products [*Ehn et al.*, 2014; *Tröstl et al.*, 2016], and by continued particle-phase chemistry [*Krapf et al.*, 2016].

Various approaches have been employed to study the effective volatility of α-pinene ozonolysis SOA, such as isothermal dilution of freshly formed SOA and vapors [*Grieshop et al.*, 2007; *Vaden et al.*, 2011; *Wilson et al.*, 2015], evaporation by passing SOA through thermal denuders [*Cappa and Wilson*, 2011; *Kolesar et al.*, 2015a; *Kolesar et al.*, 2015b; *Kostenidou et al.*, 2009; *Saleh et al.*, 2013], evaporation by in-chamber heating after SOA formation [*Saleh et al.*, 2013; *Stanier et al.*, 2007], and coupled heating and dilution of the SOA [*Kolesar et al.*, 2015b; *Loza et al.*, 2013]. Although often operating under different concentration and thermal regimes, these previous studies generally find that α-pinene ozonolysis SOA does not evaporate as a semi-volatile mixture, but rather as a mostly low volatility material and/or as having physical resistance to evaporation. Explanations have ranged from reversibly formed oligomers formed from semi-volatile monomers [*Kolesar et al.*, 2015a; *Kolesar et al.*, 2015b; *Saleh et al.*, 2013; *Trump and Donahue*, 2014], to particle-phase diffusion limitations resulting from highly viscous SOA [*Cappa and Wilson*, 2011; *Loza et al.*, 2013; *Stanier et al.*, 2007; *Vaden et al.*, 2011; *Wilson et al.*, 2015]. Disentangling oligomers and viscosity is difficult in that high oligomer content tends to lead to high viscosity [*Huang et al.*, 2018; *Koop et al.*, 2011]. While oligomers have been measured in α-pinene ozonolysis SOA [*Gao et al.*, 2004], some fraction of large molecular weight compounds present in SOA may actually arise from gas-phase chemistry [*Ehn et al.*, 2014; *Mohr et al.*, 2017]. Moreover, some studies of α-pinene SOA viscosity have reported essentially no mass transfer limitations, especially at elevated relative humidity [*Renbaum-Wolff et al.*, 2013].

There are several reasons for a lack of consensus on the causes of this SOA response to dilution or heating. First, the SOA formation conditions have often differed significantly, both from the

atmosphere and across the various chambers and flow tubes used. These conditions influence the relative importance of particle-phase accretion chemistry to varying degrees. Second, the discovery of very low and extremely low volatility organic compounds produced promptly in the gas-phase from α-pinene ozonolysis, and reaction with OH, by peroxy radical autoxidation requires the reinterpretation of the inferred volatility distributions from previous experiments. Up to half of the SOA may originate from very low volatility compounds produced from gas-phase chemistry alone [*Ehn et al.*, 2014; *Mohr et al.*, 2017]. Third, studies of SOA composition in several previous evaporation studies used thermal denuders [*Cappa and Wilson*, 2011; *Kalberer et al.*, 2004; *Kolesar et al.*, 2015a; *Kostenidou et al.*, 2009] which may lead to thermal decomposition of oligomers [*Lopez-Hilfiker et al.*, 2014; *Lopez-Hilfiker et al.*, 2016b], while studies of isothermal evaporation upon dilution have largely focused on bulk elemental mass or size changes [*Saleh et al.*, 2013; *Vaden et al.*, 2011; *Wilson et al.*, 2015]. If oligomerization or other particle-phase reactions were a controlling factor of the evaporation rate, the composition and volatility after hours of evaporation should be measurably different than before.

In this work, we seek to answer the following question: do compounds remain in the particle-phase after evaporation because *(i)* their saturation vapor concentration (c*, μg $m^{-3}$) is low enough, *(ii)* there is a barrier to evaporation, for example high viscosity or a coating, and/or *(iii)* they are (part of) an oligomeric network? We present measurements of the isothermal evaporation of α-pinene ozonolysis SOA formed in two different environmental chambers at atmospherically relevant precursor concentrations in order to address this question. The overarching goal is to provide insight into how the SOA is formed and evolves over the extended time frames rarely probed in chambers. Distinguishing the roles of low volatility vapor

condensation from subsequent particle-phase processes that form larger oligomers allows for a better understanding of SOA behavior over its atmospheric lifetime.

## 4.2 METHODS

### 4.2.1 *Chamber & Instrument Operation*

Experiments were performed in both the Pacific Northwest National Laboratory (PNNL) and the University of Washington (UW) environmental chambers, operated in continuous flow mode. The PNNL chamber, described previously [*D'Ambro et al.*, 2017b; *Liu et al.*, 2012], is 10.6 $m^3$ with a total flow of 25 L $min^{-1}$ resulting in a residence time of 7 hours, humidified to 50% relative humidity (RH). The input α-pinene concentration, i.e. that which would exist in the chamber absent any chemistry, was 10 ppb, and the steady-state ozone concentration was 100 ppb, generating ~4 μg $m^{-3}$ SOA (assuming 1 g $cm^{-3}$ density) with a mass weighted mean diameter of ~180 nm. Solid 50 nm $K_2SO_4$ seed, which does not deliquesce below 85% RH, was added to facilitate SOA formation. Experiments were also conducted using the UW chamber, described previously [*Lopez-Hilfiker et al.*, 2014], in both 2015 and 2017. The chamber is 0.7 $m^3$ with a specific total flow depending upon experiment of either 15 or 20 L $min^{-1}$, with no humidification (< 10% RH), resulting in residence times of 45 or 35 min, respectively. α-Pinene was introduced into the chamber by continuously flowing 100 sccm of Ultra-High Purity (UHP) $N_2$ through a diffusion source containing pure α-pinene submerged in methanol cooled to approximately -40 $^oC$. This approach produced a concentration of ~100 or 70 ppb α-pinene at steady-state depending upon the total flow. Ozone was generated by passing 5-7 sccm of ultra-zero air though a UV photolysis cell, and the concentration was adjusted until the desired steady-state SOA loading was achieved. SOA in the UW chamber was either ~6 or 30 μg $m^{-3}$ (assuming

1 g $cm^{-3}$ density) with a mass weighted mean diameter of ~250 or 350 nm, and no seed was added. In both chambers, particle size distributions were continuously monitored with a scanning mobility particle sizer (SMPS).

A high-resolution time-of-flight chemical ionization mass spectrometer (HRToF-CIMS) utilizing iodide-adduct ionization[*Lee et al.*, 2014] coupled to a Filter Inlet for Gases and AEROsols (FIGAERO) [*Lopez-Hilfiker et al.*, 2014] was configured and operated exactly as described previously [*D'Ambro et al.*, 2017a; *D'Ambro et al.*, 2017b; *J M Liu et al.*, 2016]. See the SI for a brief description. The coupling of a FIGAERO and an iodide HRToF-CIMS, from here on FIGAERO-CIMS, allowed for the measurement of oxidized products in the gas- and particle-phases.

### 4.2.2 *Isothermal Evaporations*

We focus here on the isothermal evaporation of α-pinene ozonolysis SOA at room temperature for time periods ranging from minutes to hours conducted as follows. Aerosol particles are collected in the FIGAERO normally, and the filter is actuated underneath the heating tube after a specified collection period. During a normal thermal desorption (see SI for brief description), the programmatic heating routine starts immediately, but in the isothermal evaporations, the UHP $N_2$ is first humidified to ~20, 50, or 80% RH via a bubbler system and then passed over the filter and into the HRToF-CIMS at room temperature for a pre-determined amount of time, typically 1, 3, 6, and 24 hours. The air surrounding the aerosols is thus continuously diluted, allowing for the evaporation of compounds from the SOA. After the humidified isothermal evaporation period, dry UHP $N_2$ is programmatically heated as in normal operation to conduct a thermal desorption

of the remaining SOA. Thus, the setup is such that the chemical composition of the evaporate and of the remaining SOA, is measured by the HRToF-CIMS. See Figure S1 for a schematic comparing the normal (Fig. S1a) versus isothermal evaporation (Fig. S1b) operation modes.

Instrument blanks were periodically performed by placing an additional filter, identical to that used for aerosol collection and desorption, upstream of the FIGAERO as described in Lopez-Hilfiker et al.[2014], while the collection, evaporation, and desorption steps were otherwise carried out normally. These blanks were especially important for assessing signals measured during the evaporation period when semi-volatile gases adsorbed to internal surfaces of the FIGAERO can contribute significantly to the overall signal. The particle-phase signals from thermal desorptions were generally well above blanks throughout the entire set of experiments (see Fig. S2 for an example).

Figure 4.1 Schematic of isothermal evaporation experiments. Top: relative humidity, N2 flow, and temperature of heating tube. Bottom: C10H16O5I-, a representative compound with strong signal in both the gas- and particle-phases. Shaded regions denote the phases of the experiment: simultaneous real-time gas-phase sampling (shown) and offline aerosol collection (blue), isothermal evaporation where compounds are measured as they evaporate off the filter (yellow), temperature programmed thermal desorption (green), and cool down of heating tube (gray). shows an example molecular ion signal time series and associated instrumental diagnostics measured during the evaporation process in the PNNL chamber. In the top panel, the RH, UHP $N_2$ flow through the heating tube, and measured temperature of the heating tube are displayed as a function of time. The bottom panel shows a representative compound ($C_{10}H_{16}O_5I^-$) as a

function of time. The blue shaded region is the particle collection and real-time gas-phase measurement. The yellow shaded region is when humidified UHP $N_2$ is carried over the filter and into the instrument. A clear signal can be seen for this compound evaporating at room temperature as the aerosol is diluted with humidified UHP $N_2$, implying evaporation from the particles on the filter. During the green shaded period, a normal thermal desorption occurs to drive the remaining aerosol mass off the filter, followed by a 10 min cool-down period (gray) before the process is started again. Measured signal during the heating period represents a thermogram. The integral of the thermogram is proportional to the mass of that compound (or compounds) on the filter prior to heating. Each evaporation experiment is bookended with a normal desorption to account for drifts in chamber SOA mass concentrations in the chambers or instrument response.

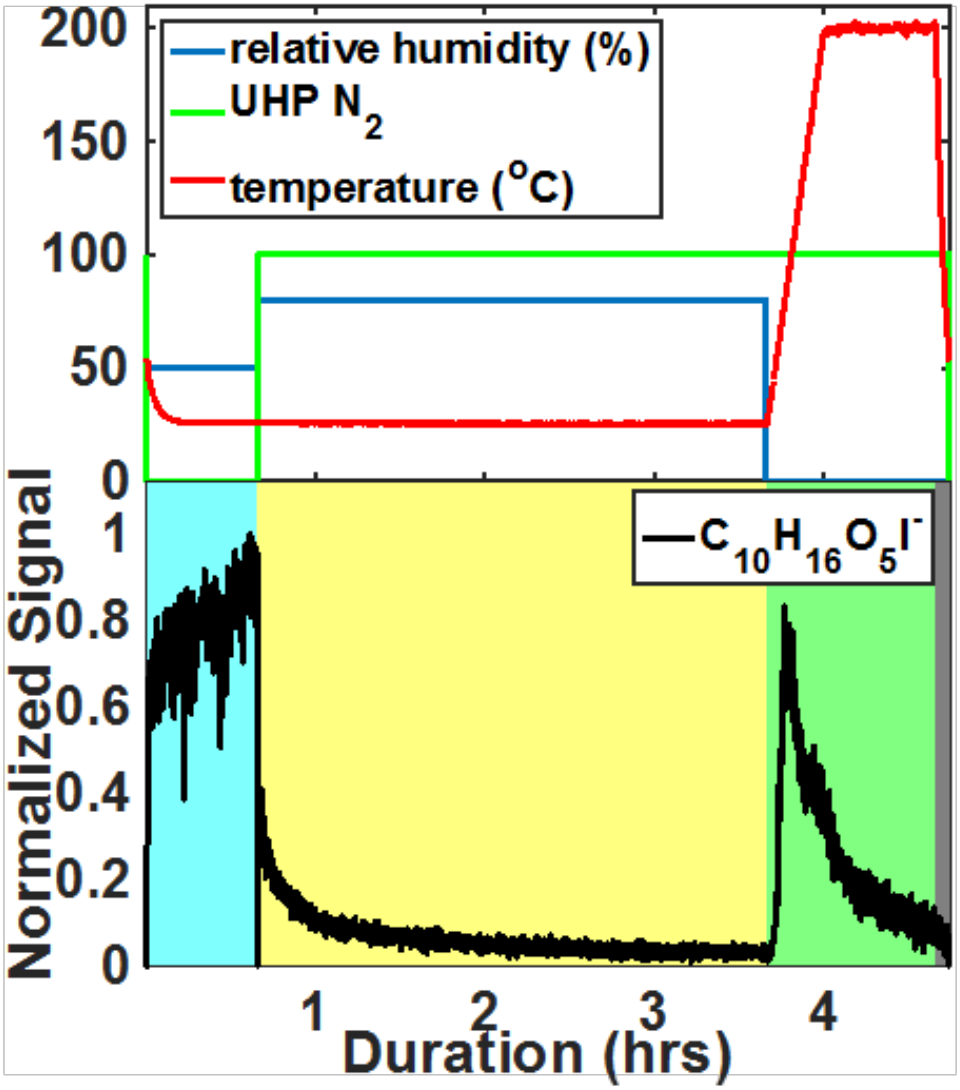


Figure 4.1 Schematic of isothermal evaporation experiments. Top: relative humidity, $N_2$ flow, and temperature of heating tube. Bottom: $C_{10}H_{16}O_5I$-, a representative compound with strong signal in both the gas- and particle-phases. Shaded regions denote the phases of the experiment: simultaneous real-time gas-phase sampling (shown) and offline aerosol collection (blue), isothermal evaporation where compounds are measured as they evaporate off the filter (yellow), temperature programmed thermal desorption (green), and cool down of heating tube (gray).

### 4.2.3 *Modeling*

Two models were applied to interpret the contribution of volatility, viscosity, and particle-phase chemistry to the observed evaporation rates. Both models use compound-specific volatility (c*), gas-phase diffusivity ($D_g$), mass accommodation (α), and temperature-dependent reversible oligomerization with forward ($k_f$) and reverse ($k_r$) rate constants to simulate the evaporation of multiple compounds. Herein, we refer to reversible oligomers as compounds that will decompose with heat or time into monomeric components that can then directly evaporate. Both models assume the organic medium of the particles is initially well-mixed. One model, described previously [*Schobesberger et al.*, 2018], is a detailed representation of evaporation and mass transfer developed for the FIGAERO, accounting for partitioning of desorbing vapors to filter and instrument wall materials. See the SI for further details and Figure S3 for a schematic of the simulated processes. To more explicitly explore the role of particle diffusion limitations due to viscous particles, we also employed a multi-layer particle model, described previously [*Zaveri et al.*, 2014; *Zaveri et al.*, 2018]. Together with the above parameters and an assumed intraparticle bulk diffusivity ($D_b$), evaporation is calculated from a single spherical particle divided into 200 layers. As one model explicitly accounts for instrumental transport limitations and the other explicitly accounts for particle diffusion limitations, the two models provide complementary and comprehensive assessment of possible processes affecting interpretation of the evaporation experiments.

## 4.3 Results & Discussion

The evaporative behavior of compounds can be visualized via the signal fraction remaining (SFR) as a function of evaporation time. The SFR is the integrated thermogram signal (see

methods) obtained after an isothermal evaporation period (i.e. the area under the curve in the green section, Figure 4.1 Schematic of isothermal evaporation experiments. Top: relative humidity, N2 flow, and temperature of heating tube. Bottom: C10H16O5I-, a representative compound with strong signal in both the gas- and particle-phases. Shaded regions denote the phases of the experiment: simultaneous real-time gas-phase sampling (shown) and offline aerosol collection (blue), isothermal evaporation where compounds are measured as they evaporate off the filter (yellow), temperature programmed thermal desorption (green), and cool down of heating tube (gray)., bottom), referenced to the integrated thermal desorption signal obtained without an isothermal evaporation period. While the Iodide CIMS does not have the same sensitivity for each oxidized product, it does converge to a similar limiting value for highly functionalized compounds [*Lopez-Hilfiker et al.*, 2016a]. Additionally, we have shown that a conservative lower-limit estimate of mass detected by the Iodide CIMS can explain ~50% of SOA as measured by an AMS (see e.g., Lopez-Hilfiker et al. [2016b] and Liu et al. [2016] Therefore, the SFR is analogous (and directly proportional) to the volume (or mass) fraction remaining reported previously [*Cappa and Wilson*, 2011; *Grieshop et al.*, 2007; *Kolesar et al.*, 2015a; *Kolesar et al.*, 2015b; *Kostenidou et al.*, 2009; *Trump and Donahue*, 2014; *Vaden et al.*, 2011; *Wilson et al.*, 2015].

### 4.3.1 *Behavior of Bulk SOA*

To maintain proportionality with volume and mass fraction remaining as discussed above, the evaporative behavior of the bulk SOA is described by the carbon-weighted SFR (Figure 4.2, top, blue and red symbols) where the SFR for each compound detected as a cluster with Iodide ions ($C_xH_yO_zI$-) is normalized by the corresponding carbon number, and then summed. Normalization

by molecular weight achieves a similar result. To within the experimental precision of our method, the bulk SFR versus isothermal evaporation time for SOA generated in the UW chamber (Figure 4.2, top, triangles) is essentially identical to the volume fraction remaining presented by Vaden et al. [2011], despite the substantially different experimental techniques used to study evaporation. In the work of Vaden et al. [2011], aerosol is formed in one chamber, passed through a DMA and two charcoal denuders, and allowed to evaporate in a second stainless steel chamber partially filled with activated charcoal to strip away the vapor phase. The signal for all 5 experiments decays in two distinct stages: a rapid loss of ~40-50% of SOA in the first 1 to 6 hours, followed by a much slower loss of the remaining SOA over the subsequent ~20 hours. After 24 hours of evaporation, 25-48% of carbon-weighted signal is remaining. The two different UW chamber experiments were conducted over two different years with similar chamber residence times, but with different evaporation RH and a factor of 5 different mean OA concentrations in the chamber. That these two experiments lead to such similar evaporative behaviors suggests that OA concentrations and RH play a limited role during evaporation, at least when OA < 30 μg $m^{-3}$, and RH >50%.

The evaporative behavior of SOA formed in the PNNL chamber is notably different from that formed in the UW chamber (Figure 4.2, top, circles). The PNNL chamber SOA shows a shallower decrease, particularly in the early stages of evaporation, such that 42-47% of signal remains after 24 hours. While different from the UW chamber SOA, even when the total OA load was similar (5 vs. 6 μg $m^{-3}$), the PNNL SOA behavior more closely resembles that shown by Wilson et al.[2015]. While SOA molecular composition was slightly different between the two chambers (e.g. O:C of 0.66 at PNNL vs. 0.62 at UW), the bulk composition differences

alone were not substantial enough to explain the significantly different evaporation rates (Fig. S4).

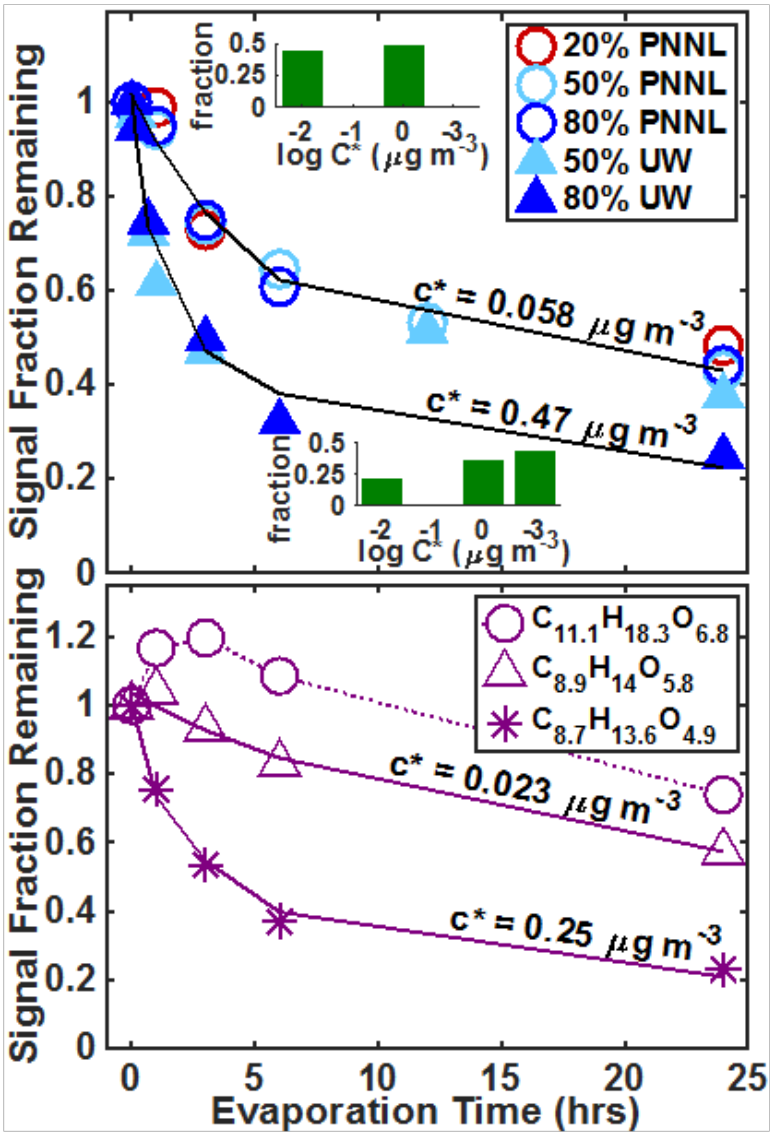


Figure 4.2 *Top*: Signal fraction remaining as a function of evaporation time for the bulk SOA for all five experiments. The 80% RH experiments in each chamber were fit with a simple c*-based evaporation model (black lines) with the resulting calculated c* labeled. *Top, inset:* the volatility basis sets generated from the c*-based model fits. *Bottom*: Signal fraction remaining as a function of evaporation time for compositions binned by their initial slope (purple symbols) and their signal weighted composition. The two monotonically decreasing bins were fit with the

simple c*-based model (solid lines) and the calculated c*'s are displayed. The bin with the largest molecular weight was not fit (dotted line) due to its non-monotonic behavior.

Comparing across our data sets, we attribute the differences between the UW and PNNL chamber SOA behaviors to the difference in chamber residence times (45min versus 7 hours, respectively). Wilson et al. [2015] showed that SOA that has been physically aged has a much slower evaporation rate, particularly in the early stages (≤ 2 hours), than its unaged equivalent. The SOA formed in the PNNL chamber has aged by about 6 hours longer than that formed in the UW chamber due to the much longer residence time. After 24 hours of evaporation however, the differences in SFR between the two chambers diminishes as the time spent aging in UHP $N_2$ on the filter becomes much larger than the difference in chamber residence times. Thus, we conclude the age of the SOA at the time of dilution plays a significant role in setting the early evaporation behavior. We note that the aging here involves mostly non-photochemical aging, given that the only source of radical oxidants is the relatively small amount of OH resulting from ozonolysis [*Donahue et al.*, 1998], as well as vapor-wall interactions. An MCM-based model [*Wolfe et al.*, 2016] predicts ~$7.4\times10^5$ and ~5.0-5.9 $\times10^6$ molec $cm^{-3}$ of OH in the PNNL and UW chambers, respectively.

Regardless of the chamber and RH used for SOA formation, we observe only a weak dependence of the evaporation rate on the RH experienced during evaporation. This finding is contrary to what previous studies have shown [*Wilson et al.*, 2015] and measures of particle viscosity would suggest [*Renbaum-Wolff et al.*, 2013]. Wilson et al. [2015] formed and evaporated their SOA at the same RH, while we formed SOA at one RH, either < 10% (UW chamber) or 50% (PNNL

chamber), and then conducted isothermal evaporations at different RH, either 20%, 50%, or 80% RH. Renbaum-Wolff et al. [2013] were examining 20-50 μm particles reconstituted by extracting SOA collected on a filter several days prior to the extraction and found that viscosity decreased at high RH. Our findings are consistent with two previous works in which SOA was formed at a lower RH and the SVOC uptake to that SOA showed no evidence for diffusion limitations at a higher RH[*Ye et al.*, 2016], or evaporation rates from thin films of the SOA were measured to be similar at high RH [*P F Liu et al.*, 2016]. It is possible that the SOA from these previous experiments and the SOA presented herein is unable to take up enough water at 50% RH or even up to 80 or 90% RH to substantially affect the observed evaporation timescales. We did not however probe evaporation at RH < 20%, where previous studies have shown there may be a difference in evaporation rate [*Wilson et al.*, 2015; *Yli-Juuti et al.*, 2017]. The role of viscosity differences is further examined below.

### 4.3.2 *Behavior of Molecular Components*

While similar molecular compositions are measured throughout each evaporation experiment and most detected compositions decrease with evaporation time, the relative contributions of these compositions to the remaining SOA do change with evaporation time. We normalize the integrated thermogram signals of each composition to that for $C_9H_{14}O_4$, a major component of the particle-phase (Fig. S5). The changes in relative contributions of any given compound to the internal comparison standard is of order a factor of 0.5 after 24 hours of evaporation, although in some cases the relative changes are factors of 2 or more. These relative changes imply that the mass fractions of different components are changing by different rates throughout the evaporation period. This observation can be explained in part, but not solely, by c*-based

evaporation. Several compositions both at lower and higher molecular weights increase with evaporation time regardless of the choice of internal comparison standard. See the following section for further discussion.

That the spectrum-wide average composition changes are relatively modest indicate that the source of many desorbing SOA components is similar regardless of whether the compounds desorb due to isothermal evaporation or by heating-induced thermal decomposition. That is, low volatility/oligomeric material must be decomposing in a similar way with both time and temperature to give rise to the similar set of detected molecular ions. This interpretation is largely consistent with the findings of constant composition by Cappa and Wilson [2011] which they attributed to a layer-by-layer evaporation in a thermal denuder. However, as noted above and shown in Figure S5, we do observe detectable changes in relative composition, in some cases by more than factors of 2, throughout the course of the room-temperature aging on the filter. Furthermore, we show below that our results can be explained without invoking a layer-by-layer evaporation model, but rather a network of weakly bound low volatility components. However, it is difficult to rule out a scenario where a small fraction of the compositions, of order 10% or less, is contained within a core, while the vast majority is in a well-mixed shell.

### 4.3.3 *Controls on the Evaporation Rate*

Each individual molecular component within the bulk SOA may have a unique rate of decay of SFR during the evaporation period (see, e.g., Fig. S6). Therefore, we determined the slope of initial decay, during the first 6 hours, in SFR for each of the 312 detected molecular ions. These slopes were then used to bin the detected molecular ion signals into three groups based on the

histogram of the calculated slopes (Fig. S7). The signal-weighted carbon, hydrogen, and oxygen numbers were averaged for each bin as a function of evaporation time to calculate the average composition (Figure 4.2, bottom panel, purple symbols). This and all further figures in the main text and SI show the 80% RH experiment at PNNL for simplicity unless otherwise stated. The decay rates of the two monotonically decreasing bins follow a logical pattern: the lower the carbon and oxygen numbers, the steeper the slope and thus the faster the evaporation rate, broadly consistent with a composition-based volatility framework. The third bin which corresponds to large molecular weight components evaporates slowest, and even increases in abundance during the first portion of the evaporation, consistent with accretion chemistry.

To begin interpreting these evaporation rates, we first apply a simple model of evaporation driven by c* (see SI for description) to each of the binned SFR curves. Assuming each bin is composed of at least three hypothetical components having different c* allows the model to replicate the evaporation behavior of the two bins with monotonically decreasing SFR (Figure 4.2, bottom, purple lines). The resulting c* distributions and signal weighted mean c* (0.023 and 0.25 μg $m^{-3}$) for these two bins are reasonable in that the mean c* is highest for the bin with a lower average carbon and oxygen number composition. Not surprisingly, the model is unable to reproduce the behavior of the third bin having an initial increase in SFR given that the model does not include a process for mass growth, only mass loss. The SOA evaporation behavior summed across all signals at 80% RH, for SOA formed in both the UW and PNNL chambers, can also be modeled by distributing the signal across components with varying pre-defined c*'s (Figure 4.2 top, black lines, and inset volatility basis set plots), resulting in bulk c*'s of 0.47 and 0.013 μg $m^{-3}$, respectively. These bulk c* values represents the overall observed c* of the SOA

as a whole. Although these simple volatility-based frameworks can explain the evaporation behavior of the bulk OA, it is unable to reproduce the molecular-level behaviors where volatility bins cannot be arbitrarily constructed and populated.

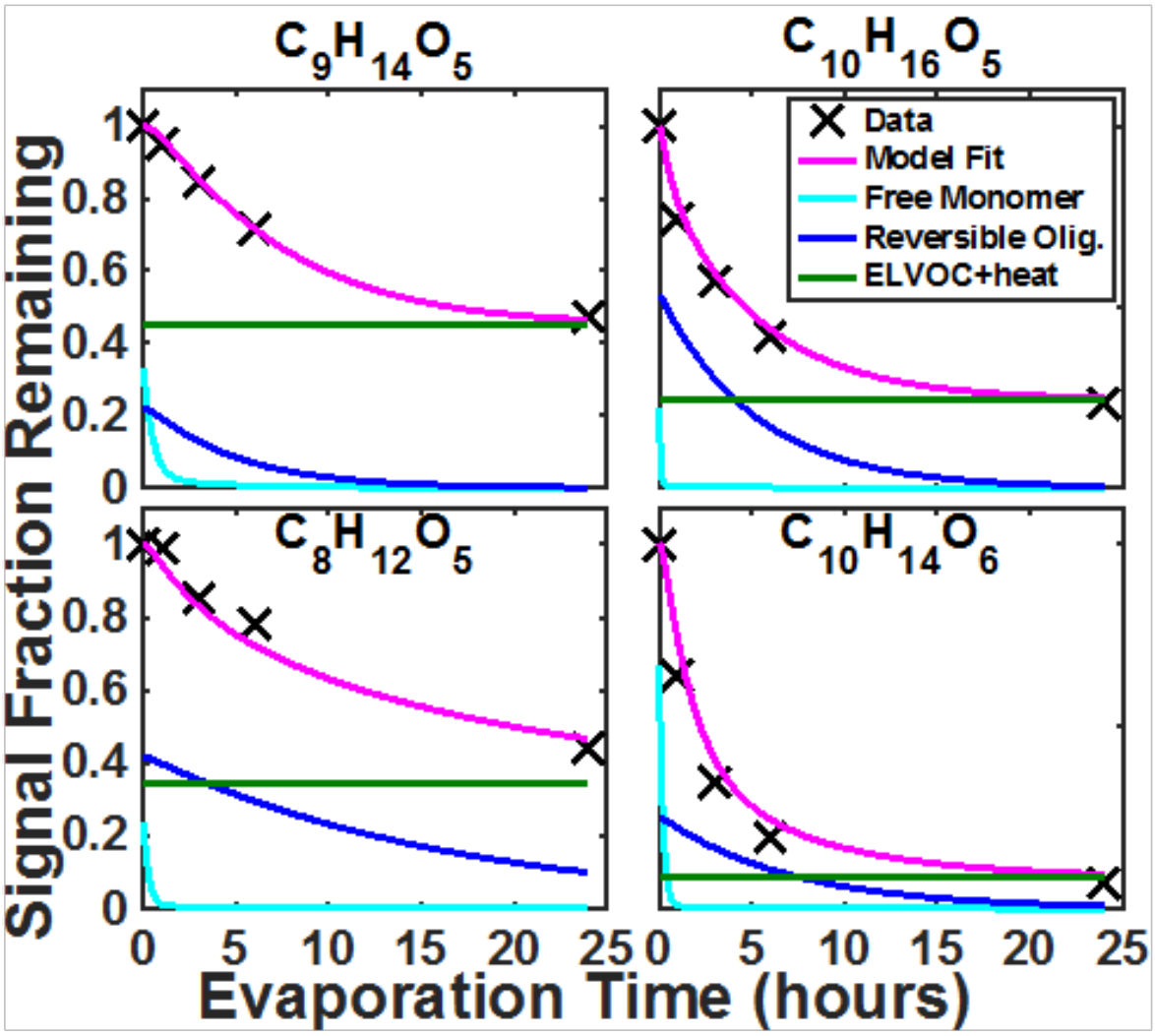


Figure 4.3 Results of the FIGAERO model for the signal fraction remaining for four compounds with similar O:C yet a relatively slow evaporation rate (*left column*) versus a relatively fast evaporation rate (*right column*). The model achieves the fits by distributing the signal across 3 components: free monomer, reversible oligomer, and thermal decomposition.

We therefore apply more comprehensive models to these isothermal evaporation experiments. Figure 4.3 shows model predictions for four major particle-phase compounds at 80% RH evaporation in the PNNL chamber that together explain 26% of the SOA signal detected, and that, despite having similar compositions, have different decay rates during isothermal evaporation: top left) $C_9H_{14}O_5$ and bottom left) $C_8H_{12}O_5$ with relatively slow decays; and top right) $C_{10}H_{16}O_5$ and bottom right) $C_{10}H_{14}O_6$ with relatively fast decays. These model fits assume there are no particle-phase diffusion limitations, but do account for mass transfer limitations through the FIGAERO filter. The model accurately replicates the observed decays of each compound during the isothermal evaporation periods only if a significant fraction of each is initially part of a reversible "oligomer" (22-53%), and if also produced from thermal decomposition of effectively non-volatile components during the temperature-programmed thermal desorption (8-45%) (as opposed to the direct evaporation with heat of monomeric material observed with that composition). We refer to reversible oligomers as compounds that will decompose with heat or time into monomeric components that can then directly evaporate, and non-volatile components (labeled in the figure as ELVOC + heat) as species that will essentially never decompose and/or evaporate at room temperature, but which can thermally decompose into fragments when heated. The model accurately replicates the SFR of each compound, with all cases having a room-temperature first-order oligomer decomposition rate coefficient between $1.7\times10^{-5}$ and $6\times10^{-5}$ $s^{-1}$. The $C_9H_{14}O_5$ and $C_8H_{12}O_5$ require a larger fraction of reversible oligomers and non-refractory material than $C_{10}H_{16}O_5$ and $C_{10}H_{14}O_6$, which require a larger fraction of free-monomer, to explain the relative differences in their respective decay rates. The corresponding room temperature c* for "free" $C_9H_{14}O_5$, $C_8H_{12}O_5$, $C_{10}H_{16}O_5$, and $C_{10}H_{14}O_6$ in the model are 0.5, 1.2, 3.8, 1.5 μg $m^{-3}$, respectively, which are reasonably similar to

each other and close to group contribution estimates [*Capouet and Muller*, 2006; *Compernolle et al.*, 2011; *Pankow and Asher*, 2008] assuming a combination of –OOH or –OH and C=O groups. Other parameters can be found in the SI, as well as the corresponding values for the bulk SOA at 80% RH in both chambers (Table S1).

To more directly address the question of particle viscosity, a particle multi-layer model was applied to the data [*Zaveri et al.*, 2014; *Zaveri et al.*, 2018]. The model was run for two scenarios: liquid-like (top row, $D_b > 10^{-10}$ cm$^2$ s$^{-1}$) and semisolid (bottom row, $1.0 \times 10^{-15} < D_b < 1.8 \times 10^{-15}$ cm$^2$ s$^{-1}$) [*Renbaum-Wolff et al.*, 2013], i.e. no particle-phase diffusion limitations versus diffusion-limited semi-solids. See the SI for further discussion on the choice of these values. The model was able to reproduce the SFR at each RH, in each chamber, for the bulk SOA as well as two model compounds, $C_{10}H_{16}O_5$ and $C_{10}H_{14}O_6$, for either scenario (Figure 4.4, PNNL and S8, UW) without requiring significant changes to the compound-specific c*. However, regardless of the scenario, bulk SOA oligomer decomposition rates of $10^{-5}$ s$^{-1}$ in the PNNL chamber and $10^{-4}$ s$^{-1}$ in the UW chamber were required to allow the model to reproduce individual compound behavior. When reversible oligomerization is removed, the model can reproduce the bulk SOA evaporation, but not that of the individual molecular compounds (Fig. S9 and Table S4). In order to fit the individual compounds in this case, without oligomer decomposition, multiple c*'s are required for the same individual composition, or the c*'s for individual compositions must evolve in time at room temperature, ultimately spanning a range of several orders of magnitude, similar to what we found above applying the simple c*-based model (see SI for further discussion). These decomposition rate constant values are in line with previous model results that utilized isothermal evaporation measurements as their guide [*Roldin*

*et al.*, 2014; *Trump and Donahue*, 2014], but slightly slower than the rates found by models that used thermal-based methods to evaporate the SOA [*Kolesar et al.*, 2015b]. Taken together, these results suggest that the methods used to perform the evaporation may affect the results, and care should be taken to perform the experiments at atmospherically relevant conditions, particularly temperatures and OA loadings, to ensure the processes being probed are relevant.

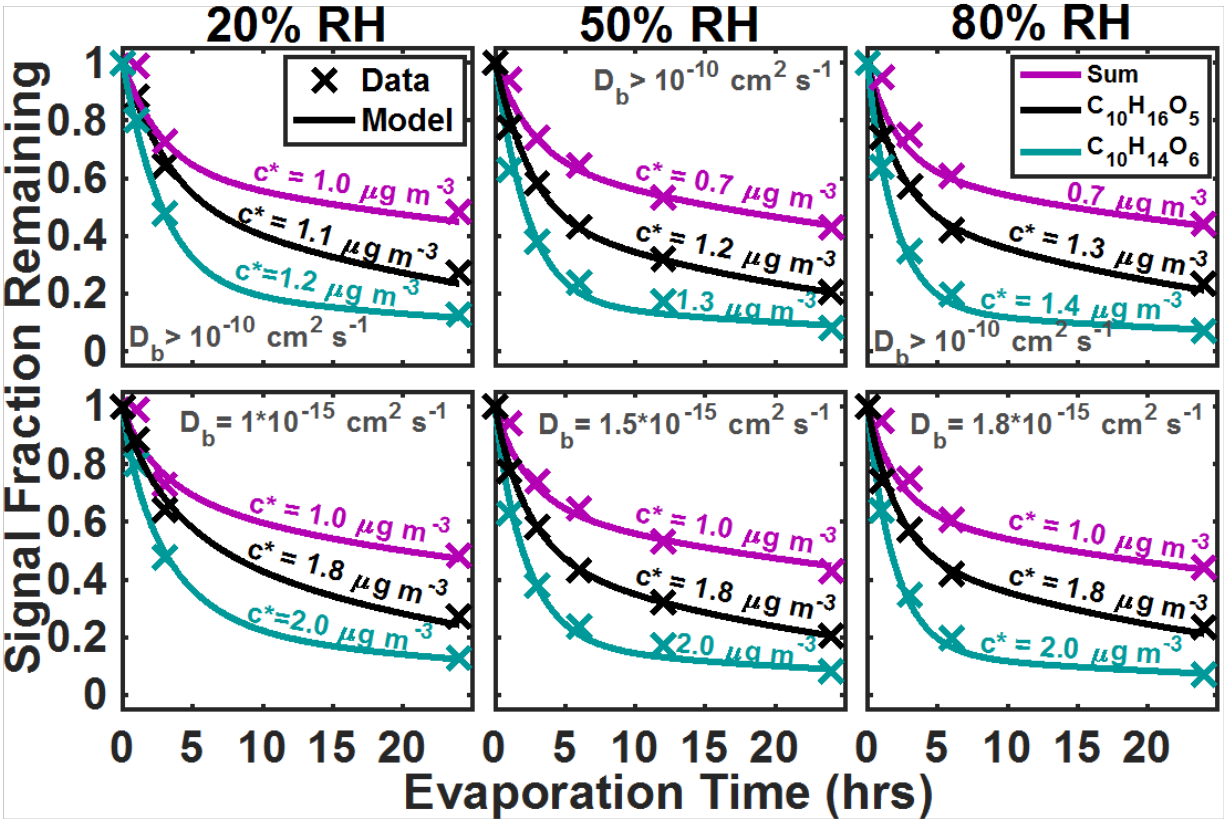


Figure 4.4 Results of the particle multi-layer model for each of the 3 evaporation RH conditions in the PNNL chamber. *Top*: liquid-like scenario, *Bottom*: semisolid scenario. The bulk diffusivity ($D_b$) and the c* for each bin are shown in gray.

These results suggest that oligomer decomposition and/or other volatility increasing chemical reactions control the early stages of evaporation upon dilution, even under a condition with moderate viscosity similar to waxy semi-solids ($1.0 \times 10^{-15} < D_b < 1.8 \times 10^{-15}$ cm$^2$ s$^{-1}$, consistent

with a viscosity of ~$10^7$ Pa s [*Renbaum-Wolff et al.*, 2013]). We note that a much higher viscosity state as the sole cause of slow evaporation can be ruled out given that the c* adjustment necessary to match the observed evaporation would be much higher than consistent with the observed compositions and SOA loading. These results further suggest that a significant fraction (~30-50%) of the aerosol undergoes such decomposition or reaction. The model simulations require similar oligomer decomposition rate constants for both the PNNL and UW chambers (Fig. S8 and Table S3). To explain the different evaporation rates between the two chambers, a higher free monomer fraction relative to oligomer fraction for each of the individual compounds is required in the shorter residence-time UW chamber, suggesting a possible accretion process occurring on that timescale that largely reaches completion on the 7 hour PNNL chamber timescale.

### 4.3.4 *Time Evolution of SOA Effective Volatility*

In addition to the relative changes in composition, we observe a substantial decrease in the effective volatility of the SOA with isothermal evaporation time as inferred via the thermogram (Figure 4.5, top) and expected. Previous studies have shown that the shape and temperature at which signal reaches a maximum during a thermogram ($T_{max}$), either for an individual component or the bulk SOA, are indicative of the chemical or physical state of the compound desorbing, and its effective volatility [*Huang et al.*, 2018; *Lopez-Hilfiker et al.*, 2014; *Lopez-Hilfiker et al.*, 2016b]. Effective volatility refers to the combined impacts of diffusion limitations and thermal decomposition of lower-volatility components.

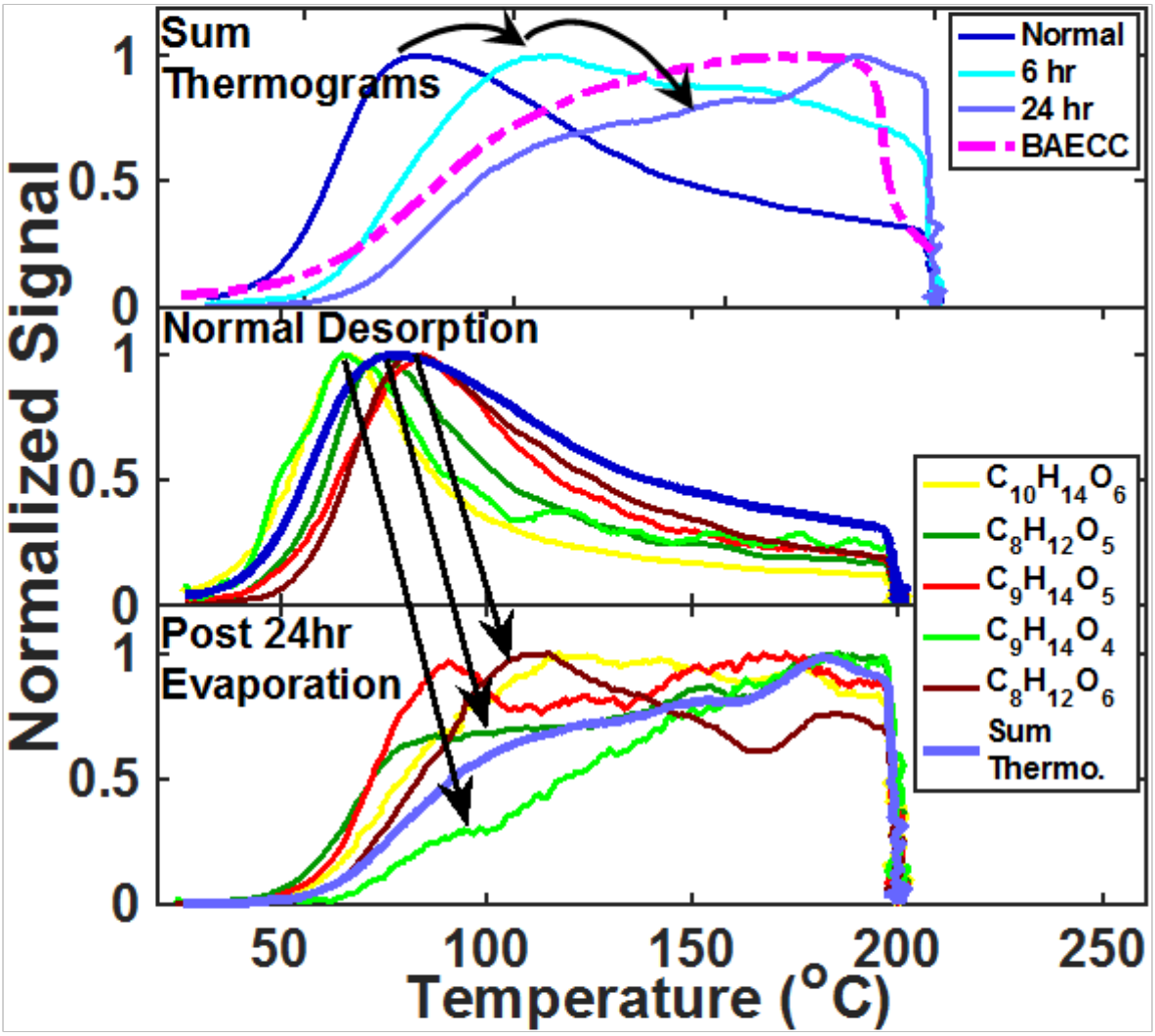


Figure 4.5 *Top*: *S*um thermograms of all $C_xH_yO_zI^-$ compounds from 80% RH PNNL experiment (blue lines) relative to data collected during BAECC (magenta dashed line) in Hyytiälä Finland, a remote boreal forest site. *Middle*: thermograms for the 7 largest signals during a normal desorption. *Bottom*: thermograms for the 7 largest signals after 24 hours of evaporation.

As a function of isothermal evaporation time, the area under the low temperature/high volatility portion of the thermogram decreases relatively rapidly, while what remains after long isothermal evaporation times is material desorbing at high temperature (see also, Fig. S10). This general

behavior is expected: higher volatility material should, by definition, evaporate fastest and what remains after such a dilution/evaporation are the lowest volatility components. Moreover, this behavior is consistent with the evaporation timescales of individual components discussed above (Figure 4.2) whereby some compounds evaporate rapidly, others more slowly, and some almost not at all.

Interestingly, the slope of the rise of total desorption signal becomes increasingly shallower, and the overall shape becomes increasingly less Gaussian (Figure 4.5, top & bottom). This behavior, thermograms shifting to shallower slopes and higher, less obvious $T_{max}$, applies not only to the bulk SOA but also to several of the major individually detected components as shown in the middle and bottom panels of Figure 4.5. The thermograms of specific SOA components during prompt desorptions, i.e., without isothermal evaporation periods, have a wide variety of thermogram shapes and $T_{max}$ (Figure 4.5, middle). However, after 24 hours of isothermal evaporation, most compounds display a similar desorption profile to that of the bulk (Figure 4.5, bottom). This behavior suggests that initially, the SOA is a mixture of distinct components having an array of volatilities, proceeding towards a more homogenous, very low volatility mixture after the evaporation of higher volatility compounds. From a calibration of $\Delta H_{vap}$, and therefore $c^*_{298K}$, with FIGAERO $T_{max}$ [*Lopez-Hilfiker et al.*, 2014], the specific compounds detected and the bulk SOA after 24 hours of isothermal evaporation have an effective $c^* < 0.001$ $\mu g\ m^{-3}$. That is, the entirety of the remaining SOA is extremely low volatility.

In an ideal, non-interacting mixture, the slope of the thermogram is controlled by the $\Delta H_{vap}$ as described by the Clausius-Clapeyron equation, which we approximate here as in Donahue et al. [2006; 2012]:

$$\ln c^*(T) \cong \ln c^*(300K) + \left[\frac{\Delta H_{vap}}{R}\left(\frac{1}{300K} - \frac{1}{T}\right)\right] \quad \text{(Eq. 4.5)}$$

For the individual components, the shallower thermogram slope observed after longer isothermal evaporation times is indicative of a lower $\Delta H_{vap}$, even though the higher $T_{max}$ is consistent with overall lower volatility (more refractive) material. Such behavior is consistent with weakly bound (e.g., non-covalent H-bonds) oligomeric networks dissociating or thermal decomposition of very low volatility compounds via scission of covalent bonds having a wide array of different bond energies [*Schobesberger et al.*, 2018]. While particle viscosity could be increasing during the evaporative aging, it is unlikely to be the dominant explanation, otherwise we would expect larger differences between the 20% and 80% RH evaporation experiments [*Wilson et al.*, 2015]. In addition, recent work shows that temperature dependent changes in viscosity are exhibited as only minor shifts in the FIGAERO thermograms, which are not consistent with the very large apparent shifts we observe [*Huang et al.*, 2018]. Moreover, substantial evaporative mass loss is obviously occurring throughout most of the isothermal dilution periods (Fig 2, top). That the higher volatility components disappear from the SOA relatively promptly (Fig. S11), while thermograms of almost all components become rather indistinct with shallow slopes and high $T_{max}$ after 24 hours of isothermal evaporation, is more consistent with a significant fraction (30-50%) of the SOA having a very low volatility but also relatively weak bonds (<85-125 kJ $mol^{-1}$) that can be broken during thermal desorption at 100-200 $^{o}$C [*Lopez-Hilfiker et al.*, 2015; *Schobesberger et al.*, 2018].

## 4.4 ATMOSPHERIC IMPLICATIONS

The results herein are compared to measurements taken at a remote boreal forest site in Hyytiälä, Finland to assess their atmospheric relevance. The chamber sum thermograms after various stages of evaporation are directly compared to the sum thermogram measured at the forest site without any evaporation period, only the 45 minute collection period (Figure 4.5, top). The laboratory chamber sum thermogram obtained after 24 hours of isothermal evaporation most closely resembles that measured in the atmosphere over the forest, suggesting that atmospheric aerosol is of very low volatility, a state which is not achieved in our typical chamber operation. Our laboratory experiments had minimal oxidative processing in the chamber, and the evaporations occurred in the dark in the absence of any external radical sources. The similarity between the chamber 24-hour evaporation thermogram and that from the forest site suggest that when designing chamber experiments, ensuring that the aerosol has enough time to age physically, not just oxidatively, is of experimental interest in order to generate SOA similar to what is observed in the ambient rural boreal forest atmosphere.

Based on results of both physical process models discussed above, the bulk α-pinene ozonolysis SOA in the PNNL chamber has an evaporating portion with an effective mass-weighted c* of ~1-4 μg $m^{-3}$ at a SOA concentration of ~5 μg $m^{-3}$, and with an oligomer lifetime against dissociation of ~21-28 hours (FIGAERO model: Fig. S12, particle multi-layer model: Figure 4.4, S8, S9). While we are not able to definitively rule out the presence of diffusion limitations, we have shown that reversible oligomers are required to explain the evaporation rate of individual compounds, even under an assumption of viscous semi-solid particles. Reproducing evaporation behaviors of individual compositions without invoking oligomer decomposition requires an array

of c*'s for each composition that span 4 to 5 orders of magnitude, or a hardening of the SOA which reduces the evaporation coefficient from 1 to $< 10^{-5}$ over the course of 24 hours. These requirements appear unphysical in some cases and inconsistent with independent measures of monoterpene SOA viscosity at high RH, respectively [*Renbaum-Wolff et al.*, 2013]. Thus, we conclude the best explanation of our results is that α-pinene ozonolysis SOA is a moderately viscous medium (even at 80% RH) with a significant fraction (~35%) being low to extremely low volatility at the time of formation, and another significant fraction being involved in reversible non-covalent interactions (~42%) among individual components strong enough to substantially reduce the effective volatility of individual components while in equilibrium with the vapor phase, leading to a dynamic system upon dilution for about 50% or more of the SOA mass.

The oligomer dissociation timescale we infer is shorter than the lifetime of boundary layer SOA against deposition. Thus, dissociation of larger molecular weight compounds, or unidentified particle-phase reactions which increase volatility, even in the absence of gas-phase radicals, could be an important loss process of SOA in the lower atmosphere downwind of net formation regions. Including these processes discussed herein, most notably the formation and decomposition of oligomeric material, in atmospheric models is likely necessary to correctly predict the amount of monoterpene SOA and its evolution downwind of net source regions. Despite our rapid and complete removal of the gas-phase, which in and of itself is not representative of atmospheric processes, the formation and dissociation rates we report are directly relevant to modeling the response of the SOA to a perturbation such as dilution or photochemical processing of gas-phase species in equilibrium with SOA components. A

reasonable approach for α-pinene SOA would be to utilize the formation and decomposition rates (Tables S1, S2, and S3), together with the mass fractions reported here, and which are similar in magnitude to those derived from the different experimental setups [*Cappa and Wilson*, 2011; *Trump and Donahue*, 2014].

## 4.5 SUPPORTING INFORMATION

The supporting information is available free of charge on the ACS publications website at DOI: 10.1021/acsearthspace-chem.8b00084. The Supporting information includes further detail on: the FIGAERO operation and each of the 3 models discussed, 4 tables with parameters of model outputs, and 13 figures supporting arguments made throughout the text. Also includes a link to the FIGAERO desorption model for download.

References

Capouet, M., and J. F. Muller (2006), A group contribution method for estimating the vapour pressures of alpha-pinene oxidation products, *Atmospheric Chemistry and Physics*, *6*, 1455-1467.

Cappa, C. D., and K. R. Wilson (2011), Evolution of organic aerosol mass spectra upon heating: implications for OA phase and partitioning behavior, *Atmospheric Chemistry and Physics*, *11*(5), 1895-1911.

Compernolle, S., K. Ceulemans, and J. F. Muller (2011), EVAPORATION: a new vapour pressure estimation method for organic molecules including non-additivity and intramolecular interactions, *Atmos. Chem. Phys.*, *11*(18), 9431-9450.

D'Ambro, E. L., K. H. Moller, F. D. Lopez-Hilfiker, S. Schobesberger, J. M. Liu, J. E. Shilling, B. Lee, H. G. Kjaergaard, and J. A. Thornton (2017a), Isomerization of Second-Generation Isoprene Peroxy Radicals: Epoxide Formation and Implications for Secondary Organic Aerosol Yields, *Environmental science & technology*, *51*(9), 4978-4987.

D'Ambro, E. L., et al. (2017b), Molecular composition and volatility of isoprene photochemical oxidation secondary organic aerosol under low- and high-NOx conditions, *Atmos. Chem. Phys.*, *17*(1), 159-174.

Donahue, N. M., J. H. Kroll, J. G. Anderson, and K. L. Demerjian (1998), Direct observation of OH production from the ozonolysis of olefins, *Geophys. Res. Lett.*, *25*(1), 59-62.

Donahue, N. M., A. L. Robinson, C. O. Stanier, and S. N. Pandis (2006), Coupled partitioning, dilution, and chemical aging of semivolatile organics, *Environmental science & technology*, *40*(8), 2635-2643.

Donahue, N. M., J. H. Kroll, S. N. Pandis, and A. L. Robinson (2012), A two-dimensional volatility basis set - Part 2: Diagnostics of organic-aerosol evolution, *Atmospheric Chemistry and Physics*, *12*(2), 615-634.

Ehn, M., et al. (2014), A large source of low-volatility secondary organic aerosol, *Nature*, *506*(7489), 476-479.

Gao, S., M. Keywood, N. L. Ng, J. Surratt, V. Varutbangkul, R. Bahreini, R. C. Flagan, and J. H. Seinfeld (2004), Low-molecular-weight and oligomeric components in secondary organic aerosol from the ozonolysis of cycloalkenes and alpha-pinene, *J. Phys. Chem. A*, *108*(46), 10147-10164.

Grieshop, A. P., N. M. Donahue, and A. L. Robinson (2007), Is the gas-particle partitioning in alpha-pinene secondary organic aerosol reversible?, *Geophys. Res. Lett.*, *34*(14).

Guenther, A. B., X. Jiang, C. L. Heald, T. Sakulyanontvittaya, T. Duhl, L. K. Emmons, and X. Wang (2012), The model of emissions of gases and aerosols from nature version 2.1 (MEGAN2.1): an extended and updated framework for modeling biogenic emissions, *Geosci. Model Dev.*, *5*(6), 1471-1492.

Hallquist, M., et al. (2009), The formation, properties and impact of secondary organic aerosol: current and emerging issues, *Atmospheric Chemistry and Physics*, *9*(14), 5155-5236.

Huang, W., H. Saathoff, A. Pajunoja, X. L. Shen, K. H. Naumann, R. Wagner, A. Virtanen, T. Leisner, and C. Mohr (2018), alpha-Pinene secondary organic aerosol at low temperature: chemical composition and implications for particle viscosity, *Atmospheric Chemistry and Physics*, *18*(4), 2883-2898.

Jimenez, J. L., et al. (2009), Evolution of organic aerosols in the atmosphere, *Science*, *326*(5959), 1525-1529.

Kalberer, M., et al. (2004), Identification of polymers as major components of atmospheric organic aerosols, *Science*, *303*(5664), 1659-1662.

Kolesar, K. R., Z. Y. Li, K. R. Wilson, and C. D. Cappa (2015a), Heating-Induced Evaporation of Nine Different Secondary Organic Aerosol Types, *Environmental science & technology*, *49*(20), 12242-12252.

Kolesar, K. R., C. Chen, D. Johnson, and C. D. Cappa (2015b), The influences of mass loading and rapid dilution of secondary organic aerosol on particle volatility, *Atmospheric Chemistry and Physics*, *15*(16), 9327-9343.

Koop, T., J. Bookhold, M. Shiraiwa, and U. Poschl (2011), Glass transition and phase state of organic compounds: dependency on molecular properties and implications for secondary organic aerosols in the atmosphere, *Phys. Chem. Chem. Phys.*, *13*(43), 19238-19255.

Kostenidou, E., B. H. Lee, G. J. Engelhart, J. R. Pierce, and S. N. Pandis (2009), Mass Spectra Deconvolution of Low, Medium, and High Volatility Biogenic Secondary Organic Aerosol, *Environmental science & technology*, *43*(13), 4884-4889.

Krapf, M., I. El Haddad, E. A. Bruns, U. Molteni, K. R. Daellenbach, A. S. H. Prevot, U. Baltensperger, and J. Dommen (2016), Labile Peroxides in Secondary Organic Aerosol, *Chem*, *1*(4), 603-616.

Lee, B. H., F. D. Lopez-Hilfiker, C. Mohr, T. Kurten, D. R. Worsnop, and J. A. Thornton (2014), An iodide-adduct high-resolution time-of-flight chemical-ionization mass spectrometer: application to atmospheric inorganic and organic compounds, *Environ. Sci. Technol.*, *48*(11), 6309-6317.

Liu, J. M., et al. (2016), Efficient isoprene secondary organic aerosol formation from a non-IEPOX pathway, *Environ. Sci. Technol.*, *50*(18), 9872-9880.

Liu, P. F., Y. J. Li, Y. Wang, M. K. Gilles, R. A. Zaveri, A. K. Bertram, and S. T. Martin (2016), Lability of secondary organic particulate matter, *Proc. Natl. Acad. Sci. U. S. A.*, *113*(45), 12643-12648.

Liu, S., J. E. Shilling, C. Song, N. Hiranuma, R. A. Zaveri, and L. M. Russell (2012), Hydrolysis of organonitrate functional groups in aerosol particles, *Aerosol Sci. Technol.*, *46*(12), 1359-1369.

Lopez-Hilfiker, F. D., S. Iyer, C. Mohr, B. H. Lee, E. L. D'Ambro, T. Kurten, and J. A. Thornton (2016a), Constraining the sensitivity of iodide adduct chemical ionization mass spectrometry to multifunctional organic molecules using the collision limit and thermodynamic stability of iodide ion adducts, *Atmos. Meas. Tech.*, *9*(4), 1505-1512.

Lopez-Hilfiker, F. D., et al. (2014), A novel method for online analysis of gas and particle composition: description and evaluation of a Filter Inlet for Gases and AEROsols (FIGAERO), *Atmos. Meas. Tech.*, *7*(4), 983-1001.

Lopez-Hilfiker, F. D., et al. (2015), Phase partitioning and volatility of secondary organic aerosol components formed from alpha-pinene ozonolysis and OH oxidation: the importance of accretion products and other low volatility compounds, *Atmos, Chem. Phys.*, *15*(14), 7765-7776.

Lopez-Hilfiker, F. D., et al. (2016b), Molecular composition and volatility of organic aerosol in the southeastern US: Implications for IEPOX derived SOA, *Environ. Sci. Technol.*, *50*(5), 2200-2209.

Loza, C. L., M. M. Coggon, T. B. Nguyen, A. Zuend, R. C. Flagan, and J. H. Seinfeld (2013), On the Mixing and Evaporation of Secondary Organic Aerosol Components, *Environmental science & technology*, *47*(12), 6173-6180.

Mohr, C., et al. (2017), Ambient observations of dimers from terpene oxidation in the gas phase: Implications for new particle formation and growth, *Geophys. Res. Lett.*, *44*(6), 2958-2966.

Ng, N. L., J. H. Kroll, M. D. Keywood, R. Bahreini, V. Varutbangkul, R. C. Flagan, J. H. Seinfeld, A. Lee, and A. H. Goldstein (2006), Contribution of first- versus second-generation products to secondary organic aerosols formed in the oxidation of biogenic hydrocarbons, *Environmental science & technology*, *40*(7), 2283-2297.

Pankow, J. F., and W. E. Asher (2008), SIMPOL.1: a simple group contribution method for predicting vapor pressures and enthalpies of vaporization of multifunctional organic compounds, *Atmospheric Chemistry and Physics*, *8*(10), 2773-2796.

Pathak, R. K., C. O. Stanier, N. M. Donahue, and S. N. Pandis (2007), Ozonolysis of alpha-pinene at atmospherically relevant concentrations: Temperature dependence of aerosol mass fractions (yields), *J. Geophys. Res.-Atmos.*, *112*(D3).

Poschl, U. (2005), Atmospheric aerosols: Composition, transformation, climate and health effects, *Angew. Chem.-Int. Edit.*, *44*(46), 7520-7540.

Renbaum-Wolff, L., J. W. Grayson, A. P. Bateman, M. Kuwata, M. Sellier, B. J. Murray, J. E. Shilling, S. T. Martin, and A. K. Bertram (2013), Viscosity of alpha-pinene secondary organic material and implications for particle growth and reactivity, *Proc. Natl. Acad. Sci. U. S. A.*, *110*(20), 8014-8019.

Roldin, P., et al. (2014), Modelling non-equilibrium secondary organic aerosol formation and evaporation with the aerosol dynamics, gas- and particle-phase chemistry kinetic multilayer model ADCHAM, *Atmospheric Chemistry and Physics*, *14*(15), 7953-7993.

Saleh, R., N. M. Donahue, and A. L. Robinson (2013), Time scales for gas-particle partitioning equilibration of secondary organic aerosol formed from alpha-pinene ozonolysis, *Environ. Sci. Technol.*, *47*(11), 5588-5594.

Schobesberger, S., E. L. D'Ambro, F. D. Lopez-Hilfiker, C. Mohr, and J. A. Thornton (2018), A model framework to retrieve thermodynamic and kinetic properties of organic aerosol from composition-resolved thermal desorption measurements, *Atmos. Chem. Phys. Discuss.*

Shilling, J. E., Q. Chen, S. M. King, T. Rosenoern, J. H. Kroll, D. R. Worsnop, K. A. McKinney, and S. T. Martin (2008), Particle mass yield in secondary organic aerosol formed by the dark ozonolysis of alpha-pinene, *Atmos. Chem. Phys.*, *8*(7), 2073-2088.

Shrivastava, M., et al. (2017), Recent advances in understanding secondary organic aerosol: Implications for global climate forcing, *Rev. Geophys.*, *55*(2), 509-559.

Stanier, C. O., R. K. Pathak, and S. N. Pandis (2007), Measurements of the volatility of aerosols from alpha-piniene ozonolysis, *Environmental science & technology*, *41*(8), 2756-2763.

Trump, E. R., and N. M. Donahue (2014), Oligomer formation within secondary organic aerosols: equilibrium and dynamic considerations, *Atmospheric Chemistry and Physics*, *14*(7), 3691-3701.

Tröstl, J., et al. (2016), The role of low-volatility organic compounds in initial particle growth in the atmosphere, *Nature*, *533*(7604), 527-+.

Vaden, T. D., D. Imre, J. Beranek, M. Shrivastava, and A. Zelenyuk (2011), Evaporation kinetics and phase of laboratory and ambient secondary organic aerosol, *Proc. Natl. Acad. Sci. U. S. A.*, *108*(6), 2190-2195.

Wilson, J., D. Imre, J. Beranek, M. Shrivastava, and A. Zelenyuk (2015), Evaporation Kinetics of Laboratory-Generated Secondary Organic Aerosols at Elevated Relative Humidity, *Environmental science & technology*, *49*(1), 243-249.

Wolfe, G. M., M. R. Marvin, S. J. Roberts, K. R. Travis, and J. Liao (2016), The Framework for 0-D Atmospheric Modeling (F0AM) v3.1, *Geosci. Model Dev.*, *9*(9), 3309-3319.

Ye, Q., E. S. Robinson, X. Ding, P. L. Ye, R. C. Sullivan, and N. M. Donahue (2016), Mixing of secondary organic aerosols versus relative humidity, *Proc. Natl. Acad. Sci. U. S. A.*, *113*(45), 12649-12654.

Yli-Juuti, T., et al. (2017), Factors controlling the evaporation of secondary organic aerosol from alpha-pinene ozonolysis, *Geophys. Res. Lett.*, *44*(5), 2562-2570.

Zaveri, R. A., R. C. Easter, J. E. Shilling, and J. H. Seinfeld (2014), Modeling kinetic partitioning of secondary organic aerosol and size distribution dynamics: representing effects of volatility, phase state, and particle-phase reaction, *Atmospheric Chemistry and Physics*, *14*(10), 5153-5181.

Zaveri, R. A., et al. (2018), Growth Kinetics and Size Distribution Dynamics of Viscous Secondary Organic Aerosol, *Environmental science & technology*, *52*(3), 1191-1199.

Zhang, Q., et al. (2007), Ubiquity and dominance of oxygenated species in organic aerosols in anthropogenically-influenced Northern Hemisphere midlatitudes, *Geophys. Res. Lett.*, *34*(13), L13801.

# Chapter 5. CONCLUSIONS

## 5.1 MAIN FINDINGS

Understanding atmospheric aerosol particles, a major component of which is secondary, is essential for understanding their impacts on climate, visibility, and human health. Much of this secondary organic aerosol is of biogenic origin, a large source of carbon to the atmosphere. The oxidation of BVOC is complex due to the vast combinations of BVOC and oxidants. Recent advances in instrumentation have allowed for the detection of species in both the gas- and particle-phases in order to allow for a mechanistic study of BVOC oxidation, providing us with a more holistic picture of how gas-phase species are processed into sufficiently low volatility material to aide in particle formation and growth.

The following broad questions guided the work presented herein:

(1) *What are the products formed from BVOC oxidation that influence SOA formation?*

(2) *What are the volatilities of those products?*

(3) *What is the mechanism of formation for those products?*

The data analysis has focused on three 6+ week deployments of a relatively novel instrumental setup to a large atmospheric simulation chamber at the Pacific Northwest National Laboratory. The use of atmospheric simulation chambers made it possible to isolate specific BVOC + oxidant reactions in order to carefully study the products generated and the formation of SOA.

The formation of isoprene SOA has been well established via acid-catalyzed heterogeneous uptake of certain oxidation products when aqueous acidic seed particles are present. While previous work had shown that SOA could be formed without this specific seed, the mechanism

of formation was largely unknown. In chapter 2, we identified species of very low volatility from the oxidation of isoprene by OH, namely, a $C_5$ dihydroxy dihydroperoxide ($C_5H_{12}O_6$). These species had sufficiently low volatility to partition to the available solid (inert) seed and form SOA. We developed a mechanism for the formation of the identified species and probed the volatility of the major particle-phase species. We compared the FIGAERO volatility measurements for specific particle-phase compounds to group contribution methods that predict the volatility based on composition. We found that a majority of species, based on mass contribution, behaved as expected, but >30% of the mass desorbed from the FIGAERO filter at temperatures higher than expected based on equilibrium partitioning. We concluded, in support of previous studies, that species can thermally decompose during thermal desorption from the filter, resulting in the detection of smaller molecular-weight species than what exist in the SOA. In this work, we also identified the effect of $NO_x$ ($NO_x$ = NO + $NO_2$), a common anthropogenic pollutant, to the products formed. As the concentration of $NO_x$ increased, the low volatility species decreased, accompanied by an increase in the corresponding organic nitrates, consistent with known chemistry involving $RO_2$ radicals reacting with NO. The major implication from this analysis was that anthropogenic emissions will lead to higher volatility material and therefore likely less SOA formation in the isoprene + OH case when SOA formation from reactive uptake is suppressed. This finding has implications for future conditions where urban areas impacted by isoprene will likely have $NO_x$ concentrations that are significant, but lower acidic aerosol surface area due to more effective reductions of sulfate precursor emissions.

In chapter 3, we apply a detailed mechanistic model to the isoprene SOA experiments presented in chapter 2 in order to understand the operating chemistry, and therefore allow the findings from

the chamber to be applied to the atmosphere. Our main conclusion is that, although we found very low volatility material can be formed from isoprene + OH, it is a minor pathway under typical atmospheric conditions within the polluted boundary layer. In chambers, it is often difficult if not impossible to simulate accurately the radical concentration regimes typical of the atmosphere. This problem is usually addressed by simulating similar ratios of reactants, such as $RO_2/HO_2$, $RO_2/NO_x$, etc., with the assumption that the same relative branching as occurs in the atmosphere will then be simulated in the chamber. However, this approach assumes that unimolecular permutations of $RO_2$ radicals are unimportant, or relatedly, that the overall lifetime of radicals against bi-molecular reactions is unimportant and only the branching is important. Over the past 5 years, the importance of room-temperature intramolecular $RO_2$ H-shifts, followed by $O_2$ addition to form more oxidized peroxy radical intermediates, has been documented for several relevant $RO_2$. Such intramolecular $RO_2$ chemistry, which can result in autoxidation, is in direct competition with bi-molecular reactions that could be suppressed by working with radical concentrations that are correct in a relative sense but too high in an absolute sense.

My detailed chemical modeling of the chamber experiments revealed that the $HO_2$ radical was much higher in the chamber than what is typically found in the ambient atmosphere, resulting in an unrealistic rate of $RO_2$ radicals reacting with $HO_2$ to form to hydroperoxides that out-competed intramolecular H-shifts that lead to different products with different SOA formation potential. In reproducing our results using the box model which explicitly simulates ~2100 species and ~700 reactions, including the dynamic partition of species between the gas- and aerosol phases, we found that the $RO_2$ radical undergoes intra-molecular H-shifts at a rate much

faster than previously thought, confirmed by quantum chemical calculations. The isomerization product was of significantly higher volatility than the hydroperoxide product, and thus by artificially increasing the importance of $RO_2 + HO_2$ due to the high $HO_2$ in the chamber, the chemistry favored low volatility material formation and therefore more SOA than would be observed in the atmosphere. These results confirm that the absolute concentrations of radicals, not just the ratios, are important to obtaining the correct distribution of products, which in turn affect SOA formation. Unfortunately, there are only a small handful of experiments where that condition has been achieved, calling into question the validity of SOA yields incorporated into most atmospheric models.

Chapter 4 explores the volatility of SOA formed from α-pinene ozonolysis, one of the most studied atmospheric reactions related to SOA. Despite the wealth of knowledge on this specific oxidation reaction, it remains unclear what the volatility of the resulting SOA is and thus how α-pinene SOA might respond to dilution or temperature variations. We adapted existing instrumentation in order to perform isothermal evaporations to determine factors controlling the lifetime of aerosol against dilution and possible formation processes. SOA was rapidly and completely diluted in a stream of $N_2$ for varying amounts of time on the order of minutes to hours, followed by a thermal desorption to investigate the remaining SOA. Two models, one explicitly applied to the specific measurement technique, the other simulating individual aerosol, were utilized to determine the processes controlling the observed evaporation rates. We found that the physical age of the aerosol, as opposed to the oxidative age, determines the evaporation rate and thus the volatility of the aerosol, proven by analyzing chamber aerosol of different ages and supported by observations of ambient SOA. Furthermore, we found that, while we could not

explicitly rule out the role of elevated viscosity causing the slow evaporation rate, the models were not able to reproduce the observed decays for individual compositions unless reversible oligomerization was invoked. Similar to the second chapter, this work has implications for how chamber experiments should be run in order to ensure that atmospherically relevant processes are being probed. Additionally, this work has implications for how SOA formation and loss should be implemented into atmospheric models.

## 5.2 Future Work

The work presented herein naturally suggests several additional experiments. Additionally, there are other applications for the FIGAERO-CIMS that would advance the field of SOA formation from BVOC. Some of these experiments which could be pursued are outlined below.

(1) The work in chapter 4 highlights the need to vary the time scales of chamber measurements. Most chamber experiments are performed on the minutes to hours timescales, limited by SOA mass and chamber volume. As highlighted in chapter 4, the volatility of the SOA formed in the chamber does not adequately represent the volatility observed in the field until after 24 hours of non-oxidative physical aging. Thus, performing experiments over longer time frames to allow slower chemistry to occur will allow for the better simulation of competitive pathways. Additionally, longer experimental time scales would allow for particle-phase transformations such as reversible oligomers, which are slower than the gas-phase radical chemistry typically studied, to occur. These types of experiments will advance our understanding of the lifetime and behavior of SOA after its initial formation and growth phase.

(2) There are still many BVOC + oxidant pairings that form SOA but which lack molecular-level composition information and detailed consideration of $RO_2$ chemistry. α-Pinene and isoprene are dominant components of BVOC emissions and thus have been extensively studied, but there are many other monoterpenes. The second most dominant monoterpene with a measured concentration of ~50% of α-pinene is $\Delta^3$-carene [*Hakola et al.*, 2012]. Due to its much lower emission rate, $\Delta^3$-carene has been studied less extensively than α-pinene. However, $\Delta^3$-carene has a reaction rate constant with OH, that is double that of α-pinene [*Atkinson et al.*, 1986]. Little is known about the products and their mechanism of formation from $\Delta^3$-carene, which, due to its rapid reaction with OH may form substantial SOA. In particular, it has been shown that α-pinene undergoes rapid self-reactions, termed auto-oxidation, under atmospheric conditions to form Extremely Low Volatility Organic Compounds (ELVOCs) [*Ehn et al.*, 2014] that are very efficient at forming SOA due to their strong preference for the condensed phase. While it is generally assumed that most, if not all, monoterpenes are able to undergo such auto-oxidation reactions, structure, particularly double bond location (endocyclic versus exocyclic), plays a significant role in which reactions are available to each isomer [*Kurten et al.*, 2015]. Therefore, it is essential to continue examining SOA formation from many BVOC/oxidant pairings in order to augment our knowledge on how SOA is formed in the atmosphere.

(3) While there are many other BVOC that can and should be investigated for their ability to form SOA, there are fewer oxidants. OH and $O_3$ are heavily studied and reasonably well known, although oxidation of BVOC by $NO_3$ is still a mechanistic area that requires

attention. Reaction rate constants of BVOC with $NO_3$ are large relative to reaction with OH or $O_3$ [*Atkinson and Arey*, 2003], and can be an important source of SOA regionally such as in the SE US where anthropogenic and biogenic emissions are high [*Pye et al.*, 2010]. However, a definitive understanding of the SOA yield and a mechanistic understanding of the gas-phase products formed and properties of the SOA such as chemical composition, volatility, and phase-state are lacking.

(4) While isolating specific BVOC and oxidant reactions is useful to develop chemical mechanisms, it is not representative of the atmosphere, and may lead to incorrect results. Thus, more work is needed to now take the individual experiments and start combining BVOC and oxidants in atmospherically relevant ratios to approach the makeup of the atmosphere. A detailed chemical box model accounting for relevant reactions occurring in the chamber should be used in conjunction with all chamber experiments to make sure that difficult-to-measure species, such as radical intermediates, are present within atmospherically relevant ranges or at a minimum the sensitivity to their abundance be probed. This work can be guided by what is measured in the atmosphere, and should attempt to mimic various different environments, such as the boreal forest versus deciduous forests, both under pristine and anthropogenically influenced conditions.

(5) One of the main difficulties in unraveling SOA mechanisms currently is that it is very difficult to measure functional groups of organic vapors directly, or to not alter functional group distribution in the workup procedures for studying SOA composition. One way to gain

insight using existing instrumentation and methods could be by adapting the evaporation method described in chapter 4. By using $N_2$ humidified with $D_2O$, the number of exchangeable hydrogens can be determined by observing a shift in the mass spectra of +1 Th for each hydrogen that exchanges with a deuterium. The rate of hydrogen/deuterium exchange is correlated to the strength of the hydrogen bond [*Steffel et al.*, 2007], and thus can be used to provide insight into the functional groups present. For example, the hydrogen of a peroxide group is less strongly bound than the hydrogen of an alcohol group [*Blanksby and Ellison*, 2003] and would therefore be expected to exchange more readily. These types of experiments should be performed, as with the regular evaporation experiments, during a steady state chamber experiment in order to minimize the number of variables.

The effects of dilution were examined in chapter 4, and a natural follow up would be to examine the effects of temperature changes. Most chamber studies are operated at room temperature, but the range of temperatures at which SOA is present in the atmosphere ranges drastically from the arctic to deserts, or for example when BVOC is lofted into the free troposphere. As temperature increases the rate of autoxidation leading to the possible formation of ELVOC would increase rapidly, but the rate of evaporation from the SOA would also increase. Conversely, lower temperatures may even stop autoxidation yet drive condensation of semi-volatile material to the SOA. The net effects of these opposing processes would aid in the modeling of SOA formation across the globe where temperatures vary widely.

References

Atkinson, R., and J. Arey (2003), Gas-phase tropospheric chemistry of biogenic volatile organic compounds: a review, *Atmospheric Environment*, *37*, S197-S219.

Atkinson, R., S. M. Aschmann, and J. N. Pitts (1986), Rate constants for the gas-phase reactions of the OH-radical with a series of monoterpenes 294 +/- 1-K, *International Journal of Chemical Kinetics*, *18*(3), 287-299.

Blanksby, S. J., and G. B. Ellison (2003), Bond Dissociation Energies of Organic Molecules, *Accounts Chem. Res.*, *36*(4), 255-263.

Ehn, M., et al. (2014), A large source of low-volatility secondary organic aerosol, *Nature*, *506*(7489), 476-479.

Hakola, H., H. Hellen, M. Hemmila, J. Rinne, and M. Kulmala (2012), In situ measurements of volatile organic compounds in a boreal forest, *Atmospheric Chemistry and Physics*, *12*(23), 11665-11678.

Kurten, T., M. P. Rissanen, K. Mackeprang, J. A. Thornton, N. Hyttinen, S. Jørgensen, M. Ehn, and H. G. Kjaergaard (2015), Computational study of hydrogen shifts and ring-opening mechanisms in alpha-pinene ozonolysis products, *J. Phys. Chem. A*, *119*(46), 11366-11375.

Pye, H. O. T., A. W. H. Chan, M. P. Barkley, and J. H. Seinfeld (2010), Global modeling of organic aerosol: the importance of reactive nitrogen (NO<sub>x</sub> and NO<sub>3</sub>), *Atmos. Chem. Phys.*, *10*(22), 11261-11276.

Steffel, L. R., T. J. Cashman, M. H. Reutershan, and B. R. Linton (2007), Deuterium exchange as an indicator of hydrogen bond donors and acceptors, *J. Am. Chem. Soc.*, *129*(43), 12956-+.

# VITA

Emma L. D'Ambro grew up in Schaghticoke, a small town in upstate New York. Throughout high school she studied a variety of subjects and was active in athletics, participating in cross country and indoor and outdoor track. She attended Le Moyne College in Syracuse New York where she majored in chemistry, minored in math and physics, and ran NCAA varsity cross country. In the summer of 2012 she accepted a research position at Duke University investigating the composition of flowback samples from hydraulic fracturing, sparking her interest in environmental chemistry. After graduation in 2013 from Le Moyne, she moved to Seattle to begin her Ph.D. in the Thornton group. Emma finished the program in 2018 with a Ph.D. in analytical chemistry.